Modeling of Material Degradation using Decoupled Finite Element Approaches: Applications to Localized Corrosion of Iron Alloys and Hydraulic Fracture of Glaciers

By

Xiangming Sun

Dissertation

Submitted to the Faculty of the

Graduate School of Vanderbilt University

in partial fulfillment of the requirements

for the degree of

DOCTOR OF PHILOSOPHY

in

Civil Engineering

December 12, 2020

Nashville, Tennessee

Approved:

Ravindra Duddu, Ph.D.

Alan Bowers, Ph.D.

Caglar Oskay, Ph.D.

Paul Laibinis, Ph.D.

To my beloved parents, Yi Wang and Weiliang Sun

ACKNOWLEDGMENTS

Firstly, I would like to express my great thankfulness to my advisor Professor Ravindra Duddu, who has always been encouraging and supportive during the past five years. His enthusiasm and scrupulous attitude to science led me to be a qualified researcher. Without his support and guidance, I would not be able to finish this dissertation.

I also would like to thank Dr. Alan Bowers, Dr. Caglar Oskay, and Dr. Paul Laibinis for serving on my dissertation committee. Their insightful comments and valuable suggestions motivated me to widen my research from various perspectives.

I would like to extend my thanks to my colleagues who have been along with me for the academic journey at Vanderbilt University. Especially, I would like to acknowledge my group mates, including Dr. Stephen Jiménez, Mr. Gourab Ghosh, and Mr. Yuxiang Gao, as well as my collaborators, including Dr. Robert G. Kelly and Dr. Jayendran Srinivasan, for their help and support throughout my graduate study.

Last but not the least, I would like to express my deepest gratitude to my parents and grandparents for their love, support, and encouragement. They always stand with me as my strongest backup for whatever I pursue. I am forever indebted to them for giving me the opportunities and experiences that have made me who I am today.

TABLE OF CONTENTS

LIST OF TABLES

LIST OF FIGURES

Chapter 1

INTRODUCTION

The goal of this dissertation is to apply the notion of decoupling on highly non-linear mathematical models describing material degradation within the framework of the finite element method. Multiple chemical and physical processes can cause the degradation of materials and pose a significant threat to the safety and stability of both man-made or natural materials and structures [164]. Material degradation induced by localized corrosion is a huge concern especially for military mobile and fixed equipment and structures because of their prolonged exposure to harsh/marine (aggressive) environments [28, 35, 51, 128]. To mitigate these risks, it is essential to fundamentally understand and predict the propagation of localized corrosion. Damage accumulation over time can also lead to the degradation of different materials, such as man-made metallic alloys and natural polycrystalline ice. Because progressive degradation of materials can severely weaken the mechanical strength, a localized crack can initiate in damaged zone and propagate in a rapid rate.

Complementary to experiments, numerical modeling studies are essential and effective to better understand the chemical and physical processes associated with material degradation and to predict the failure of materials. It is ideal to use a coupled numerical algorithm to solve the equations describing material degradation. However, the coupled approaches often encounter numerical issues owing to the complexity of algorithms and high non-linearity of governing equations. Therefore, decoupled algorithms are developed and implemented to model the degradation of iron alloys and glaciers. The focus of this dissertation is to first test the viability and accuracy of decoupled approaches through verification and validation studies, and then explore the fundamental mechanisms that dominant material degradation related physical and chemical processes, including localized corrosion and hydraulic fracture of glaciers.

Fundamental understanding and prediction of localized corrosion is difficult due to the complex nature of initiation and propagation events spanning multiple size and time scales. The initiation of localized corrosion sites involving passive film breakdown is stochastic in nature and takes place on smaller length scales (on the order of nanometers) [55]. Therefore, it is not possible to predict exactly when and where pits will nucleate, and mechanistic/deterministic models only consider the physical and chemical processes of corrosion propagation after initiation based on mass and charge balance. The simplest of mechanistic models consider mass transport of solute species (e.g., metal or hydrogen ions) in the solution environment based on Fickian diffusion [7, 82, 137, 138, 140], but they ignore electro-migration effects on ion transport. Perhaps, the first-ever comprehensive mechanistic model of pitting and crevice corrosion, considering electro-diffusive mass transport of multi-ionic species and homogeneous chemical reactions in solution, was proposed by Sharland and Tasker [131, 133]; however, the analysis was restricted to one-dimension due to model complexity. Also, because only the equilibrium constants for the chemical reactions are known, the reformulation of governing equations to eliminate the unknown forward and backward reaction rate terms is necessary if a chemical species is added to or removed from the system. An alternative approach is to simply assume a large enough value of reaction rate so that the reactions are fast compared to diffusive transport [162, 163]. This approach is prone to numerical convergence issues due to poor conditioning of matrices resulting from the discretization of electro-diffusion-reaction equations of multi-ionic systems. Therefore, it is quite challenging to numerically model the electro-diffusive mass transport of species and homogeneous chemical reactions within the electrolyte simultaneously.

Damage accumulation and fracture (or crevasse) propagation in glaciers and ice shelves are critical processes that determine the mass balance of continental ice sheets and can contribute to global sea level rise [47]. Crevasses have historically been thought to be opening (mode I) fractures formed under the action of tensile normal stress. Iceberg calving, which

is a dominant mode of mass loss from ice sheets, occurs when the combination of basal and surface crevasses penetrates the entire ice thickness, thus isolating an iceberg [19]. Existing calving models analytically estimated the crevasse penetration depths in glaciers and ice shelves using linear elastic fracture mechanics (LEFM) models [77, 159]. The fundamental assumption of these LEFM models is that crevasses will penetrate to the depth where stress intensity factor reaches a critical value. However, using the LEFM to explicitly track the propagation of crevasse tip can be algorithmically cumbersome. In the recent decades, crevasse propagation has been implicitly captured by implementing continuum damage mechanics (CDM) models [44, 116]. While LEFM only requires the critical value of the stress intensity factor, one needs to define and calibrate several parameters when applying the phenomenological creep damage model. In contrast, the phase-field method for brittle fracture [95] can be an ideal tool to model and simulate glacier crevasse propagation. It replaces discrete sharp crack surfaces with a smeared zone of damaged material by representing the crack with the continuous damage (phase field) variable [86, 95]. Because the phase field is a CDM approach, it enables implicit crack surface tracking but eliminates the need for calibration of several phenomenological damage parameters. However, a significant challenge of the phase field model is that it involves the solution of coupled nonlinear PDEs for the damage and displacement fields over the computational domain.

As discussed above, the interactions between different physical processes (i.e., mass transport and chemical reactions during localized corrosion) and field variables (i.e., damage, displacement, and crack driving force during glacier crevasses propagation) can cause numerical issues when solving the governing nonlinear partial differential equations and algebraic equations in a fully coupled manner. Decoupled numerical methods, also referred to as operator-splitting approaches, are better suited to handle the high non-linearity together with multiple physical processes and fields in a robust, flexible, and efficient manner. To comprehensively demonstrate advantages of the decoupled numerical algorithm on solving multi-physics problems describing material degradation related chemical and phys-

ical processes, three objectives are set and systematically discussed in this dissertation.

The first objective of this dissertation is to develop a sequential non-iterative approach (SNIA) that individually treats electro-diffusive ion transport and homogeneous chemical reactions using the standard finite element method. The concentration of ionic species and the electrical potential in the electrolyte domain are described by the Nernst-Planck equations and the local electro-neutrality (LEN) condition. The metal-solution (electrode-electrolyte) interface fluxes are defined in terms of the anodic and cathodic current densities using Tafel kinetics. The electro-diffusion equations are decoupled from the chemical equilibrium equations using the SNIA in two steps. In the first step, the electro-diffusion equations are linearized using the Newton-Raphson method, discretized using the standard finite element method, and solved in the open-source software FEniCS to establish "uncorrected" species concentrations. In the second step, the nonlinear chemical equilibrium equations are linearized using the Newton-Raphson method along with the under-relaxation technique to ensure non-negativity of concentrations and solved in FEniCS to establish the "corrected" species concentrations. Numerical studies, including model comparison, parametric and experimental validation studies, are conducted to simulate localized crevice/cavity corrosion of generic carbon steel and iron-chromium binary alloys and to demonstrate the efficacy of this proposed approach.

The second objective of this dissertation is to examine critical electrochemical factors for stable dissolution and repassivation of the localized corrosion site on the surface of metallic materials using the proposed SNIA. Existing studies have shown that localized corrosion is a complex electrochemical dissolution process occurring at the interface between metal (solid) and electrolyte (liquid) [49, 55]. The stable propagation of localized corrosion is governed by the bulk environment, the composition of the alloy, and the aggressive chemistry within the localized corrosion site [75, 175]. The conditions that ensure the maintenance of such chemistry are typically analyzed using the one-dimensional (1-D) pit concept. The 1D pit experiments first apply a high electrical potential in order to

initiate and grow pits, which leads to the precipitation of a salt film on the corroding surface [64, 151]. Under such circumstance, metal dissolution is diffusion-limited so that the corroding system is in a quasi-steady state. The pit stability product under a salt film can then be extracted from measuring the diffusion-limited current density at different pit depths [57, 81, 98, 104]. To estimate the conditions that govern the transition of the pit from stability to repassivation, rapid polarization scans can be employed which decrease the applied potential below the point where the salt film disappears. In this stage, metal dissolution proceeds in a salt film-free environment. As the applied potential is gradually decreased, the corresponding decrease in metal dissolution rate and diminished cation hydrolysis [92] would lead to an increase of the pH near the corroding surface and eventually cause the pit to passivate. The repassivation potential is the potential corresponding to the conditions below which the pit will no longer propagate [12, 67, 149]. These critical electrochemical factors, including species concentrations, electrolyte pH and resistance, and electrical potential, for 1D pit experiments can be numerically examined using the SNIA so that fundamental mechanisms dominant localized corrosion and its passivation can be well explained.

The third objective of this dissertation is to predict the propagation of glacier crevasses using a decoupled finite element approach based on a phase-field model combining brittle fracture with hydrofracture. Hydrofracture can promote the propagation of glacier crevasses and, in some cases, lead to full-depth penetration and ice-shelf calving. However, the stress field driving the hydrofracturing process is simplified even ignored in most modeling studies about glacier calving. To this end, the phase field model proposed by Miehe et al. [95] is extended based on the notion of poro-damage mechanics [47, 99] to model hydrofracturing of water-filled glacier crevasses. The extended poro-damage phase-field model is based on hybrid formulation and can be implemented using a sequential non-iterative (or staggered) update scheme of time-discrete fields in three steps. In the first step, the displacement field $\boldsymbol{u}$ is solved using the momentum balance equation along with

its boundary conditions. In the second step, the elastic strain energy is calculated and the crack driving force is updated accordingly. In this step, the strain energy is decomposed into positive and negative components using three different elastic strain energy decomposition schemes. Based on the assumption that compressive normal stress at the crack tip will not lead to crack opening, only the positive component is used to update the history field variable. In the last step, the phase field (damage) variable is obtained from solving the damage evolution equation using the standard finite element method. As the benchmark solution, the predictions of maximum crevasse penetration depths obtained using LEFM models for different idealized scenarios will be compared to corresponding phase-field predictions.

Chapter 2

A SEQUENTIAL NON-ITERATIVE APPROACH FOR MODELING MULTI-IONIC SPECIES REACTIVE TRANSPORT DURING LOCALIZED CORROSION

This chapter has been published in the journal Finite Elements in Analysis and Design as the following peer-reviewed manuscript: Sun X. and Duddu R., A sequential non-iterative approach for modeling multi-ionic species reactive transport during localized corrosion. *Finite Elements in Analysis and Design* 166 (2019) 103318. doi:10.1016/j.finel.2019.103318

2.1 Introduction

Localized corrosion of iron and steel alloys, including pitting, stress corrosion cracking, corrosion fatigue, and crevice corrosion [87], poses a significant threat to structural safety. For military mobile and fixed equipment and structures, localized corrosion is a huge concern because of their prolonged exposure to harsh/marine environments [128]. Despite significant advances in corrosion science research, fundamental understanding and prediction of localized corrosion is difficult due to the complex nature of initiation and propagation events spanning multiple size and time scales [55]. Complementary to experimental studies, mechanistic modeling studies are essential to better understand the physical and chemical processes associated with localized corrosion and to predict corrosion rates under varying environmental conditions. The propagation or passivation of localized corrosion sites (i.e., pits or crevices) is significantly influenced by the solution chemistry and alloy composition [12, 175]. However, it is challenging to numerically solve highly-nonlinear, time-dependent reactive-transport equations for establishing the solution chemistry with multi-ionic solute species. Therefore, herein we develop a sequential non-iterative approach (SNIA) that treats homogeneous chemical reactions along with electro-diffusive ion transport using the standard finite element method, and establish its viability through verification and validation studies.

The initiation of localized corrosion sites involving passive film breakdown is stochastic in nature and takes place on smaller length scales (on the order of nanometers) [55], it is not possible to predict exactly when and where pits will nucleate. Therefore, mechanistic/deterministic models only consider the physical and chemical processes of corrosion propagation after initiation based on mass and charge balance. The simplest of mechanistic models consider mass transport of solute species (e.g., metal or hydrogen ions) in the solution environment based on Fickian diffusion [7, 82], but they ignore electro-migration effects on ion transport. Perhaps, the first-ever comprehensive mechanistic model of pitting and crevice corrosion, considering electro-diffusive mass transport of multi-ionic species and homogeneous chemical reactions in solution, was proposed by Sharland [131, 133]; however, the analysis was restricted to one-dimension due to model complexity and the propagation of the corrosion interface was neglected. Also, applying this approach to multi-ionic systems is cumbersome because it requires reformulating the governing equations to eliminate reaction terms from mass transport equations, if a chemical species is added to or removed from the system. The reformulation is necessary because only the equilibrium constants for the chemical reactions are known; whereas, the reaction rates are largely unknown. An alternative approach is to simply assume a large enough value of reaction rate so that the reactions are fast compared to diffusive transport [162, 163]. This approach is prone to numerical convergence issues due to poor conditioning of matrices resulting from the discretization of electro-diffusion-reaction equations of multi-ionic systems. Later, with the advent of commercial finite element software, such as COMSOL, several researchers have investigated the multi-ionic reactive-transport in the solution environment with a static corrosion interface [91, 145] or a moving corrosion interface of a single pit/crevice [147, 169]. Galvanic corrosion studies usually simplify the model formulation by neglecting electro-diffusive transport and chemical reactions, and only considering the Laplace equation for electrical potential [3, 41] which may be valid under certain idealized conditions.

Despite advances in numerical methods and the availability of commercial software, it

is quite challenging to numerically model the dynamic (spatio-temporal) evolution of the solution chemistry and electrical potential in the presence of multi-ionic species along with the morphological evolution of pits/crevices in two or three dimensions. Consequently, modeling studies that simulate morphology evolution by solving a moving boundary problem did not consider the electro-diffusion of ionic species and/or homogeneous chemical reactions. Broadly, these moving boundary models of corrosion interface evolution can be categorized as: sharp-interface finite element models [42, 156]; diffuse-interface cellular-automaton models [112, 125, 126]; diffuse-interface phase field models [2, 88–90]; and peridynamic models [33, 66]. A few modeling studies considered multi-ionic reactive transport and morphology evolution [13, 124, 170] with limited success. Specifically, the nonlinear fluxes of ionic species generated from electrode reactions and rapid concentration changes taking place in the solution environment due to nonlinear chemical reactions [103] can cause severe convergence issues in one-step (coupled) numerical methods. Furthermore, there exists several orders of magnitude difference in timescales of corrosive dissolution, homogeneous chemical reactions, and electro-diffusive mass transport [124]. Typically, corrosion interface evolution is much slower than the mass transport of ions in solution; whereas, chemical reactions are extremely fast so that equilibrium is attained almost instantaneously. The use of equilibrium equations instead of kinetic expressions is valid when there is a vast separation of time scales between mass transport and chemical reactions. The two-step (decoupled) numerical methods, also referred to as operator-splitting approaches, are better suited to handle the high nonlinearity and vast separation of timescales in a robust, flexible, and efficient manner.

In two-step numerical methods, multi-ionic mass transport and chemical reactions are solved separately and sequentially at any given time increment [172]. In general, the two-step methods are easier to implement than one-step methods on parallel computers and lead to better conditioned discretized system of equations, because the nonlinear partial differential equations governing mass transport are decoupled from the nonlinear algebraic

equations governing chemical reactions. This can be a significant advantage in the treatment of reduction-oxidation (redox) problems, especially, when a large number of chemical species exist in the solution environment [141]. Therefore, two-step methods have been widely applied to solve reactive-transport problems excluding electro-migration effects [62, 120, 141, 157, 161, 173]. The main disadvantage is that decoupling the mass transport and chemical reaction will introduce a numerical error in the resolution of a reactive-transport problem. However, previous studies [62, 157] have shown that the error can be reduced by decreasing the size of time increment. The two-step methods can be divided in two main classes: the sequential iterative approach (SIA) and the sequential non-iterative approach (SNIA). In the SIA, iterations are performed between the mass transport and chemical reaction steps within a time increment until convergence is reached; whereas, in the SNIA iterations are not performed between the two steps [121]. Because the iteration between two steps will reduce the decoupling (or splitting) error, the SIA does not require the time increment size as small as the SNIA to ensure numerical accuracy [62]. Remarkably, Walter et al. [161] found that the discrepancy between results obtained from the SIA and the SNIA is less than 2% when the same size of time increment was applied. However, the CPU load of the SIA is about 3.5 times compared to that of the SNIA, which means the SNIA is adequately accurate and much more efficient to solve the reactive-transport problems.

The current trend in reactive transport modeling is to use two-step methods, but existing studies usually consider advection-diffusion of chemical species and neglect the influence of the electric potential field established due to ion migration [62, 120, 141, 157, 161, 173]. Relatively, fewer studies in the literature [14, 121] have implemented the SNIA for electro-diffusive-reactive transport with applications to ion transport in porous media. The SNIA has been seldom applied for corrosion problems, except for Sharland [132] wherein a two-step (SNIA-like) method was implemented. To our knowledge, previous studies did not investigate the numerical accuracy and its time increment sensitivity within the context of

finite element analysis of electrochemical systems. Therefore, in this chapter, we present a two-step sequential non-iterative approach (SNIA) to solve the electro-diffusion-reaction equations corresponding to localized corrosion, and comprehensively study its numerical accuracy and time increment sensitivity. The concentration of ionic species and the electrical potential in the electrolyte domain are described by the Nernst-Planck equations and the local electro-neutrality (LEN) condition. The metal-solution (electrode-electrolyte) interface fluxes are defined in terms of the anodic and cathodic current densities using Tafel kinetics. The electro-diffusion equations are decoupled from the chemical equilibrium equations using the SNIA in two steps. In the first step, the electro-diffusion equations are linearized using the Newton-Raphson method, discretized using the standard finite element method, and solved in the open-source software FEniCS to establish "uncorrected" species concentrations. In the second step, the nonlinear chemical equilibrium equations are linearized using the Newton-Raphson method along with the under-relaxation technique to ensure non-negativity of concentrations and solved in FEniCS to establish the "corrected" species concentrations. Herein, we do not consider interface evolution due to corrosive dissolution, because the emphasis is on evaluating the accuracy and robustness of the SNIA.

The remainder of this chapter is organized as follows: in Section 2.2, we establish the governing equations of the reactive-transport model for localized corrosion, including the coupled and decoupled forms; in Section 2.3, we detail the numerical implementation of the SNIA, including the linearization and discretization of the governing equations with the under-relaxation technique; in Section 2.4, we present several benchmark numerical examples simulating localized corrosion of carbon steel and iron-chromium binary alloys to illustrate the viability of the SNIA; in Section 2.5, we conclude with a brief summary and closing remarks.

2.2 Model formulation

In this section, we first present the multi-ionic species reactive transport equations corresponding to the localized corrosion problem, wherein the motion of the corrosion interface is neglected. We next present an alternative set of governing equations for the same corrosion problem by separating the electro-diffusion-based mass transport equations from the chemical-equilibrium-based reaction equations.

2.2.1 Coupled form

The multi-ionic species reactive transport equations describing the concentration of chemical species are derived based on the dilute solution theory [87]. We define a regular two-dimensional domain $\Omega \subset \mathbb{R}^2$ that consists of two phases: the solid metal domain Ω_s and the liquid solution domain Ω_l, as shown in Figure 2.1. The solid and liquid domains are separated by a sharp corrosion interface $\Gamma_{\text{int}} = \Gamma_a \cup \Gamma_c$, where Γ_a and Γ_c denote the anodic and cathodic boundaries, respectively. In the electrolyte domain Ω_l, the rate of change of ionic concentration occurs due to both species mass transport and homogeneous chemical reactions. According to the law of conservation of mass, the transport equation of species i can be expressed as

$$\frac{\partial C_i}{\partial t} = -\nabla \cdot \boldsymbol{J}_i + R_i \ \text{ in } \ \Omega_l, \ i = \{1, 2, \cdots, n\}, \tag{2.1}$$

where C_i and $\boldsymbol{J}_i$ are the concentration and flux density of chemical species i, respectively, and are functions of both spatial coordinates $\mathbf{x}$ and time t; ∇ denotes the spatial gradient vector; R_i is the rate of chemical reactions and n denotes the total number of species in Ω_l. By assuming the electrolyte to be in a stagnant condition, advection can be ignored, and the flux $\boldsymbol{J}_i$ of the i^{th} species due to ionic diffusion and electro-migration is given by

$$\boldsymbol{J}_i = -D_i \nabla C_i - \frac{z_i F}{R^* T} D_i C_i \nabla \phi, \tag{2.2}$$

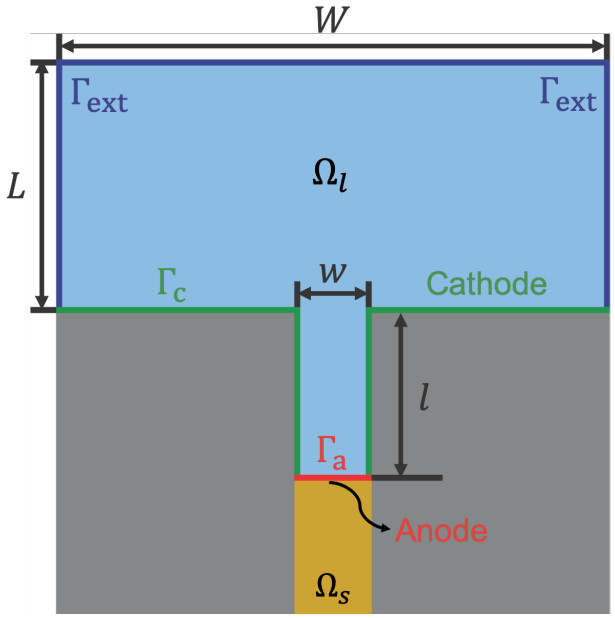

Figure 2.1: Schematic diagram of the two-dimensional domain for the localized (crevice) corrosion problem. The corrosion interface Γ_a (red) between solid metal Ω_s (gold) and liquid solution Ω_l (light blue) domains. The anodic (red) and cathodic (green) boundaries are denoted by Γ_a and Γ_c, where electrode reactions occur. The rest of the domain (gray) may be composed of a passive material and is excluded from the domain. Far-field (or bulk solution) concentrations and zero potential conditions are prescribed at the external (dark blue) boundary Γ_{ext}.

where D_i [m^2/s] is the Fickian diffusion coefficient of species i, z_i [–] is the charge number, F [C/mol] is the Faraday's constant, R^* [J/mol/K] is the universal gas constant, T [K] is the temperature, and ϕ [V] is the electrical potential.

Let us consider that there are n_r total number of homogeneous chemical reactions occurring in the electrolyte domain Ω_l involving certain chemical species as reactants and products. The general form of the r^{th} chemical reaction can be written as

$$\sum_p \nu_{rp} \mathrm{S}_p \rightleftharpoons \sum_q \nu_{rq} \mathrm{S}_q, \tag{2.3}$$

where S_p and S_q denote the symbol for the chemical formula of the reactant and product species involved in the reaction, respectively; ν_{rp} denotes the stoichiometric coefficient for species p in the r^{th} chemical reaction. The rate of production (or consumption) of chemical

species i due to homogeneous chemical reactions can be generalized as [87]

$$R_i = \sum_{r=1}^{n_r} \left\{ \omega_{ri} k_r \left(K_r \prod_p C_p^{\nu_{rp}} - \prod_q C_q^{\nu_{rq}} \right) \right\}, \tag{2.4}$$

where k_r and K_r are the rate and the equilibrium constants of the r^{th} reaction, respectively, ω_{ri} represents whether chemical substance S_i is a reactant, product or not involved in the forward direction of the r^{th} reaction. If S_i is not involved in the r^{th} reaction, $\omega_{ri} = 0$; however, if involved in the forward reaction as the product then $\omega_{ri} = 1$, or as the reactant then $\omega_{ri} = -1$. Substituting Equations (2.2) and (2.4) into the transport equation (2.1) yields

$$\frac{\partial C_i}{\partial t} = D_i \nabla^2 C_i + \frac{z_i D_i F}{R^* T} \nabla \cdot (C_i \nabla \phi) + \sum_{r=1}^{n_r} \left\{ \omega_{ri} k_r \left(K_r \prod_p C_p^{\nu_{rp}} - \prod_q C_q^{\nu_{rq}} \right) \right\}. \tag{2.5}$$

Solving Equation (2.5) directly maybe impractical because the value of the rate constant k_r for a specific reaction is not known and only the equilibrium constant K_r is known from thermodynamic considerations [87]. However, Equation (2.5) can be numerically solved by considering k_r as an adjustable numerical-rate parameter for fast reactions that are in equilibrium at any given location and time. The choice of k_r is usually based on numerical stability and convenience; choosing a large value for k_r ensures chemical equilibrium, but it may lead to numerical issues, such as ill-conditioning, instability and lack of convergence. Alternatively, the steady-state form of Equation (2.5) can be rearranged to eliminate the reaction terms R_i and solved together with chemical equilibrium equations [131], as described in Appendix B. The drawbacks of this alternative model formulation are that the governing equations need to be manually rearranged for each particular electrolyte system and it is still prone to numerical issues while solving nonlinear algebraic (chemical reaction) equations together with partial differential (mass transport) equations.

2.2.2 Decoupled form

To accurately describe the chemical equilibrium state and to alleviate numerical issues, we consider a decoupled model formulation. According to the operator splitting approach [162], we split Equation (2.5) into two separate equations describing mass transport and homogeneous chemical reactions. The advantage of our model formulation is that it can be solved using sequential non-iterative or partly-iterative algorithms in an accurate, efficient and robust manner [14].

2.2.2.1 Mass transport

The ionic concentrations and electrical potential in the electrolyte domain are governed by the Nernst-Planck equations that do not include reaction kinetics. Neglecting chemical reactions will yield physically incorrect ionic concentrations, which can be corrected using chemical equilibrium equations. The so-called "uncorrected" concentrations $\widetilde{C}_i$ can be computed as

$$\frac{\partial \widetilde{C}_i}{\partial t} - D_i \nabla^2 \widetilde{C}_i - \frac{z_i D_i F}{R^* T} \nabla \cdot \left(\widetilde{C}_i \nabla \phi \right) = 0 \ \text{ in } \ \Omega_l, \ i = \{1, 2, \cdots, n\}, \tag{2.6}$$

where $\widetilde{C}_i$ and ϕ are functions of both spatial coordinates $\mathbf{x}$ and time t. Because the chemical reactions satisfy charge balance, the electrical potential can be established by enforcing the local electro-neutrality (LEN) condition on the "uncorrected" concentrations as

$$\sum_{i=1}^{n} z_i \widetilde{C}_i = 0 \ \text{ in } \ \Omega_l. \tag{2.7}$$

Thus, the uncorrected concentrations and electrical potential can be determined by solving Equation (2.6) along with LEN condition Equation (2.7). The intial and boundary con-

ditions corresponding to Equations (2.6) and (2.7) are given by

$$\begin{aligned} \widetilde{C}_i(\mathbf{x},0) &= C_i^{\infty} \text{ and } \phi(\mathbf{x},0)=0 \qquad \text{in } \Omega_l, \\ \widetilde{C}_i(\mathbf{x},t) &= C_i^{\infty} \text{ and } \phi(\mathbf{x},t)=0 \qquad \text{on } \Gamma_{\text{ext}}, \\ -D_i\left(\nabla\widetilde{C}_i+\frac{z_iF}{R^*T}\widetilde{C}_i\nabla\phi\right)\cdot\mathbf{n} &= \frac{I_i}{z_iF} \quad \text{on } \Gamma_{\text{int}}, \end{aligned} \tag{2.8}$$

where C_i^{∞} is the far-field concentration of species i, $\mathbf{n}$ denotes the unit normal to the interface Γ_{int} pointing outward from Ω_l, and I_i [A/m^2] represents the electrode current density. According to Tafel kinetics [133], the electrode current density is usually defined by an exponential function of over-potential η [V] as

$$I_i = \hat{I}_i \exp\left(\frac{\alpha_i F\eta}{R^*T}\right), \tag{2.9}$$

where the exchange current density $\hat{I}_i$ [A/m^2] and the charge transfer coefficient α_i [–] are obtained from polarization experiments. The over-potential is defined as

$$\eta = \phi_{\text{M}} - \phi_{\text{E}}, \tag{2.10}$$

where ϕ_{M} is the metal potential and ϕ_{E} the potential drop from Γ_{int} to Γ_{ext}. It is possible that the electrode current density depends also on the concentration of certain chemical species, which will be considered later in Section 2.4.

2.2.2.2 Homogeneous chemical reactions

We assume that characteristic times of chemical reactions in aqueous solution are much shorter than those of the mass transport or corrosion processes [132, 162]. Thus, the reactant and product species concentration in the electrolyte solution reaches the equilibrium state instantly as given by

$$K_r \prod_p C_p^{\nu_{rp}} = \prod_q C_q^{\nu_{rq}}. \tag{2.11}$$

The corrected concentration C_i that satisfy the chemical equilibrium condition in Equation (2.11) are related to the uncorrected concentrations $\widetilde{C}_i$ as

$$C_i = \widetilde{C}_i + \sum_{r=1}^{n_r} \omega_{ri} \nu_{ri} \widehat{C}_r, \tag{2.12}$$

where $\nu_{ri}\widehat{C}_r$ is the absolute value of concentration change of species i due to the r^{th} reaction. In Appendix A, we show that above equation defining the corrected concentration satisfies mass balance of all chemical species. Substituting Equation (2.12) into Equation (2.11), we can obtain n_r number of nonlinear algebraic (chemical reaction) equations to solve for unknowns $\widehat{C}_r$ as follows:

$$K_r \prod_p \left(\widetilde{C}_p + \sum_{l=1}^{n_r} \omega_{lp} \nu_{lp} \widehat{C}_l \right)^{\nu_{rp}} - \prod_q \left(\widetilde{C}_q + \sum_{l=1}^{n_r} \omega_{lq} \nu_{lq} \widehat{C}_l \right)^{\nu_{rq}} = 0, \;\; r = \{1, 2, \cdots, n_r\}. \tag{2.13}$$

Equations (2.6), (2.7) and (2.13) along with initial and boundary conditions defined in Equation (2.8) establish the governing equations of the decoupled model formulation for the multi-ionic species reactive transport associated with localized corrosion in a pit or crevice with a fixed geometry.

2.3 Numerical Implementation

In this section, we detail the sequential non-iterative approach (SNIA) and its implementation for solving the decoupled model formulation. To ensure non-negativity of ionic concentrations, we employ a modified Newton-Raphson scheme using the under-relaxation technique while solving the chemical equilibrium equations.

2.3.1 Solution strategy

We employ a two-step staggered numerical solution strategy at any given time increment as follows:

1. Compute the uncorrected concentrations $\widetilde{C}_i$ and electrical potential ϕ from the nonlinear Nernst-Planck equations (2.6) and the LEN condition (2.7) along with initial and boundary conditions defined in Equation (2.8);

2. Compute the corrected concentrations C_i of each species by solving the nonlinear chemical equilibrium equations (2.13).

Thus, the coupled equations of ion transport and homogeneous chemical reactions are solved sequentially only once within the given time increment. Because we do not iterative between the transport and reaction steps, the proposed numerical scheme can be classified as a sequential non-iterative approach. The pseudocode for SNIA at time increment $k+1$ is given in Algorithm 1.

2.3.2 Finite element approximation

The nonlinear Nernst-Planck equations (2.6) and the LEN condition (2.7) are discretized and solved using the standard finite element method in the open-source software FEniCS [9]. The electrolyte solution domain Ω_l is spatially discretized using quadratic (three-noded line or six-noded triangular) finite elements. At each finite element node there are

Algorithm 1: The sequential non-iterative approach (SNIA) for simulating multi-species reactive transport. In our notation, the left superscript indicates the time increment.

input : ${}^{k}C_i$ and ${}^{k}\phi$
output : ${}^{k+1}C_i$ and ${}^{k+1}\phi$
parameter: t^{∞}, Δt, D_i, z_i, F, R^{*}, T, K_i, ν_{ij}, and ω_{ij}

if $t \geq t^{\infty}$ **then**
  return ${}^{k+1}C_i = {}^{k}C_i$ and ${}^{k+1}\phi = {}^{k}\phi$;
  break
else
  solve `Electro-diffusion equations;` `// Eqs.(2.6) and (2.7)`
  compute ${}^{k+1}\widetilde{C}_i$ and ${}^{k+1}\phi$;
  return ${}^{k+1}\phi$;
  if ${}^{k+1}\widetilde{C}_i$ *compatible with chemical equilibrium state* **then** `// Eq.(2.11)`
    return ${}^{k+1}C_i = {}^{k+1}\widetilde{C}_i$;
  else
    solve `Chemical equilibrium equations;` `// Eq.(2.13)`
    compute ${}^{k+1}\widehat{C}_i$; `// Refer to Algorithm 2`
    return ${}^{k+1}C_i = {}^{k+1}\widetilde{C}_i + \sum_{j=1}^{n_r} \omega_{ji}\nu_{ji}\,{}^{k+1}\widehat{C}_i$;
  end
  update $t = t + \Delta t$;
end

$n+1$ unknown variables, including n uncorrected concentrations $\widetilde{C}_i$ and electrical potential ϕ, which are approximated as

$$\begin{aligned} \widetilde{C}_i(\mathbf{x},t) &= \sum_{A=1}^{n_e} N^A(\mathbf{x})\,\widetilde{C}_i^A(t), \\ \phi(\mathbf{x},t) &= \sum_{A=1}^{n_e} N^A(\mathbf{x})\,\phi^A(t), \end{aligned} \tag{2.14}$$

where N^A are the standard finite element shape functions, n_e is the total number of nodes in the mesh, $\widetilde{C}_i^A$ and ϕ^A denote the nodal degrees-of-freedom corresponding to the uncorrected concentration of species i and electrical potential at node A, respectively. The weak form for establishing the unknown fields $\widetilde{C}_i \in \widetilde{\mathscr{C}}$ and $\phi \in \Phi$ is given by

$$\begin{aligned} \sum_{i=1}^{n} \left\{ \int_{\Gamma_{\text{int}}} \frac{u_i I_i}{z_i F}\, d\Omega - \int_{\Omega_l} u_i \dot{\widetilde{C}}_i\, d\Omega - \int_{\Omega_l} \nabla u_i \cdot D_i \left(\nabla \widetilde{C}_i + \frac{z_i F}{R^* T} \widetilde{C}_i \nabla \phi \right) d\Omega \right\} \\ + \int_{\Omega_l} v \sum_{i=1}^{n} z_i \widetilde{C}_i\, d\Omega \quad = 0, \end{aligned} \tag{2.15}$$

where u_i and v are weighting functions, $\widetilde{\mathscr{C}}$ and Φ are spaces of sufficiently continuous functions corresponding to the uncorrected concentrations and electrical potential, respectively.

To solve the non-stationary, nonlinear weak form in Equation (2.15), we temporally discretize it using the backward Euler method and linearize using the Newton-Raphson method. To denote the value of a variable at time increment k we use the left superscript; for iterative procedures we use m as the counter and set it as a left subscript. Any symbol written without the left subscript indicates the converged value at the given time increment. For example, ${}^{k+1}_{m}\widetilde{C}_i$ denotes the uncorrected concentration of species i at time increment $k+1$ and iteration m; whereas, ${}^{k}C_i$ denotes the converged corrected concentration of species i at time increment k. The rate of change of species concentration at time increment $k+1$ can be defined as

$${}^{k+1}_{m}\dot{\widetilde{C}}_i = \frac{\partial\, {}^{k+1}_{m}\widetilde{C}_i}{\partial t} = \frac{{}^{k+1}_{m}\widetilde{C}_i - {}^{k}C_i}{\Delta t}, \tag{2.16}$$

where Δt is the size of time increment. Assuming all the variable fields are known at iteration m and time increment $k+1$, these fields can be linearized at iteration $m+1$ as

$$\begin{aligned} {}^{k+1}_{m+1}\widetilde{C}_i &= {}^{k+1}_{m}\widetilde{C}_i + \delta\widetilde{C}_i, \\ {}^{k+1}_{m+1}\phi &= {}^{k+1}_{m}\phi + \delta\phi. \end{aligned} \tag{2.17}$$

Depending on the electrode kinetics, the current density I_i may be a function of $\widetilde{C}_i$ and ϕ and can be further linearized at iteration $m+1$ and time increment $k+1$ as

$$I_i\left({}^{k+1}_{m+1}\widetilde{C}_i, {}^{k+1}_{m+1}\phi\right) = I_i\left({}^{k+1}_{m}\widetilde{C}_i, {}^{k+1}_{m}\phi\right) + \frac{\partial I_i}{\partial\, {}^{k+1}_{m}\widetilde{C}_i}\delta\widetilde{C}_i + \frac{\partial I_i}{\partial\, {}^{k+1}_{m}\phi}\delta\phi. \tag{2.18}$$

Substituting Equations (2.16) $-$ (2.18) into Equation (2.15), the discretized and linearized weak form of the governing electro-diffusion equations can be written as

$$\begin{aligned} \mathscr{A}\left(u_i, \delta\widetilde{C}_i, v, \delta\phi\right) = \sum_{i=1}^{n}\Bigg\{ & \left(u_i, \frac{\delta\widetilde{C}_i}{\Delta t}\right)_{\Omega_l} + \left(\nabla u_i, D_i\nabla\delta\widetilde{C}_i\right)_{\Omega_l} \\ & + \left(\nabla u_i, \frac{D_i z_i F}{R^* T}\left(\delta\widetilde{C}_i\nabla\, {}^{k+1}_{m}\phi + {}^{k+1}_{m}\widetilde{C}_i\nabla\delta\phi\right)\right)_{\Omega_l} \\ & + \left(v, z_i\delta\widetilde{C}_i\right)_{\Omega_l} - \left(u_i, \frac{\partial I_i}{\partial\, {}^{k+1}_{m}\widetilde{C}_i}\frac{\delta\widetilde{C}_i}{z_i F} + \frac{\partial I_i}{\partial\, {}^{k+1}_{m}\phi}\frac{\delta\phi}{z_i F}\right)_{\Gamma_{\text{int}}}\Bigg\}, \\ \mathscr{L}\left(u_i, v\right) = \sum_{i=1}^{n}\Bigg\{ & \left(u_i, \frac{{}^{k}C_i - {}^{k+1}_{m}\widetilde{C}_i}{\Delta t}\right)_{\Omega_l} - \left(\nabla u_i, D_i\nabla\, {}^{k+1}_{m}\widetilde{C}_i\right)_{\Omega_l} \\ & - \left(\nabla u_i, \frac{D_i z_i F}{R^* T}\, {}^{k+1}_{m}\widetilde{C}_i\nabla\, {}^{k+1}_{m}\phi\right)_{\Omega_l} - \left(v, z_i\, {}^{k+1}_{m}\widetilde{C}_i\right)_{\Omega_l} \\ & + \left(u_i, \frac{1}{z_i F}I_i\left({}^{k+1}_{m}\widetilde{C}_i, {}^{k+1}_{m}\phi\right)\right)_{\Gamma_{\text{int}}}\Bigg\}, \end{aligned} \tag{2.19}$$

where $\mathscr{A}$ denotes the left-hand side of governing equations and $\mathscr{L}$ denotes the right-hand side, and $(u,v)_\Omega = \int_\Omega uv\, d\Omega$ denotes the inner product of u and v measured in the domain Ω.

2.3.3 Under-relaxation technique

The condition that chemical species concentrations must be positive or zero is known in transport modeling, involving diffusion-advection and/or reaction, as the non-negativity constraint [32, 101]. For a set of nonlinear algebraic equations, such as chemical equilibrium equations (2.13), there will be a number of solutions, but usually only one solution satisfies the non-negativity constraint. A simple method for ensuring non-negativity is to set the initial values of concentration fields to be positive and then scale back corrections that would induce any unknown variable to be negative [20]. This technique in numerical analysis is known as under-relaxation and is widely used in geochemical reaction modeling. For the sake of completeness, in this section we detail the implementation of the under-relaxation technique.

We express Equation (2.13) as a residual $\mathscr{R}_r$ at iteration $m+1$ and time increment $k+1$ as

$$\mathscr{R}_r\left({}^{k+1}_{m+1}\widehat{C}_j\right) = K_r \prod_p \left(\widetilde{C}_p + \sum_{l=1}^{n_r} \omega_{lp}\nu_{lp}\,{}^{k+1}_{m+1}\widehat{C}_l\right)^{\nu_{rp}} - \prod_q \left(\widetilde{C}_q + \sum_{l=1}^{n_r} \omega_{lq}\nu_{lq}\,{}^{k+1}_{m+1}\widehat{C}_l\right)^{\nu_{rq}}. \tag{2.20}$$

Henceforth, we will omit the left superscript because all concentrations are considered at time increment $k+1$. Using the Newton-Raphson method, ${}_{m+1}\widehat{C}_i$ can be determined as

$${}_{m+1}\widehat{C}_i = {}_m\widehat{C}_i + \Delta\widehat{C}_i. \tag{2.21}$$

$$\Delta\widehat{C}_i = -\left[\frac{\partial \mathscr{R}_r}{\partial\, {}_m\widehat{C}_i}\right]^{-1} \mathscr{R}_r\left({}_m\widehat{C}_j\right). \tag{2.22}$$

Substituting Equation (2.21) into Equation (2.12), the corrected concentrations C_i at iteration $m+1$ are given by

$${}_{m+1}C_i = \widetilde{C}_i + \sum_{r=1}^{n_r} \omega_{rj}\nu_{rj}\left({}_{m+1}\widehat{C}_r\right) = \widetilde{C}_i + \sum_{r=1}^{n_r} \omega_{rj}\nu_{rj}\left({}_m\widehat{C}_r + \Delta\widehat{C}_r\right), \tag{2.23}$$

and the increment of corrected concentration variables is given by

$$\Delta C_i = {}_{m+1}C_i - {}_{m}C_i = {}_{m+1}C_i - \left(\widetilde{C}_i + \sum_{r=1}^{n_r} \omega_{rj} \nu_{rj} \left({}_{m}\widehat{C}_r \right) \right) = \sum_{r=1}^{n_r} \omega_{rj} \nu_{rj} \Delta \widehat{C}_r. \tag{2.24}$$

Combining Equations (2.22) – (2.24), we can directly obtain the increment in corrected concentrations as

$$\Delta C_i = - \sum_{r=1}^{n_r} \omega_{rj} \nu_{rj} \left[\frac{\partial \mathscr{R}_r}{\partial \, {}_{m}\widehat{C}_i} \right]^{-1} \mathscr{R}_r \left({}_{m}\widehat{C}_j \right). \tag{2.25}$$

If ${}_{m}C_i + \Delta C_i < 0$, the non-negativity constraint will not be satisfied, leading to nonphysical concentrations. To resolve this issue, we define an under-relaxation factor δ_{UR} as

$$\frac{1}{\delta_{\text{UR}}} = \max \left\{ 1, -\frac{\Delta C_1}{\frac{1}{2} \, {}_{m}C_1}, -\frac{\Delta C_2}{\frac{1}{2} \, {}_{m}C_2}, \cdots, -\frac{\Delta C_n}{\frac{1}{2} \, {}_{m}C_n} \right\}, \tag{2.26}$$

and compute the corrected concentrations as

$${}_{m+1}C_i = {}_{m}C_i + \delta_{\text{UR}} \Delta C_i. \tag{2.27}$$

Thus, in the under-relaxation technique, the net change in corrected concentrations at any iteration $m+1$ is allowed to reduce the previous corrected concentration ${}_{m}C_i$ by no more than half the value. This ensures that the concentrations at any iteration do not become negative. The pseudocode for the modified Newton-Raphson method at $m+1$ iteration is given in Algorithm 2.

Algorithm 2: The modified Newton-Raphson method using the under-relaxation technique. Note that ε denotes the maximum absolute value of net concentration change and Tol $= 10^{-10}$ is the chosen numerical tolerance.

input : ${}_m\varepsilon$, ${}_mC_i$, and ${}_m\widehat{C}_i$
output : ${}_{m+1}\varepsilon$, ${}_{m+1}C_i$, and ${}_{m+1}\widehat{C}_i$
parameter: Tol, K_i, ν_{ij}, and ω_{ij}

if ${}_m\varepsilon >$ Tol **then**
  solve `Chemical equilibrium equations;` `// Eq.(2.13)`
    compute $\Delta\widehat{C}_i$; `// Eq.(2.21)`
  compute ΔC_i ; `// Eq.(2.25)`
  update δ_{UR} ; `// Eq.(2.26)`
  return ${}_{m+1}\widehat{C}_i = {}_m\widehat{C}_i + \delta_{\text{UR}}\Delta\widehat{C}_i$;
  return ${}_{m+1}C_i = {}_mC_i + \delta_{\text{UR}}\Delta C_i$;
  return ${}_{m+1}\varepsilon = \max\{|\delta_{\text{UR}}\Delta C_1|, |\delta_{\text{UR}}\Delta C_2|, \cdots, |\delta_{\text{UR}}\Delta C_n|\}$;
else
  return ${}_{m+1}\widehat{C}_i = {}_m\widehat{C}_i$ and ${}_{m+1}C_i = {}_mC_i$;
  break
end

2.4 Numerical Examples

In this section, we will illustrate the accuracy and robustness of the SNIA for solving the multi-species reactive transport in the solution phase during localized corrosion. We also establish the applicability of the approach for different material/chemical systems by considering two different types of steel: a generic carbon steel and Fe-Cr binary alloys.

2.4.1 Corrosion of Carbon Steel

We consider 1D and 2D models of localized corrosion in a cavity or crevice. To demonstrate the accuracy of the proposed approach, we evaluate the error in steady-state species concentrations against the solution obtained from Sharland's approach [131]. Due to the highly nonlinear nature of the localized corrosive dissolution problem, numerical convergence may not be guaranteed for all values of electrochemical and crevice geometry parameters. Therefore, to demonstrate robustness of the SNIA, we perform parametric studies in 2D by varying the over-potential and crevice length L examining the variation of electrochemical variables, specifically, corrosion current density and electrolyte pH.

2.4.1.1 Electrochemical Reactions and Kinetics

Sharland and Tasker [133] modeled the localized corrosion of carbon steel by considering six ionic species: Fe^{2+}, $FeOH^{+}$, Na^{+}, Cl^{-}, H^{+}, and OH^{-}; these species are numbered in this order from $i = 1$ to 6 and denoted by the right subscript of variables. Except for Fe^{2+} and $FeOH^{+}$ that are produced from electrochemical reactions, all other species exist initially in 10^{-3} M NaCl solution at room temperature $T = 25^{\circ}$C. We consider three electrode reactions taking place on Γ_{int} and two chemical reactions in Ω_l. The anodic reaction involving the oxidation of iron on Γ_a is

$$\text{Fe} \rightarrow \text{Fe}^{2+} + 2\,\text{e}^{-}. \tag{2.28}$$

As noted in [153], the above reaction follows Tafel kinetics defined in Equation (2.9). The cathodic reaction involving the reduction of water on Γ_c also follows Tafel kinetics and is given by

$$H_2O + e^- \rightarrow H + OH^-. \tag{2.29}$$

The other cathodic reaction involving the hydrogen discharge on Γ_c is

$$2H^+ + 2e^- \rightarrow H_2\uparrow. \tag{2.30}$$

The hydrogen discharge reaction shows a first order dependence on the concentration of H^+ and its kinetics can be expressed as [154]

$$I_5 = \hat{I}_5 C_5 \exp\left(\frac{\alpha_5 F \eta}{R^* T}\right). \tag{2.31}$$

The two homogeneous chemical reactions considered in this model are:

$$Fe^{2+} + H_2O \rightleftharpoons FeOH^+ + H^+, \tag{2.32}$$

$$H_2O \rightleftharpoons H^+ + OH^-, \tag{2.33}$$

and the corresponding equilibrium constants are denoted by K_1 and K_2, respectively. All parameters used in the corrosion model of carbon steel are listed in Table 2.1.

Table 2.1: Model parameters for multi-ionic species reactive transport system of corrosion in carbon steel.

Parameter	Value [Unit]	Reference	Parameter	Value [Unit]	Reference
F	$96,485.3$ [C/mol]	–	R^*	8.314 [J/mol/K]	–
T	298.15 [K]	[133]	ϕ_{M}	$-0.1, -0.2, -0.4$ [V]	[133]
K_1	1.625×10^{-7} [M]	[89]	K_2	10^{-14} [M^2]	–
D_1	1.0×10^{-9} [m^2/s]	[133]	D_2	1.0×10^{-9} [m^2/s]	[133]
D_3	1.0×10^{-9} [m^2/s]	[133]	D_4	1.0×10^{-9} [m^2/s]	[133]
D_5	9.3×10^{-9} [m^2/s]	[133]	D_6	5.3×10^{-9} [m^2/s]	[133]
z_1	$+2$ [$-$]	–	z_2	$+1$ [$-$]	–
z_3	$+1$ [$-$]	–	z_4	-1 [$-$]	–
z_5	$+1$ [$-$]	–	z_6	-1 [$-$]	–
C_1^∞	0 [M]	[131]	C_2^∞	0 [M]	[131]
C_3^∞	10^{-3} [M]	[133]	C_4^∞	10^{-3} [M]	[133]
C_5^∞	10^{-7} [M]	[133]	C_6^∞	10^{-7} [M]	[133]
$\hat{I}_1$	2.7×10^{11} [A/m^2]	[153]	α_1	1.0 [$-$]	[153]
$\hat{I}_5$	2.0×10^{-7} [Am/mol]	[154]	α_5	-0.5 [$-$]	[154]
$\hat{I}_6$	-8.0×10^{-10} [A/m^2]	[154]	α_6	-0.5 [$-$]	[154]

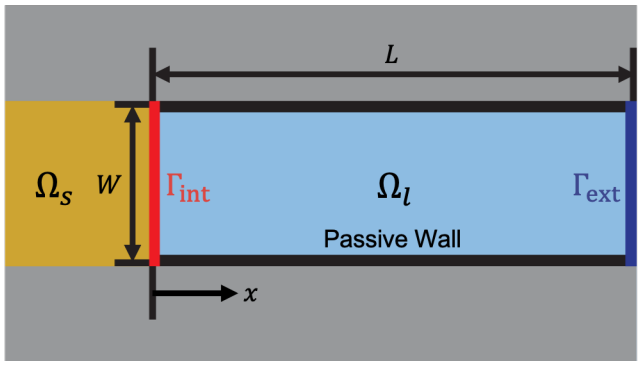

Figure 2.2: Schematic diagram of the one-dimensional domain for cavity corrosion of carbon steel Ω_s (gold) in NaCl solution Ω_l (light blue). Anodic and cathodic boundaries coincide with Γ_{int} (red line). The gray region is insulated from the electrolyte solution by passive walls (thick black lines).

2.4.1.2 1D Cavity corrosion

Following Sharland and Tasker [133], we model the corrosion environment within a rectangular cavity ($L \times W = 2$ mm $\times$ 10 μm) shown in Figure 2.2. Although the domain is two-dimensional, the ion transport is restricted to one dimension by assuming zero flux conditions at passive sidewalls and that anode Γ_a and cathode Γ_c boundaries coincide with Γ_{int}. Therefore, we perform simulations on a 1D domain of length $L = 2$ mm and discretize it using quadratic (three-noded) line elements with an element length of 1 μm.

Because corrosive dissolution is slow compared to ion migration, the steady-state ion concentrations and electrical potential in the cavity can be used to estimate the corrosion rate. Therefore, we assess the accuracy of the SNIA in predicting the steady-state concentrations and corrosion current density against those obtained from Sharland's approach (see Appendix B). We define the Normalized Root Mean Square (NRMS) error in species concentrations in the electrolyte domain Ω_l as

$$\varepsilon_{\text{NRMS}} = \frac{\sqrt{\frac{1}{n_e}\sum_{i=1}^{n_e}(C_i - \bar{C}_i)^2}}{\bar{C}_{max} - \bar{C}_{min}}, \tag{2.34}$$

where C_i and $\bar{C}_i$ are ionic concentrations at the i^{th} node computed from SNIA and Shar-

land's approach, respectively. We evaluate the corrosion current density corresponding to iron dissolution at Γ_{int} as

$$I = -z_1 D_1 F \left(\nabla C_1 + \frac{z_1 F}{R^* T} C_1 \nabla \phi \right) \cdot \mathbf{n}. \tag{2.35}$$

We first solve the steady-state ion transport equations (i.e., without the time derivative term $\dot{\tilde{C}}_i$ in Equation (2.6)) and the chemical equilibrium equations using the SNIA. In Figure 2.3, we show the steady-state concentrations and electrical potential along the cavity length computed from Sharland's approach and SNIA. It is evident that the electrical potential profiles from both approaches match exactly as shown in Figure 2.3(b), which indicates that the uncorrected concentrations correspond with the true electrical potential. The concentration correction based on homogeneous chemical reactions is charge balanced, so it does not affect the potential field. The steady-state ionic concentrations computed using Sharland's approach and SNIA presented in Figure 2.3(a) and Figure 2.3(d) show similar trends, except for the discrepancy in the predicted values of $FeOH^+$ and H^+. Table 2.2 lists the NRMS errors in concentrations of the six ionic species considered in this example compared to Sharland's results. The current density computed from SNIA is 5651.09 A/m^2 and that from Sharland's approach is 5645.49 A/m^2, thus the relative error in predicted current density is 0.099%. While the errors in current density and Fe^{2+} concentration are negligible, the NRMS errors in concentrations of $FeOH^+$ and H^+ are significant (about 20% and 33% respectively). Because the chemical reactions in Equations (2.32) and (2.33) occur must faster compared to ion transport, the SNIA applied to steady-state transport equations does not accurately describe the concentrations of reaction products $FeOH^+$ and H^+. However, the SNIA is still reasonably accurate for capturing the evolution of the corrosion interface based on the quasi-steady-state assumption.

We next solve the time-dependent transport equations and chemical equilibrium equations using the SNIA and determine the steady-state concentrations and potential using different sizes of time increment $\Delta t = \{1, 10, 10^2, 10^3, 10^4, 10^5, 10^6\}$ seconds. We ran all

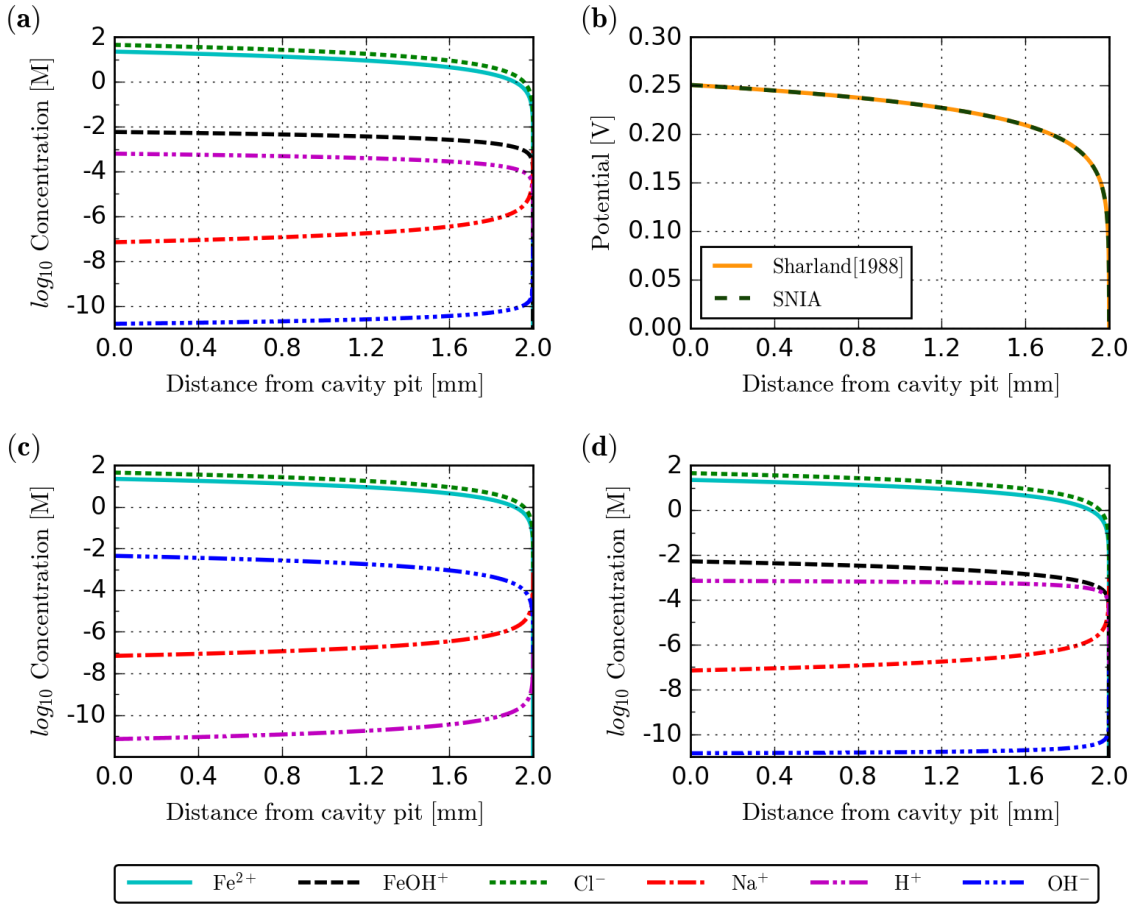

Figure 2.3: Numerical results of multi-ionic species concentration at steady-state for 1D cavity corrosion of carbon steel with $\phi_{\mathrm{M}} = -0.2$ V: (a) Benchmark concentration profiles along the cavity length [133]; (b) Comparison of potential profile along cavity length computed from Sharland's approach and SNIA; (c) Uncorrected concentration profiles along the cavity length computed from SNIA with the size of time increment $\Delta t \to \infty$; (d) Corrected concentration profiles along the cavity length computed from SNIA with the size of time increment $\Delta t \to \infty$.

Table 2.2: The normalized root mean square (NRMS) errors of steady-state ionic concentrations by comparing SNIA results to Sharland's for multi-ionic species reactive transport within 1D cavity corrosion of carbon steel.

Variable	C_1	C_2	C_3	C_4	C_5	C_6
$\varepsilon_{\mathrm{NRMS}}$ (%)	0.059	20.455	0.058	0.0003	32.550	0.193

simulations until a final time $t^{\infty} = 3 \times 10^6$ seconds to attain steady-state. In Figure 2.4(a) we calculate error between the steady-state numerical solution obtained from Sharland's approach [131] and the t^{∞}-solution obtained from the SNIA for transient transport and equilibrium reaction equations. As we increase the size of time increment, the error in $FeOH^+$ and H^+ concentrations in the SNIA varies non-monotonically (i.e., error increases till $\Delta t = 10^3$ seconds and then decreases); the errors in all other ion concentrations are relatively small. Decreasing the size of time increment to $\Delta t = 1$ seconds decreases the error in $FeOH^+$ and H^+ concentrations to less than 2%. In Figures 2.4(c) and (d), we further compare the predicted steady-state concentrations of $FeOH^+$ and H^+ along the cavity length using time increment sizes $\Delta t = 1$ and 10^3 seconds against Sharland's results. For this example, the characteristic diffusion time scale $t_d = L^2/4D_5 \approx 100$ seconds. This time-step convergence study suggests that $\Delta t \leq 0.01 \times t_d$ yields adequately accurate results. We next evaluate the steady-state corrosion current densities for the dissolution of iron at Γ_{int} using Equation (2.35) for different sizes of time increment. It is evident from Figure 2.4(b) that the maximum error in current density computed from Sharland's approach and SNIA is about 0.3%, which is negligible. This study suggests that while the SNIA is accurate for predicting corrosion rate using larger sizes of time increment, using smaller time increment sizes ($\Delta t \leq 10$ seconds) is necessary to capture the steady-state concentrations of all ionic species accurately and to obtain results that are consistent with Sharland's results.

2.4.1.3 2D Crevice Corrosion

Using the same chemical system and time-dependent mass transport, we perform simulations of the crevice corrosion problem on a 2D domain shown in Figure 2.1. We assume a constant crevice width $w = 2$ μm and different crevice lengths $l = \{0, 2.5, 5, 7.5, 10, 12.5, 15\}$ μm. Following the example in [46, 124], we take the dimension of the rectangular electrolyte region above the crevice to be $W \times L = 42 \times 21$ μm^2. The domain Ω_l is then discretized using quadratic (six-noded) triangular elements with the leg length

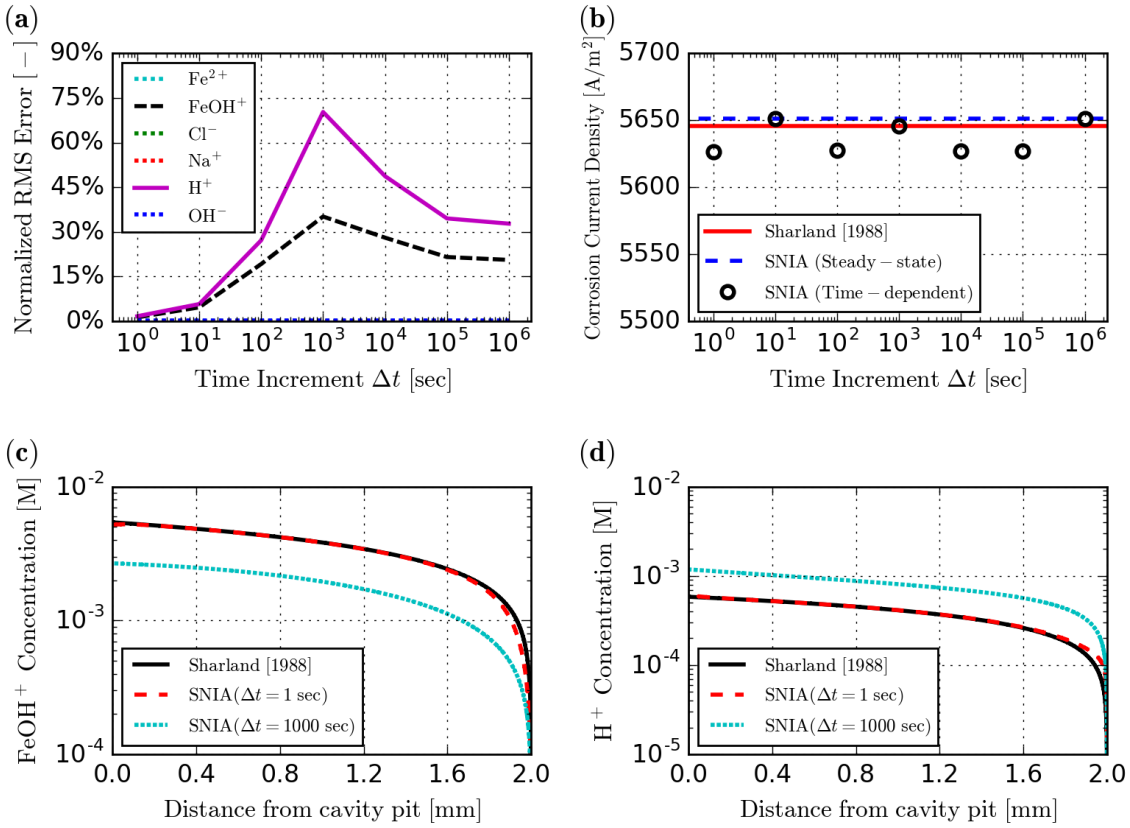

Figure 2.4: Numerical accuracy study with respect to time increment size Δt. (a) Normalized Root Mean Square (NRMS) error of concentrations obtained from SNIA compared to Sharland's approach. Lines representing NRMS errors of Fe^{2+}, Na^+, Cl^- and OH^- concentrations overlap on the blue dotted line for OH^-; (b) Corrosion current density corresponding to iron dissolution at Γ_{int}. Comparison of (c) $FeOH^+$ and (d) H^+ concentration distributions computed from different methods within the cavity using different time increment sizes.

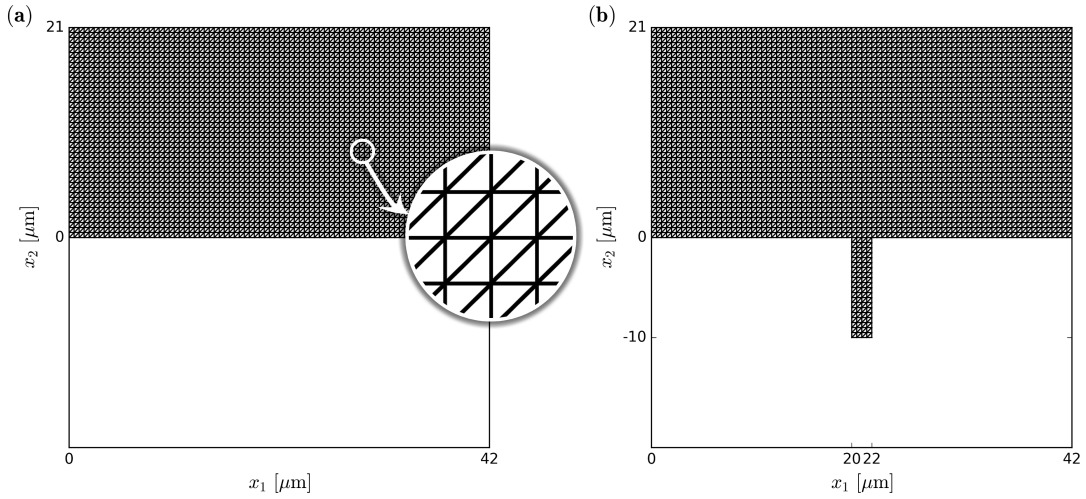

Figure 2.5: Structured finite element meshes consisting of quadratic (six-noded) triangules are used to discretize the computational domain for localized corrosion problem with different crevice lengths: (a) $l = 0$; (b) $l = 10$ μm

0.5 μm. The structured finite element mesh of domains with $l = 0$ and 10 μm are shown in Figures 2.5(a) and (b), respectively. For this example, the characteristic diffusion time scale $t_d = L^2/4D_5 \approx 10^{-2}$ seconds. Therefore, we take $\Delta t = 0.01 \times t_d = 10^{-4}$ seconds to ensure sufficient accuracy.

We first show the accuracy of the SNIA relative to the Sharland's approach for predicting steady-state concentrations and electrical potential within a 2D geometry. We take the metal potential $\phi_{\mathrm{M}} = -0.2$ V. The steady-state results for the concentration of Fe^{2+}, electrical potential, the concentration of $FeOH^+$ and the pH ($= -log_{10}[H^+]$, where $[H^+]$ denotes the concentration of hydrogen ion in the unit of mol/L) with $l = 0$ and 10 μm are plotted in Figures 2.6(a)–(d) and 2.7(a)–(d), respectively. Because there can be larger discrepancies in the steady-state concentration of $FeOH^+$ and H^+ from SNIA and Sharland's approach, we plot the corresponding relative errors within the entire domain in Figures 2.6(e)–(f) and 2.7(e)–(f). We find that relative errors of $FeOH^+$ and H^+ concentrations are negligible except for the limited region near the anode boundary; consequently, the corresponding NRMS errors are sufficiently small, as noted in subfigures (e) and (f). This study indicates

that the 2D steady-state results obtained from SNIA are consistent with those obtained from Sharland's approach, so long as the size of time increment is chosen appropriately.

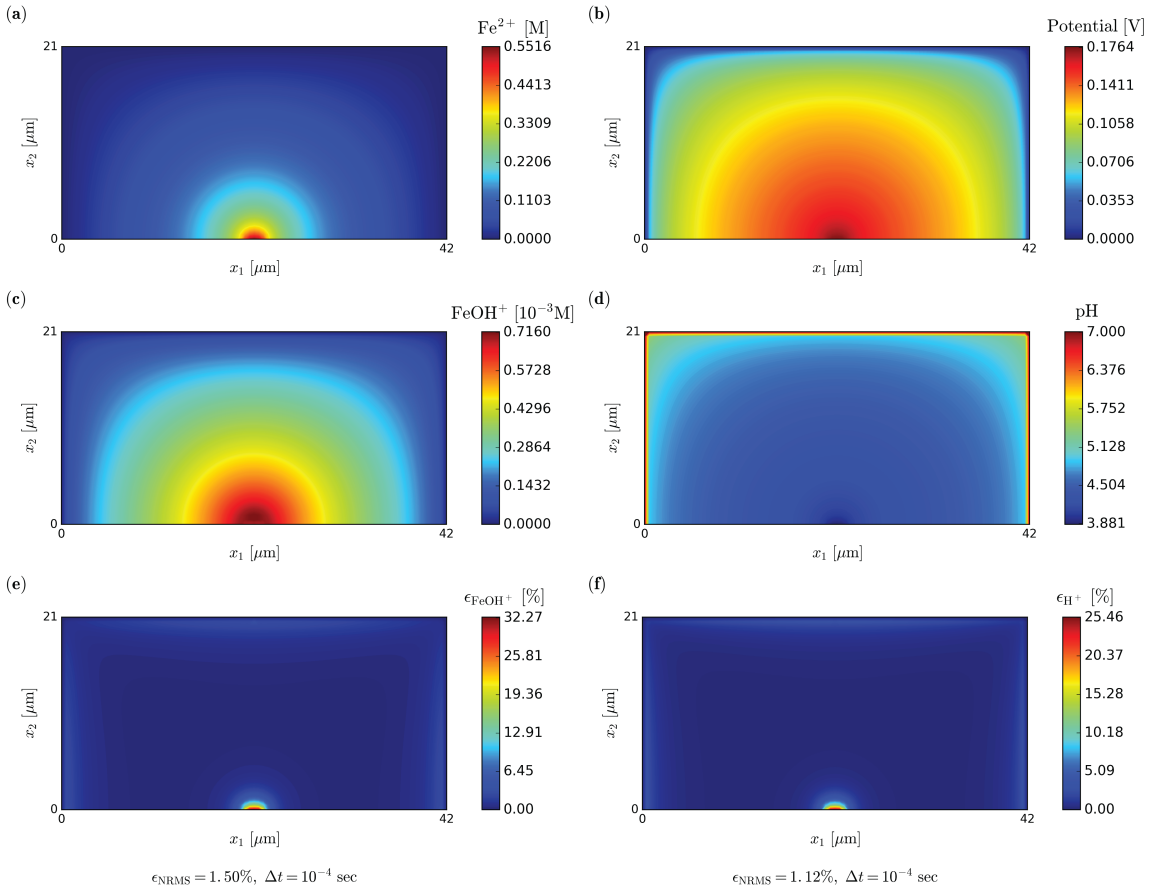

Figure 2.6: Concentration and potential profiles predicted by the SNIA for 2D crevice corrosion of carbon steel with crevice length $l = 0$ and $\phi_M = -0.2$ V. (a) Concentration of Fe^{2+}; (b) Potential; (c) Concentration of $FeOH^+$; (d) pH $= -log_{10}[H^+]$; (e) Relative error of $FeOH^+$ concentration comparing SNIA to Sharland's approach; (f) Relative error of H^+ concentration comparing SNIA against Sharland's approach.

We next perform a parametric study to the variation of steady-state corrosion current density I and electrolyte pH at the crevice tip in relation to crevice length L for three different metal potentials. The results from this study are shown in Figure 2.8. For each different crevice length L, we generate an appropriate finite element mesh to capture the domain geometry and use the SNIA to determine the steady-state values of relevant electrochemical variables. From Figure 2.8(a) it is evident that the corrosion current density decreases (exponentially) with crevice length, which is in good agreement with the results presented by

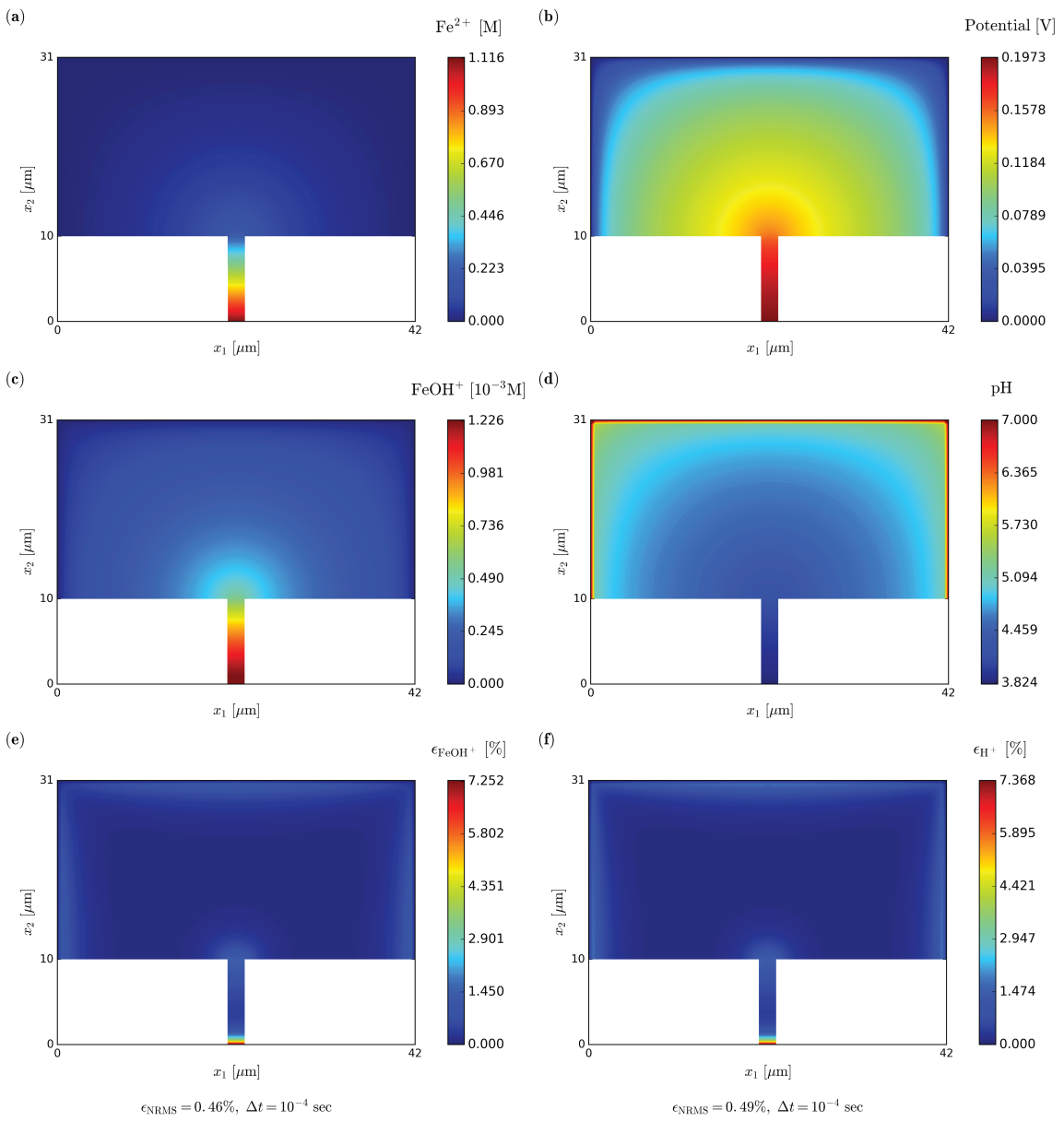

Figure 2.7: Concentration and potential profiles predicted by the SNIA for 2D crevice corrosion of carbon steel with crevice length $l = 10$ μm and $\phi_M = -0.2$ V. Note that only electrochemical variables inside the liquid phase are plotted for all contours shown in this chapter. (a) Concentration of Fe^{2+}; (b) Potential; (c) Concentration of $FeOH^+$; (d) pH $= -log_{10}[H^+]$; (e) Relative error of $FeOH^+$ concentration comparing SNIA to Sharland's approach; (f) Relative error of H^+ concentration comparing SNIA against Sharland's approach.

Sharland and Tasker [133]. This is because increasing the crevice length will decrease the concentration gradient of Fe^{2+}, which decreases the corrosion current density. Also, as expected the corrosion current density is larger for larger metal potential. From Figure 2.8(b) we find that pH at the crevice tip decreases with crevice length. This result indicates that an increase of the geometry factor l^2/w of the crevice will lead to a drop in pH within the crevice, which is consistent with the analysis done by Yaya et al. [171]. Due to the highly nonlinear nature of the corrosive dissolution problem, numerical convergence in Sharland's approach is not guaranteed for all values of electrochemical and crevice geometry parameters. For example, if we take a large value of metal potential $\phi_{\mathrm{M}} = -0.1$ V, the simulation using Sharland's approach does not converge; whereas, there is no apparent convergence issue with the SNIA. We find that solving the nonlinear algebraic (chemical reaction) equations separately from the partial differential (mass transport) equations is more robust with regard to numerical convergence, demonstrating the advantage of the proposed SNIA over Sharland's approach.

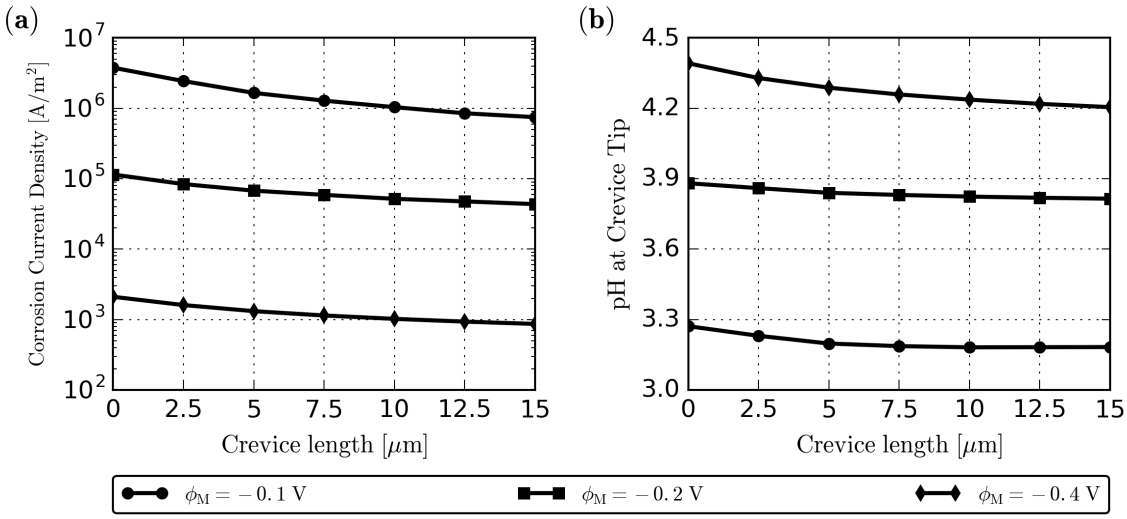

Figure 2.8: Parametric sensitivity of corrosion variables with respect to crevice length L and metal potential ϕ_{M}: (a) Corrosion current density corresponding to iron dissolution at Γ_a; (b) pH at crevice tip.

2.4.2 Corrosion of Fe-Cr Alloy

As noted by Walton [163], the main drawback of Sharland's approach is that governing equations generally must be rederived if a new electrochemical system is considered. However, this issue can be effectively avoided using the SNIA. To demonstrate the applicability of the SNIA, we next consider the crevice corrosion of Fe-Cr binary alloys, which involves additional ions and reactions. To validate our model, we further perform parametric studies by varying the chemical compositions of alloys and compare our results to experimental data reported by Bogar and Fujii [22].

2.4.2.1 Electrochemical Reactions and Kinetics

Bogar and Fujii performed experiments to demonstrate the influence of chromium on the solution chemistry within an artificial crevice [22]. As shown in Figure 2.9(a), the crevice was constructed using the disk with radius $r = 0.4375$ inch on one side and a 2×2 inch^2 acrylic plastic plate on the other. The disk was made of Fe-Cr binary alloys with different weight fractions of chromium. The metal disk and the plastic plate were mounted vertically and placed at a distance of 0.015 inch by inserting a thickness gauge in between. The edges and the back surface of the disk were shielded from the electrolyte by pouring sealing cement. When the sealing cement dried out, the entire setup was placed into a container filled with 3.5% NaCl solution under room temperature $T = 25^{\circ}$C. After removing the thickness gauge, the crevice with the dimensions $l \times w \times d = 0.9 \times 0.4 \times 0.015$ inch^3 was formed, which was a rectangular slot open to the bulk solution at top and bottom ends. A potentiostat was used to polarize the iron/chromium anode and the platinum cathode. The potential on the anode was maintained at 0.3 V throughout the experiment. The reference and cathodic electrodes were placed far enough away from the crevice to avoid possible interference.

To model the crevice corrosion of Fe-Cr binary alloys, here we consider the simplified electrochemical system proposed by Stroe et al. [145]. In addition to six ionic species for

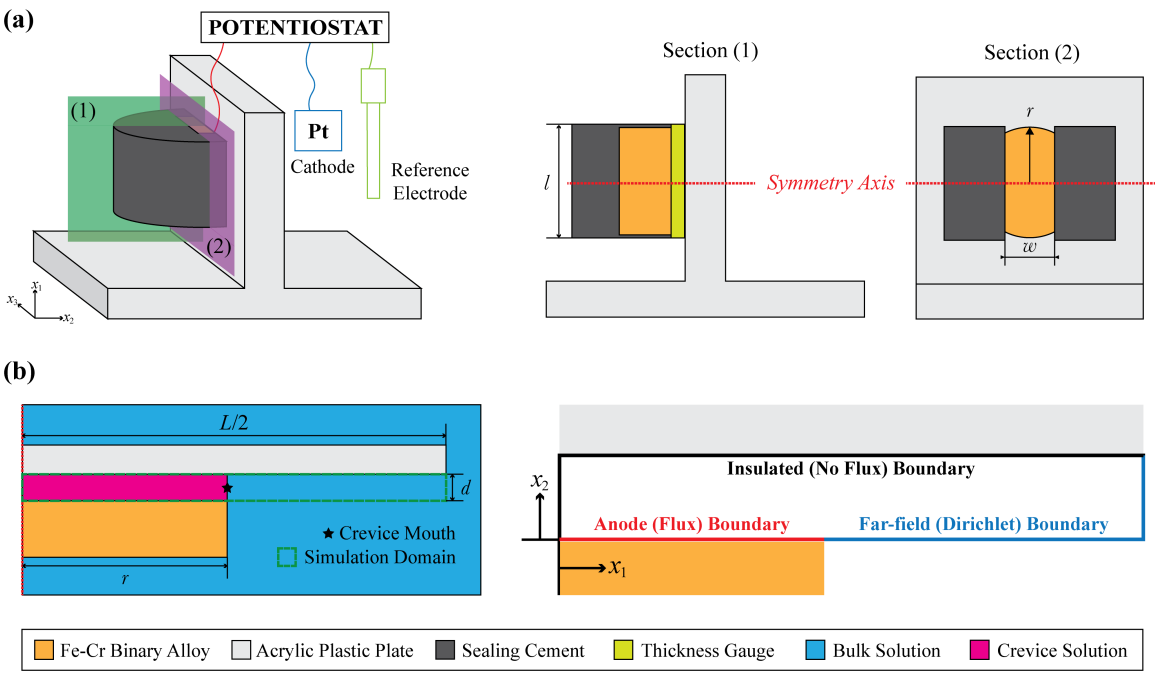

Figure 2.9: Schematic diagrams of crevice corrosion of Fe-Cr binary alloy: (a) Bogar and Fujii's experiment setup and sectional views; (b) Idealized domain and boundary conditions of the 2D artificial crevice between the metal disk and the acrylic plastic plate.

localized corrosion of carbon steel: Fe^{2+}, $FeOH^{+}$, Na^{+}, Cl^{-}, H^{+}, and OH^{-}, we also consider another four ions: Cr^{3+}, $FeCl^{+}$, $CrOH^{2+}$, and $CrCl^{2+}$; all these species are numbered in this order from $i = 1$ to 10 and denoted by the right subscript of variables in this study. Because we only focus on the solution chemistry within the crevice, cathodic reactions are neglected. In addition to the oxidation of iron, we consider the following anodic reaction involving the oxidation of chromuim on Γ_a

$$\mathrm{Cr} \rightarrow \mathrm{Cr}^{3+} + 3\,\mathrm{e}^{-}. \tag{2.36}$$

Bogar and Fujii reported the calculated weights of ferrous and chromium content within the crevice by integrating the current/time curves recorded during the experiment. Sharland [132] used the calculated data to estimate the current density of alloys I_{a} by assuming a uniform distribution of it over the electrode surface, as tabulated in Table 2.3. According to [145], it is assumed that the current density for the dissolution of binary alloys I_{a} is the

Table 2.3: Current densities of Fe-Cr binary alloys (I_a) for different weight fractions of chromium (f_7) estimated by Sharland [132].

f_7	1%	10%	15%	20%	25%
I_a (A/m^2)	45.0	27.0	20.0	5.7	2.5

sum of current densities for the oxidation of iron and chromium, which are in proportion to their weight fractions f_1 and f_7, respectively. Therefore, electrode kinetics of oxidation of iron and chromium separately can be expressed as

$$I_1 = f_1 I_a, \tag{2.37}$$

$$I_7 = f_7 I_a. \tag{2.38}$$

In addition to homogeneous chemical reactions (2.32) and (2.33), we consider another three reactions taking place in Ω_l

$$Fe^{2+} + Cl^- \rightleftharpoons FeCl^+, \tag{2.39}$$

$$Cr^{3+} + H_2O \rightleftharpoons CrOH^{2+} + H^+, \tag{2.40}$$

$$Cr^{3+} + Cl^- \rightleftharpoons CrCl^{2+}, \tag{2.41}$$

and the corresponding equilibrium constants are denoted by K_3, K_4, and K_5, respectively. All parameters used in the corrosion model of Fe-Cr binary alloys are listed in Table 2.4.

2.4.2.2 2D Crevice Corrosion

As shown in Figure 2.9(b), we perform simulations on the crevice corrosion of Fe-Cr binary alloys with different weight fractions of chromium $f_7 = \{1\%, 10\%, 15\%, 20\%, 25\%\}$ on a 2D rectangular domain with the dimension $0.5L \times d = 1 \times 0.015$ inch^2. The geometry is simplified from the experimental setup based on the following assumptions:

Table 2.4: Model parameters for multi-ionic species reactive transport system of crevice corrosion in Fe-Cr binary alloys.

Parameter	Value [Unit]	Reference	Parameter	Value [Unit]	Reference
D_1	7.1×10^{-10} [m^2/s]	[31]	D_2	7.5×10^{-10} [m^2/s]	[31]
D_3	1.33×10^{-9} [m^2/s]	[31]	D_4	2.03×10^{-9} [m^2/s]	[31]
D_5	9.31×10^{-9} [m^2/s]	[31]	D_6	5.3×10^{-9} [m^2/s]	[31]
D_7	5.9×10^{-10} [m^2/s]	[31]	D_8	1.0×10^{-9} [m^2/s]	[31]
D_9	7.3×10^{-10} [m^2/s]	[31]	D_{10}	1.0×10^{-9} [m^2/s]	[31]
z_1	$+2$ [$-$]	$-$	z_2	$+1$ [$-$]	$-$
z_3	$+1$ [$-$]	$-$	z_4	-1 [$-$]	$-$
z_5	$+1$ [$-$]	$-$	z_6	-1 [$-$]	$-$
z_7	$+3$ [$-$]	$-$	z_8	$+1$ [$-$]	$-$
z_9	$+2$ [$-$]	$-$	z_{10}	$+2$ [$-$]	$-$
C_1^{∞}	10^{-5} [M]	[145]	C_2^{∞}	1.625×10^{-8} [M]	[145]
C_3^{∞}	0.6 [M]	[132]	C_4^{∞}	0.6 [M]	[132]
C_5^{∞}	2×10^{-6} [M]	[132]	C_6^{∞}	5×10^{-9} [M]	[132]
C_7^{∞}	10^{-5} [M]	[145]	C_8^{∞}	1.59×10^{-13} [M]	[145]
C_9^{∞}	6.92×10^{-10} [M]	[145]	C_{10}^{∞}	1.95×10^{-10} [M]	[145]
K_3	0.692 [M^{-1}]	[145]	K_4	1.59×10^{-4} [M]	[145]
K_5	0.195 [M^{-1}]	[145]			

1. We neglect the shape effect of the metal disk and assume the dissolution of Fe-Cr alloys to be uniform, which decreases the dimension of the problem from three to two;

2. We enforce bulk concentrations of ionic species at the far-field boundary of the idealized domain shown in Figure 2.9(b). Thus, we neglect the changes to bulk solution concentrations caused by the small amount of ferrous and chromium ions diffusing from the crevice;

3. We assume the left boundary of the domain to be insulated by taking the advantage of the four-fold symmetry of the crevice in the experimental setup.

The domain is then discretized using quadratic (six-noded) triangular elements with the leg length 20 μm. For this example, the characteristic diffusion time scale $t_d = d^2/4D_5 \approx 10^2$ seconds. Therefore, we take $\Delta t = 0.01 \times t_d = 1$ second to ensure sufficient accuracy. Based on the experimental results, we chose to run all simulations until a final time $t^\infty = 5$ hours $= 1.8 \times 10^4$ seconds to attain the experimental steady state. We first investigate the electrochemistry of crevice corrosion for Fe-15Cr binary alloy (i.e., $f_7 = 15\%$). The simulation results for the pH and the concentrations of Fe^{2+}, Cr^{3+}, $FeCl^+$, $CrCl^{2+}$, $CrOH^{2+}$, Na^+, and Cl^- are shown in Figure 2.10. After polarizing the crevice, Fe and Cr dissolve into solution as Fe^{2+} and Cr^{3+} ions, which increases their concentration in the crevice, as evident from Figures 2.10(a) and (b). The accumulation of these metal ions within the crevice is accompanied by the migration of Cl^- ions from the bulk solution into the crevice and of Na^+ ions from the crevice into the bulk solution, as shown in Figures 2.10(g) and (h). This ion migration helps maintain the local electro-neutrality condition. Along with the mass transport of ionic species, chemical reactions producing $FeCl^+$, $CrCl^{2+}$, $FeOH^+$, $CrOH^{2+}$, and H^+ occur simultaneously, but with different rates. The chemical equilibrium constants of the reactions producing metal-chloride ions (K_2 and K_3) are several orders of magnitude larger than those producing metal-hydroxide ions (K_1 and K_4); consequently, the concen-

trations of $FeOH^+$ and $CrOH^{2+}$ are less than the other ionic products listed above. Due to the relatively small amount of $FeOH^+$ compared to other species, we do not show its concentration profile in Figure 2.10. Notably, all ionic concentrations show large variations near the crevice mouth ($x_1 = 0.4375$ inch), and show little variation within the crevice solution. Thus, the ionic concentrations at the far-field boundary do not affect those within the crevice. This suggests that our second modeling assumption is valid and will not affect the accuracy of predicted concentrations inside the crevice.

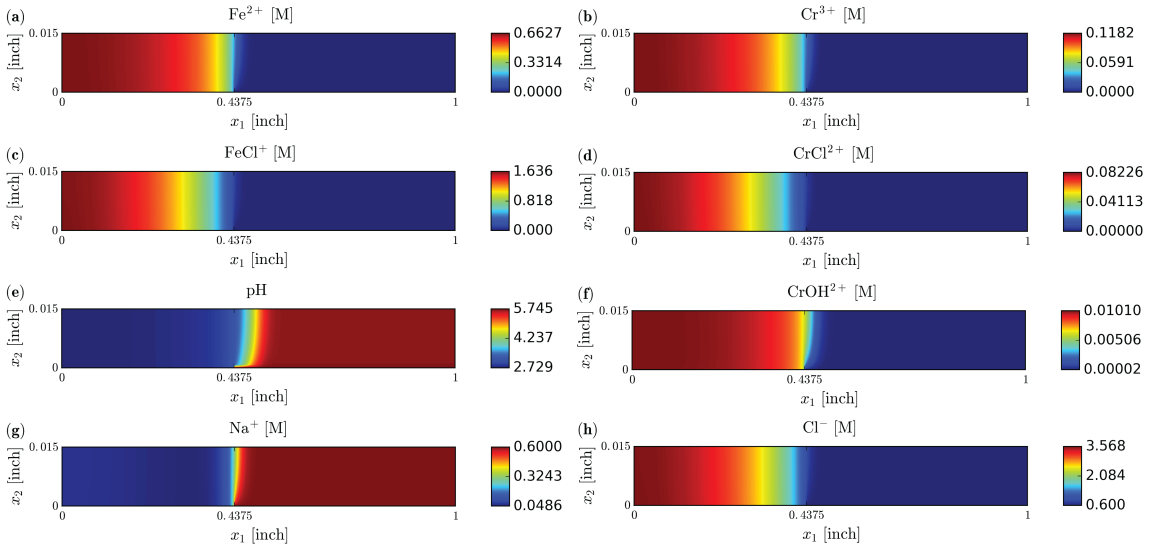

Figure 2.10: Steady-state numerical results obtained from the SNIA for 2D crevice corrosion of Fe-15Cr binary alloy: Concentrations of (a) Fe^{2+}, (b) Cr^{3+}, (c) $FeCl^+$, and (d) $CrCl^{2+}$; (e) the pH $= -log_{10}[H^+]$; Concentrations of (f) $CrOH^{2+}$, (g) Na^+, and (h) Cl^-.

We next perform a parametric study by varying the chromium weight fraction f_7 to examine following experimental observations:

1. In the experiment with $f_7 = 25\%$, steady state is reached after approximately 5 hours;

2. The time taken to attain the steady state increases with the weight fraction of chromium, so the experiment with $f_7 = 25\%$ takes longer time than other experiments;

3. The steady-state pH at the crevice mouth decreases as the chromium content increases.

The results from this study are shown in Figure 2.11. We compare the pH at crevice mouth predicted by SNIA with the experimental data reported by Bogar and Fujii and the simulation results of Sharland's [132], as shown in Figure 2.11(a). In this example, Sharland applied the two-step method using CHEQMATE and PHREEQE different from the one-step reformulation-based approach described in Appendix B. Interestingly, the SNIA gives better predictions of the pH for Fe-Cr binary alloys with chromium content less than 20% and shows a consistent trend with experimental results, that is, the predicted pH at crevice mouth decreases with an increase in the weight fraction of chromium. As remarked by Sharland [132], the discrepancy between the predicted pH and the experimental data is attributed to the lower value of assumed current densities for $f_7 \geq 20\%$, as tabulated in Table 2.3. Because of the underestimation of current densities, the amount of metal ions dissolving into the electrolyte from the solid phase is lesser; consequently, the amount of hydrogen ion getting produced through chemical reactions (2.32) and (2.40) is also lesser. Figure 2.11(b) shows the evolution of the hydrogen ion concentration at the crevice mouth for $f_7 = 1\%$, 10%, and 15%. While the hydrogen ion concentration for $f_7 = 1\%$ seems to have reached the steady state after 5 hours, the other two cases still seem to be asymptotically approaching the steady state. This result is consistent with the experimental observation that time taken to attain the steady state increases with the weight fraction of chromium.

To further demonstrate the consistency between predicted results obtained from the SNIA and the experimental data, the total amount of iron and chromium ions in the crevice solution is evaluated. In Bogar and Fujii's experiment, they inserted a microcapillary of uniform bore into the crevice and withdrew 1 μL samples of crevice solution in the vicinity of the crevice opening. They obtained the local concentrations of Fe^{2+} and Cr^{3+} by analyzing these samples, and then calculated the total amount of these ions by assuming a uniform concentration throughout the crevice. However, the specific location where they withdrew the crevice solution was not clearly reported. Therefore, we compute the total amount of Fe^{2+} and Cr^{3+} from the SNIA using the mean concentrations of these ions throughout the

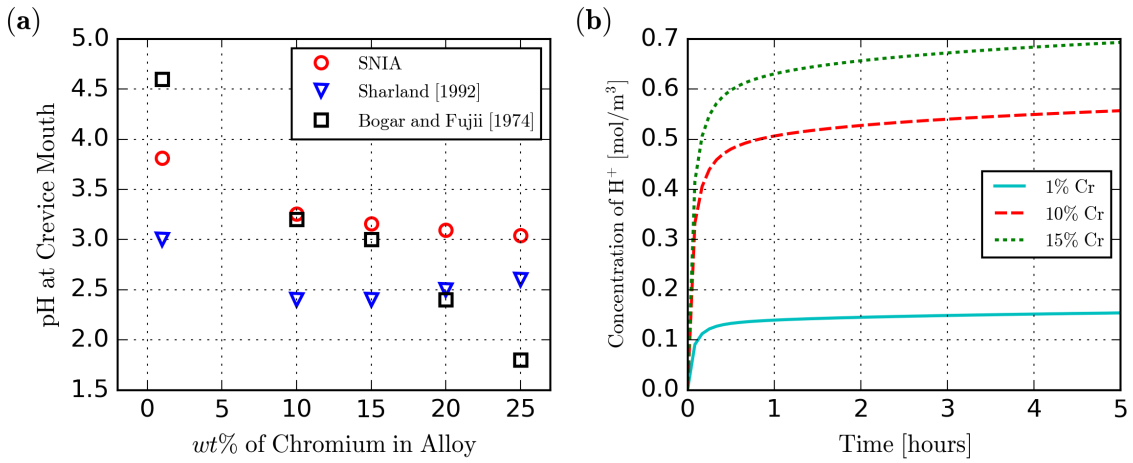

Figure 2.11: (a) Parameter sensitivity study examining the relationship between the weight fraction of chromium in Fe-Cr alloy and pH at crevice mouth. Numerical results of Sharland's and experimental data of Bogar and Fujii's are taken from Table 10 in [132]; (b) Time dependence of hydrogen ion concentration at crevice mouth for Fe-1Cr, Fe-10Cr and Fe-15Cr binary alloys in 3.5% NaCl solution.

crevice. To understand the variability in the weight prediction of metal ions, we account for the uncertainty in the location where the sample is withdrawn. We estimated the total amount of Fe^{2+} and Cr^{3+} using the predicted concentrations at the crevice tip ($x_1 = 0$) and mouth ($x_1 = 0.4375$ inch), based on the uniform concentration assumption. In Figure 2.12, we plotted the estimated total amounts of metal ions from the crevice tip and mouth as the upper and lower bounds of the error bar, respectively. From Figure 2.12, we can see that our predictions of Fe^{2+} and Cr^{3+} are in better agreement with the experimentally measured value compared to Sharland's results. We think that this improvement is due to the better representation of the experimental setup, particularly, the imposition of the far-field boundary conditions. However, because of the lower estimation of the electrode current density, the predicted amount of Cr^{3+} is significantly less than the measured value for alloys with the weight fraction of chromium greater than 20%. We believe the accuracy of predicted ionic concentrations can be further improved if more detailed experimental data is available.

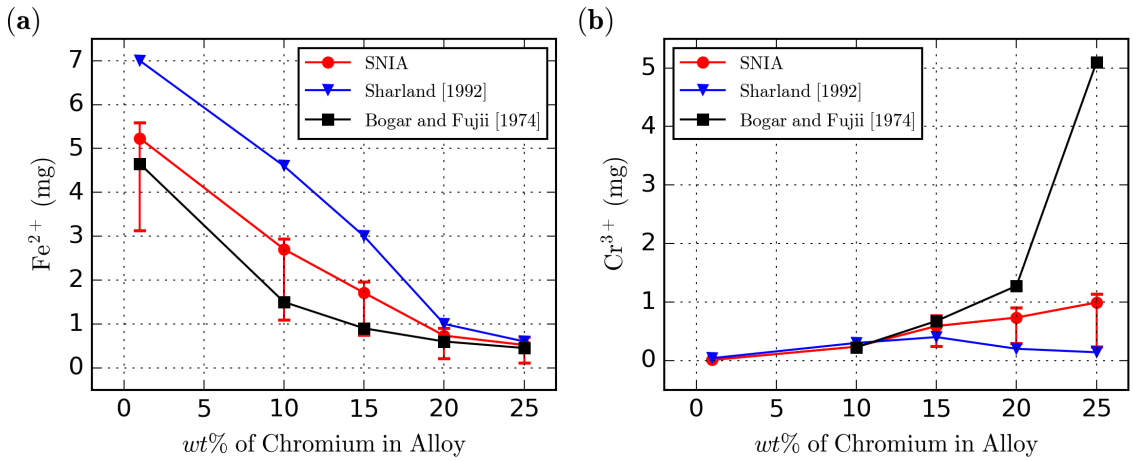

Figure 2.12: Parameter sensitivity study examining the relationship between weight fraction of chromium in Fe-Cr alloy and: (a) amount of Fe^{2+} in the crevice solution; (b) amount of Cr^{3+} in the crevice solution. Numerical results of Sharland's and experimental data of Bogar and Fujii's are taken from Table 10 in [132].

2.5 Conclusions

The corrosive dissolution problem is quite challenging because it involves multiple ionic species, multi-timescale processes due to electro-diffusive-reactive transport and multiple physical/chemical phenomena governed by highly non-linear partial differential equations. In this chapter, we propose a sequential non-iterative approach (SNIA) to model the multi-ionic species reactive transport in the liquid (electrolyte) phase during localized corrosion. We use the concept of total solute concentration to de-couple the governing equations of electro-diffusive mass transport from homogeneous equilibrium chemical reactions, leading to a two-step staggered numerical solution strategy: first, we compute the uncorrected concentrations and potential from the nonlinear Nernst-Planck equations and local electroneutrality (LEN) condition along with initial and boundary conditions; second, we compute the corrected concentrations by solving the nonlinear chemical equilibrium equations. Herein, the nonlinear Nernst-Planck equations along with the LEN condition are linearized using the Newton-Raphson method, discretized in space using standard quadratic finite elements (six-noded triangles), discretized in time using the backward Euler scheme, and solved within the open-source software FEniCS. The nonlinear chemical equilibrium equations are also solved using the Newton's method but with an the under-relaxation factor to ensure non-negativity of corrected concentrations. We then compared and validated the accuracy and robustness of the SNIA by conducting two sets of simulations studies focusing on corrosion of carbon steel and Fe-Cr binary alloys within 1D cavity and 2D crevice.

An important contribution of this study to the literature on finite element analysis of electrochemical systems is the evaluation of the numerical accuracy. Particularly, we conducted studies evaluating the error (relative to Sharland's approach) in resolving ionic concentrations and corrosion current densities as a function of the time increment size. Figure 2.4 indicates that an appropriate size of time increment chosen based on the characteristic diffusion time scale of the corrosion system will ensure sufficient numerical accuracy of

the SNIA. We also demonstrate the robustness of the SNIA by varying the values of electrochemical and crevice geometry parameters. For the larger metal potential $\phi_{\mathrm{M}} = -0.1$ V (see Figure 2.8), the one-step coupled formulation (see Appendix B) encountered difficulty with numerical convergence; whereas, there were no convergence issues with the SNIA. This is because in the SNIA we solve the nonlinear algebraic (chemical reaction) equations separately from the partial differential (mass transport) equations. We also illustrate the flexibility of the SNIA in handling different electrochemical systems corresponding to carbon steel and Fe-Cr binary alloys without requiring any reorganization of equations or readjustment of kinetic reaction rate constants. The parametric study examining the variation of steady-state pH at the crevice mouth (see Figure 2.11) and total amount of ferrous and chromium ions in relation to the chromium weight fraction (see Figure 2.12) during crevice corrosion of Fe-Cr binary alloys showed good agreement between results obtained from SNIA and the experimental data reported by Bogar and Fujii [22]. While the advantages of the SNIA are its robustness and flexibility, the disadvantage is reduced computational efficiency due to time increment size restrictions to ensure sufficient numerical accuracy.

Because the SNIA was rarely applied to electrochemical corrosion, we restricted the scope of this chapter to demonstrating that the SNIA performs well in comparison with previous simulation results [132, 133] and experimental data [22]. The SNIA is relatively straightforward and robust, so it holds great promise for studying and understanding the complex electrochemistry problems, involving the electro-diffusive-reactive transport of multiple chemical species in the solution.

Chapter 3

NUMERICAL INVESTIGATION OF CRITICAL ELECTROCHEMICAL FACTORS FOR PITTING CORROSION USING THE SEQUENTIAL NON-ITERATIVE APPROACH

3.1 Introduction

Austenitic stainless steels are widely used by the U.S. military in mobile and fixed equipment and structures due to their outstanding resistance to uniform corrosion [53, 94]. However, the main use of these equipment and structures is in harsh marine environments, which can be acidic and usually contain high concentrations of chloride [129, 136, 168]. Due to prolonged exposure in such an aggressive atmospheric environment, these steels are susceptible to localized corrosion, which can lead to high maintenance costs as well as potential threats to structural health and safety [28, 35, 51]. To mitigate these risks, it is essential to fundamentally understand and predict the propagation of localized corrosion. Existing studies have shown that localized corrosion is a complex electrochemical dissolution process occurring at the interface between metal (solid) and electrolyte (liquid) [49, 55]. The stable propagation of localized corrosion is governed by the bulk environment, the composition of the alloy, and the aggressive chemistry within the localized corrosion site [75, 175]. To better understand the critical chemistry that enables or prevents the localized corrosion of 300 series stainless steels, herein we conduct numerical studies using a multi-species reactive transport model [40, 46, 108, 148] to investigate key electrochemical factors responsible for stable pitting and repassivation of 316L stainless steel wire immersed in sodium chloride solution.

Sustained pit dissolution, which is often termed as stable propagation of an active pit, involves aggressive chemistry: high concentrations of metal cations produced by the oxidation of the metal alloys, low (acidic) pH caused by the subsequent hydrolysis of those

cations, and high concentration of chloride migrating from the bulk solution [18, 92, 144]. The conditions that ensure the maintenance of such chemistry are typically analyzed using the one-dimensional (1-D) pit concept. Because the 1D pit has a simpler geometry than the natural pits occurring in service, it can be directly used to quantitatively study the correlation between the internal electrochemistry evolution and pit depth as well as other variables in experiments. Galvele first formulated the steady-state relationship between metal dissolution and mass transport inside the 1D pit [56]. In Galvele's study, it was theoretically demonstrated that the product of the current density and the pit depth needed to be greater than a critical value to maintain the necessary local aggressive chemistry for sustained/stable pit growth. This critical value has been referred to as the pit stability product (X_{ps}) in the literature [27, 114]. Additionally, other critical electrochemical factors can also be evaluated by constructing the 1D pit, as shown in several recent studies [74, 139, 166]. These critical electrochemical factors are associated with different stages of experiments: stable pit growth under a salt film, film-free metal dissolution, and the transition to repassivation.

The 1D pit experiments first apply a high electrical potential in order to initiate and grow pits, which leads to the precipitation of a salt film on the corroding surface [64, 151]. The formation of this salt film is dictated by solubility limits of metal chlorides. Compared to the pit depth, the thickness of the salt film is negligible so its structure will not affect ionic transport within the pit [81]. The salt film only serves as source/sink for metal and chloride ions considering that perturbations in current may occur during experiments [139]. Under such circumstance, metal dissolution is diffusion-limited so that the corroding system is in a quasi-steady state. The pit stability product under a salt film can then be extracted from measuring the diffusion-limited current density at different pit depths [57, 81, 98, 104]. To estimate the conditions that govern the transition of the pit from stability to repassivation, rapid polarization scans can be employed which decrease the applied potential below the point where the salt film disappears. In this stage, metal dissolution proceeds in a salt

film-free environment. As the applied potential is gradually decreased, the corresponding decrease in metal dissolution rate and diminished cation hydrolysis [92] would lead to an increase of the pH near the corroding surface and eventually cause the pit to passivate. The repassivation potential is the potential corresponding to the conditions below which the pit will no longer propagate [12, 67, 149]. It is important to note here that these experiments utilize applied polarization to develop and evaluate the critical electrochemical conditions associated with stable pitting and the transition to repassivation, although corresponding conditions are independent of how they are attained. In other words, pitting in practice will also be governed by the same critical conditions, and the 1D pit experiments provide an effective testbed to attain and evaluate such conditions via a simplified geometry and applied polarization.

Complementary to experimental studies of pitting corrosion, mechanistic modeling studies are essential to better understand the chemistry evolution of both active and passive pits as experimental access to in-situ measurements of important parameters is highly limited due to the size scale. The simplest of mechanistic models consider mass transport of solute species (e.g., metal or hydrogen ions) in the solution environment based on the Fick's law of diffusion [52]. The 1D Fickian diffusion model has been widely used to simulate the evolution of the chemistry inside the 1D pit [7, 42, 72, 82, 137, 138, 140]. Srinivasan et al. used this model to evaluate the effect of the external hemispherical boundary layer on the cation flux inside the pit [140] and to demonstrate the dilution of cations near the corroding surface when repassivation happens [137, 138]. Jun et al. applied the similar model to analyze the effects of chloride concentration and temperature on 1D pit growth [72]. The main drawback of this 1D diffusion model is that it ignores the effect of electro-migration and viscosity on species transport. Therefore, Jun et al. further extended their model to calculate the flux inside the pit by incorporating the effect of electro-migration and viscosity into the species diffusion coefficient based on the Stokes-Einstein equation [73]. However, this improvement is based only on parametric calibration, so it does not

fully account for the governing physics of ion transport. As such, Jun et al. model is applicable only for estimating the flux, but not for predicting the species concentrations and the electrical potential.

To better understand and predict the evolution of species concentration and electrical potential, it is necessary to use a comprehensive mechanistic model of pitting corrosion that considers electro-diffusive mass transport of multiple species and homogenous chemical reactions in solution. However, there is a vast separation of times scales between mass transport and chemical reaction processes. For this reason, the evolution of chemistry dominated by chemical reactions in the electrolyte are often solved using special commercial software and databases, separate from those used for solving the diffusion models using decoupled approaches. In this study, we adopt a multi-species reactive transport model based on the sequential non-iterative approach (SNIA) developed by Sun and Duddu [148]. Compared to other numerical approaches proposed for solving electro-diffusive-reactive transport equations [89, 131, 163], the SNIA is able to establish the pit chemistry with multiple species and reactions in a more robust and flexible manner. The robustness of the SNIA arises from the decoupling of the time-dependent partial differential equations of the slower mass transport process from the nonlinear algebraic equations of the faster equilibrium chemical reactions. The flexibility of SNIA stems from the utilization of the total solute concentration concept to establish the corrected concentrations, which eliminates the necessity to reorganize the governing equations. However, the drawback of the SNIA is that it can be computationally more expensive compared to the coupled approaches, due to the restrictions on time increment size to ensure numerical accuracy.

The remainder of this chapter is organized as follows: in Section 3.2, we briefly describe the setup of artificial pit experiments and two commonly used mass transport models for simulating multi-species reactive transport during corrosive dissolution; in Section 3.3, we establish the decoupled governing equations of the reactive-transport model for corrosion and summarize the strategy for solving those equations; in Section 3.4, we detail the cali-

bration of parameters based on experimental data; in Section 3.5, we present the predicted critical electrochemical factors for both stable dissolution under a salt film and transitioning from film-free stable pitting to repassivation, and discuss the potential mechanisms dominating the evolution of the local chemistry for pit stability and repassivation; in Section 3.6, we conclude with a brief summary and closing remarks.

3.2 Background

In this section, we first introduce the setup of artificial pit experiments, from which we extract data to calibrate parameters of electrode kinetics. We next briefly describe two commonly used mass transport models and their limitations for simulating multi-species reactive transport during corrosive dissolution.

3.2.1 Artificial pit experiments

This study utilized data from one-dimensional artificial pit experiments reported by Srinivasan et al. [138, 139]. Lead-in-pencil electrode can better describe the geometry of these experiments as shown in Figure 3.1(a). The pit was constructed using 316L stainless steel wires with diameter $\varnothing = 50.8$ μm embedded in epoxy. The wires were composed of 67.98 wt% Fe, 17.07 wt% Cr, 10.66 wt% Ni, and 2.16 wt% Mo, with trace amounts of other elements that were ignored in this study. After surface polishing to a finish of 320 grit with SiC abrasive , the electrode was placed upright in the test container filled with 0.6 M NaCl solution. A saturated calomel electrode (SCE) and a platinum mesh electrode were employed as the reference and counter electrode, respectively. All tests were performed at an average ambient temperature of 22 °C using a Bio-Logic SP-200 (Bio-Logic SAS, Claix, France) potentiostat. The pit was initiated with a potential of $+750$ $\mathrm{mV_{SCE}}$ and then propagated to different depths by applying a lower potential of $+450$ $\mathrm{mV_{SCE}}$. After that, a rapid cathodic polarization scan at 5 mV/s to a final potential of -900 $\mathrm{mV_{SCE}}$ was conducted to extract the pit stability product, the transition and the repassivation potentials for a specific pit geometry. Parametric calibration based on the experimental data will be detailed in Section 3.4.

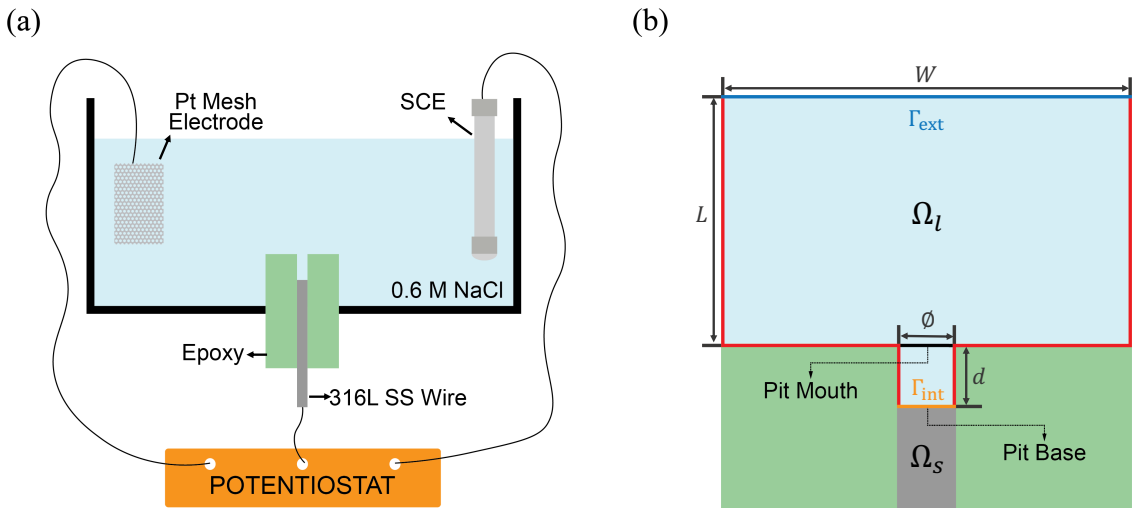

Figure 3.1: Schematic diagram of: (a) the experimental setup; (b) the two-dimensional domain for the artificial pit corrosion problem used in simulation studies. The corrosion interface Γ_{int} (orange) separates the solid metal Ω_s (gray) and liquid solution Ω_l (light blue) domains. Far-field (or bulk solution) concentrations and applied potential are prescribed at the external (dark blue) boundary Γ_{ext}. Zero flux condition is enforced on the boundaries marked by red color. The rest of the domain (green) is composed of epoxy and is excluded from the simulation domain.

3.2.2 Existing mathematical models

Based on the geometric setup of artificial pit experiments, we define a two-dimensional domain for our simulation studies that consists of two phases: the solid electrode domain Ω_s and the liquid electrolyte domain Ω_l, as shown in Figure 3.1(b). The reference and counter electrodes can be ignored here considering their spatial distances away from the pit mouth. The electrode and electrolyte domains are separated by a sharp corrosion interface Γ_{int}. In the electrolyte domain Ω_l, both mass transport and homogeneous chemical reactions can cause changes in species concentrations and distribution. According to the law of conservation of mass, the rate of change of concentration of the species i can be expressed as

$$\frac{\partial C_i}{\partial t} = -\nabla \cdot \boldsymbol{J}_i + R_i \ \text{ in } \ \Omega_l, \ i = \{1, 2, \cdots, n\}, \tag{3.1}$$

where C_i [mol/m^3] and $\boldsymbol{J}_i$ [mol/m^2/s] are the concentration and flux density of the i^{th} species at time t [s], respectively; ∇ denotes the spatial gradient vector; R_i [mol/m^3/s] is the rate of chemical reactions and n denotes the total number of species in Ω_l. In the stagnant electrolyte environment, the transport of species is driven by species concentration gradients and/or the electrical potential gradient [133]. Depending on whether the electromigration effect is taken into consideration or not, the flux $\boldsymbol{J}_i$ can be described by two different models: the Fickian (diffusion) model and the Nernst-Planck (electro-diffusion) model.

According to Fick's laws of diffusion [52], the magnitude of species flux density $\boldsymbol{J}_i$ is proportional to the concentration gradient, which can be written as

$$\boldsymbol{J}_i = -D_i \nabla C_i, \tag{3.2}$$

where D_i [m^2/s] is the Fickian diffusion coefficient of species i. However, charge balance is not satisfied for multi-ionic species in the Fickian model because the electrical potential

field due to ion migration is not properly described. A better way is to incorporate multi-species transport with charge balance using the Nernst-Planck model, which considers the transport of species due to both diffusion and electro-migration. By assuming the electrolyte to be in a stagnant condition in the artificial pit, advection can be ignored. The flux $\boldsymbol{J}_i$ of the i^{th} species can be written as

$$\boldsymbol{J}_i = -D_i \nabla C_i - \frac{z_i F}{R^* T} D_i C_i \nabla \phi, \tag{3.3}$$

where z_i [–] is the charge number of species i, F [C/mol] is the Faraday's constant, R^* [J/mol/K] is the universal gas constant, T [K] is the temperature, and ϕ [V] is the electrical potential of electrolyte. The potential field can be established by solving the Poisson's equation as given by

$$\nabla^2 \phi = -\frac{F}{\varepsilon} \sum_{i=1}^{n} z_i C_i \text{ in } \Omega_l, \tag{3.4}$$

where ε is the permittivity of the electrolyte. The permittivity of the electrolyte is relatively small compared to the value of Faraday's constant, resulting in the large value of the right-hand term F/ε in Equation (3.4). That means any deviation from electro-neutrality requires unrealistically large electrical restoring force. Such large electric force removes charge gradients on a much faster timescale than that of species diffusion [133]. Furthermore, visible deviation from electro-neutrality can only be observed in the double layer near the electrode interface with the order of 1 to 10 nm in thickness [87]. Therefore, the local electro-neutrality (LEN) condition is applied as an good approximation of the Poisson's equation, which can be expressed as

$$\sum_{i=1}^{n} z_i C_i = 0 \text{ in } \Omega_l. \tag{3.5}$$

Note that the electrolyte near the electrode will reach to saturation when a large enough electrical potential is applied during artificial pit experiments [138]. Because the Nernst-

Planck model is used to describe the mass transport of aqueous chemical species in dilute electrolytic solutions [76, 133], we need to extend Equation (3.3) by considering the effect of viscosity associated with temperature on the diffusivity of the species in the highly concentrated electrolytic environment.

3.3 Numerical Framework

In this section, we first detail the decoupled multi-species reactive transport equations corresponding to the pitting corrosion problem. To solve these equations in a robust and flexible manner, we next briefly discuss the solution strategy based on the sequential non-iterative approach.

3.3.1 Decoupled formulation

Using the sequential non-iterative approach (SNIA) [14, 148], we split Equation (3.1) into two separate equations describing mass transport and chemical reaction in strong ionic solutions, respectively. The rate of chemical reaction R_i will be first eliminated from the species transport Equation (3.1), which will yield physically incorrect ionic concentrations. The so-called "uncorrected" concentrations $\widetilde{C}_i$ can be computed as

$$\frac{\partial \widetilde{C}_i}{\partial t} = D_i \nabla^2 \widetilde{C}_i + \frac{z_i D_i F}{R^* T} \nabla \cdot \left(\widetilde{C}_i \nabla \phi \right) \quad \text{in } \Omega_l, \; i = \{1, 2, \cdots, n\}. \tag{3.6}$$

Because the neglected chemical reactions satisfy charge balance, the LEN condition in Equation (3.5) is still valid for the uncorrected concentrations and can be enforced to establish the electrical potential field. Thus, the uncorrected concentrations and electrical potential can be determined by solving Equation (3.6) along with LEN condition in Equation (3.5). The boundary conditions corresponding to Equations (3.5) and (3.6) are given by

$$\begin{aligned} \widetilde{C}_i(\mathbf{x}, t) \;=\; C_i^{\infty} \;\text{ and }\; \phi(\mathbf{x}, t) = -E_{\text{SCE}} \quad &\text{on } \Gamma_{\text{ext}}, \\ \boldsymbol{J}_i \cdot \mathbf{n} = \frac{\kappa_i i_{\text{a}}}{z_i F} \quad &\text{on } \Gamma_{\text{int}}, \end{aligned} \tag{3.7}$$

where C_i^{∞} is the far-field concentration of species i, E_{SCE} is the reference electrode potential, $\mathbf{n}$ denotes the unit normal to the interface Γ_{int} pointing outward from Ω_l, i_{a} [A/m^2] represents the anodic current density, and κ_i [–] is the coefficient of electrode kinetics. The

product of κ_i and i_a gives the current flux corresponding to species i due to electrode reactions. For metal cations dissolving into the electrolyte through anodic reactions, κ_i is taken as the molar fraction of the corresponding metal element in the alloy. For the hydroxide ion generated by the local cathodic reaction, κ_i is taken equal to an experiment-determined ratio of the local cathodic current density to the anodic current density [137].

Typically, corrosion interface evolution is much slower than the mass transport of ions in solution; whereas, chemical reactions are extremely fast so that equilibrium is attained almost instantaneously. Because there exists several orders of magnitude difference in timescales of corrosive dissolution, homogeneous chemical reactions, and electro-diffusive mass transport [124], it is physically consistent to use the SNIA. Neglecting the motion of corrosive interface Γ_{int}, the concentration of species involved in chemical reactions must satisfy the chemical equilibrium condition as given by

$$K_r \prod_p C_p^{\nu_{rp}} = \prod_q C_q^{\nu_{rq}}. \tag{3.8}$$

where K_r is the equilibrium constant of the r^{th} reaction, C_p and C_q are concentrations of the reactant and product species, respectively, and ν_{rp} denotes the stoichiometric coefficient of species p in the r^{th} reaction. The corrected concentrations C_i that satisfy the chemical equilibrium condition described above are related to the uncorrected concentrations $\widetilde{C}_i$ as [148]

$$C_i = \widetilde{C}_i + \sum_{r=1}^{n_r} \omega_{ri} \nu_{ri} \widehat{C}_r, \tag{3.9}$$

where n_r is the total number of chemical reactions occurring in the electrolyte, the product of ν_{ri} and $\widehat{C}_r$ gives the absolute value of concentration change of species i due to the r^{th} chemical reaction, and ω_{ri} represents whether species i is a reactant, product or not involved in the forward direction of the r^{th} reaction. If the species i is not involved in the r^{th} reaction, $\omega_{ri} = 0$; however, if involved in the forward reaction as the product then $\omega_{ri} = 1$, or as the reactant then $\omega_{ri} = -1$. Substituting Equation (3.9) into Equation (3.8), we can obtain n_r

number of nonlinear algebraic (chemical reaction) equations to solve for unknowns $\widehat{C}_r$ as follows:

$$K_r \prod_p \left(\widetilde{C}_p + \sum_{l=1}^{n_r} \omega_{lp} \nu_{lp} \widehat{C}_l \right)^{\nu_{rp}} - \prod_q \left(\widetilde{C}_q + \sum_{l=1}^{n_r} \omega_{lq} \nu_{lq} \widehat{C}_l \right)^{\nu_{rq}} = 0, \;\; r = \{1, 2, \cdots, n_r\}. \tag{3.10}$$

To ensure the non-negativity of species concentrations, the nonlinear chemical reactions equations (3.10) are solved using the Newton-Raphson method together with the under-relaxation technique. This decoupled formulation can lead to better-conditioned discretized system of equations, which is a significant advantage in the treatment of reduction-oxidation (redox) problems. However, the disadvantage is that decoupling of the species transport and chemical reaction will introduce numerical error. For numerical accuracy, we found it necessary to restrict the size of the time increment to 1% of the characteristic diffusion time scale of the domain [148].

3.3.2 Solution strategy

Based on the SNIA [148], we employ a two-step staggered numerical solution strategy at any given time increment as follows:

1. Compute the uncorrected concentrations $\widetilde{C}_i$ and electrical potential ϕ from the Nernst-Planck equations (3.6) and the LEN condition (3.5) along with boundary conditions (3.7);

2. Compute the corrected concentrations C_i of each species by solving the chemical equilibrium equations (3.10) using the modified Newton-Raphson method.

The detailed version of the above solution strategy in the format of a pseudocode has been introduced in Algorithm 1.

3.4 Parameterization and Calibration

In this section, we first clarify the two major stages of the 1D pit experiment considered in this numerical study: stable dissolution under a salt film and film-free dissolution that eventually transitions to repassivation. We then detail the calibration process for several key parameters including the elapsed time of each stage, the kinetics of electrode and chemical reactions, and the diffusivity and viscosity of each species.

3.4.1 Stages of the 1D pit experiment

We consider two main stages of the artificial pit experiments as the simulation targets of the numerical investigation: Stage I – stable dissolution under a salt film, and Stage II – film-free dissolution and transition to repassivation. In Stage I, the application of high electrical potential leads to metal dissolution and hydrolysis, which results in a local aggressive chemistry inside the pit. Due to the continuous high-rate metal dissolution and limited diffusion, a salt film precipitates on the corroding surface within the saturated metal chloride solution. The presence of the salt film results in diffusion-limited dissolution of the 316L cation species and fixes its concentration at the bottom of the pit. Note that the concentration here refers to that of the saturated solution adjacent to the salt film, not of the salt film itself. In this study, we do not consider any blocking of the electrode area, nor do we consider the solid-liquid interface motion caused by the formation of salt film . We assume the '316L cation' species consists of Fe^{2+}, Cr^{3+}, Ni^{2+}, and Mo^{3+} in the same proportion as the respective metal atoms in the alloy composition [137, 138, 140]. For brevity, the '316L cation' is referred to as "Me" in Section 3.5. The pit depth is considered as the diffusion distance when the current density is diffusion-limited. In experiments, Faraday's Law is used to calculate the pit depth because it can describe the relationship between pit depth and charge density [139]. The charge density is obtained from time-integration of the average current density (i.e., the measured current divided by the corroding surface

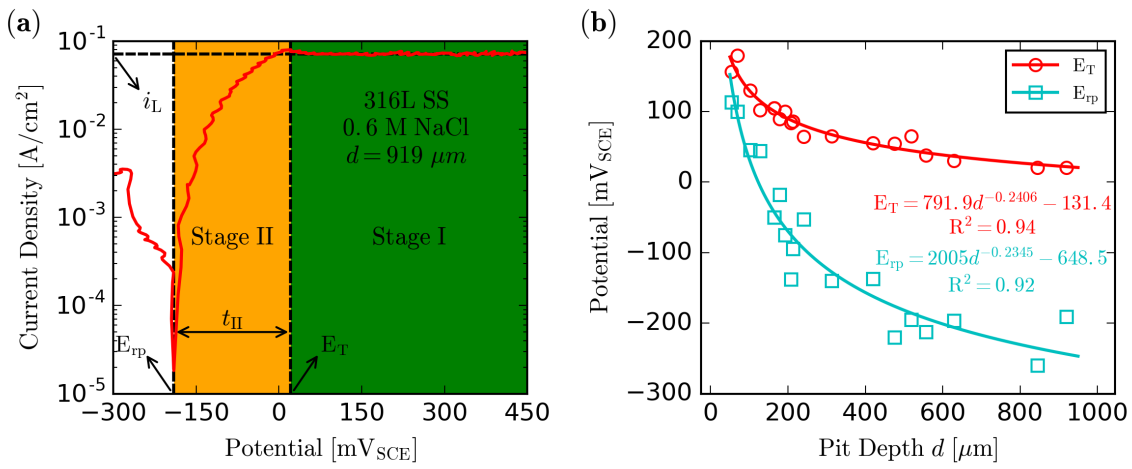

Figure 3.2: Extraction of kinetic parameters from experiments: (a) Polarization kinetics data indicating measurements of the diffusion-limited dissolution current density i_L, the transition potential E_T, and the repassivation potential E_{rp}. t_{II} denotes the elapsed time of Stage II. Red line represents the polarization curve obtained from the experiment. Green and orange regions are the first (stable dissolution under a salt film) and second (film-free dissolution and transition to repassivation) stages of the study, respectively; (b) Estimation of the transition potential E_T and the repassivation potential E_{rp} with respect to the pit depth d by least squares curve fitting based on the power law: $E_T = 791.9d^{-0.2406} - 131.4$, $E_{rp} = 2005d^{-0.2345} - 648.5$. Note that these fitted curves are applicable for pits with diameter $\varnothing = 50\ \mu$m.

area). Once the pit is corroded to the expected depth, decreasing the applied potential leads to dissolution of the salt film and film-free dissolution ensues. As the applied potential is further reduced, the anodic dissolution rate and the associated current density across the electrode-electrolyte interface Γ_{int} also decrease in response. The consequent dilution of the aggressive chemistry at the pit base, due to lesser metal dissolution rate as well as diffusion of concentrated aggressive species out of the pit, ultimately leads to repassivation.

The transition from Stage I and Stage II can be identified using the experimental polarization kinetics data as plotted in Figure 3.2(a). As long as the current density passing Γ_{int} stays at the diffusion-limited current density i_L, the system is in Stage I and the pit is expected to grow stably under a salt film. In this stage, we aim to investigate the pit chemistry at the saturated state by neglecting the motion of the corroding interface. The elapsed time of Stage I in experiments, which is adequately long to grow the pit to the expected

depth, is not relevant for numerical modeling. Instead, we directly run the simulation with the expected pit depth till the saturated state is attained. Note that the saturated state is not the same as steady state, where concentrations and electrical potential inside the pit no longer evolve over time as well as space. In Stage I of the 1D pit experiment, only saturated state is ensured because it can be easily identified by a constant diffusion-limited current measured. When the rapid polarization scan starts, we consider the beginning of Stage II as the time when the applied electrical potential decreases to the transition potential E_{T}, and the current density becomes less than i_{L}. At the end of this stage, the repassivation of the pit is estimated to occur when the current density is reduced to i_{rp} =30 μA/cm^2. The applied potential recorded instantly when the current density reaches i_{rp} is referred to as the repassivation potential E_{rp}. Because the polarization scan rate $\dot{E}_{\mathrm{app}}$ [V/s] is a constant, the elapsed time of the second stage t_{II} can be estimated by

$$t_{\mathrm{II}} = \frac{E_{\mathrm{T}} - E_{\mathrm{rp}}}{\dot{E}_{\mathrm{app}}}. \tag{3.11}$$

To evaluate the elapsed time of the second stage for pits with intermediate depths that are not measured through experimental studies, we further perform least squares curve fitting based on the power law for both the transition and repassivation potentials with respect to the pit depth (d), as shown in Figure 3.2(b). Note that the fitted curves are directly applicable only for pits with a constant diameter $\varnothing = 50$ μm.

3.4.2 Electrode reactions and kinetics

There are three types of electrode reactions occurring during the experiment: anodic metal dissolution, internal and external cathodic reactions [137]. We use the terms internal and external cathodic reactions to note the spatial difference as to where these cathodic reactions occur during experiments. Anodic dissolution and the internal cathodic reaction occur on the corroding surface of the 316L stainless steel wire, which is directly exposed

to sodium chloride solution. Anodic dissolution includes the oxidation of iron, chromium, nickel, and molybdenum:

$$\begin{aligned} \mathrm{Fe} &\rightarrow \mathrm{Fe}^{2+} + 2\,\mathrm{e}^{-}, \\ \mathrm{Cr} &\rightarrow \mathrm{Cr}^{3+} + 3\,\mathrm{e}^{-}, \\ \mathrm{Ni} &\rightarrow \mathrm{Ni}^{2+} + 2\,\mathrm{e}^{-}, \\ \mathrm{Mo} &\rightarrow \mathrm{Mo}^{3+} + 3\,\mathrm{e}^{-}. \end{aligned}$$

Because the conditions inside the pit are oxygen-poor, the local (internal) cathodic reaction is considered to be the hydrogen evolution reaction (HER) which can proceed as the reduction of water or protons listed below

$$2\,\mathrm{H_2O} + 2\,\mathrm{e}^{-} \rightarrow \mathrm{H_2} + 2\,\mathrm{OH}^{-}.$$

In the experiments considered, significant proportion of the cathodic reaction typically occurs on the counter electrode. Based on the fact that the counter electrode is spatially distant from the pit, the external cathodic reaction is assumed not to affect the local chemistry inside the pit and is therefore ignored in this study.

To specify the electrode flux boundary condition defined in Equation (3.7), we need to calibrate the anodic current density i_{a} based on experimental results. In the artificial pit experiments, the net current density i_{net} can be directly monitored using the potentiostat. Theoretically, the net current density is a difference between the anodic current density i_{a} and the local cathodic current density $i_{\mathrm{c,local}}$, which can be written as

$$i_{\mathrm{net}} = i_{\mathrm{a}} - i_{\mathrm{c,local}}. \tag{3.12}$$

Owing to the large potential difference applied during Stage I, the local cathodic reaction (HER) is negligible [137]. Therefore, the anodic current density is approximately equal to

the measured net (diffusion-limited) current density ($i_a = i_{net} = i_L$). However, once Stage II begins, the local cathodic reaction rate is considered to increase, coincident with the decrease of the anodic dissolution rate. Srinivasan and Kelly [137] previously estimated the ratio of the local cathodic current density to the anodic current density via Mixed Potential Theory analysis to be about 0.3% when the pH of the pit is sufficiently high to initiate the nucleation of passive oxides. Based on this estimate, the anodic current density at repassivation can then be calculated as

$$i_a = \frac{i_{net}}{1-0.003} = \frac{i_{rp}}{1-0.003}. \tag{3.13}$$

Regardless of the pit depth, we set the threshold of net current density to be a constant value of 30 μA/cm^2 in order to determine when repassivation occurs in artificial pit experiments [137]. In contrast, the diffusion-limited current density does vary for pits with different depths. Experiments demonstrated that the product of the diffusion-limited current density i_L and the pit depth d is constant as long as the temperature and the bulk concentration of sodium chloride do not change [139]. This allows us to define the pit stability product $X_{ps} = i_L \cdot d$, which can be obtained from the linear regression analysis of the experimental data. Appendix C lists the pit stability product values for stainless steel in NaCl solution at different temperatures and bulk concentrations. We use these values to calculate the diffusion-limited current density i_L, which defines the flux boundary conditions in our simulation studies of Stage I.

3.4.3 Diffusivity and viscosity

The metal chloride solution near the corroding surface will reach saturation when a large enough electrical potential is applied. As demonstrated by Jun et al. [73], the effect of electrolyte viscosity on mass transport in such a concentrated electrolyte environment cannot be ignored. The effect of viscosity η and temperature T on the diffusion coefficient

can be described using the Stokes-Einstein relation as

$$D = \frac{kT}{6\pi\eta r}, \tag{3.14}$$

where k [J/mol/K] is the Boltzmann constant and r [m] is the radius of the species. For the sake of simplicity, we assume that the the effect of temperature on the radius of the species can be neglected. Thus, the diffusion coefficient can be approximately calculated using its reference value D_{ref} as

$$D = \frac{TD_{\text{ref}}}{\eta T_{\text{ref}}}, \tag{3.15}$$

where the reference temperature T_{ref} is taken as the room temperature 298.15 K. The reference values of diffusion coefficients for all species considered in this study are listed in Appendix D. The viscosity of the electrolyte can be analytically represented based on the extended Jones–Dole equation [5], which can be written as

$$\eta = 1 + a_0 {C_l}^{\frac{1}{2}} + a_1 C_l + a_2 {C_l}^2 + a_3 {C_l}^3, \tag{3.16}$$

where C_l is the concentration of the electrolyte, and coefficients a_i can be calculated from its temperature-pressure dependence

$$a_i = \sum_{m=0}^{1} \sum_{n=0}^{4} \zeta_{mn} p^m \tau^n, \;\; i = \{0,1,2,3\}, \tag{3.17}$$

where p is the pressure, $\tau = T_0/T = 400\ \text{K}/T$ is the relative temperature, and ζ_{mn} are the coefficients calibrated from a series of experiments [5], which are listed in Appendix E. The integral indices m and n are only used for calibration without any physical interpretation. As noted by Aleksandrov et al. [5], Equation (3.16) is valid for describing the viscosity of aqueous solutions of sodium chloride in the concentration ranging from 0 to 6 M at temperatures from 0 to 325 °C. Based on the assumption of the LEN condition (3.5), we

herein use the concentration of Cl^- as the estimate for the electrolyte concentration C_l to calculate the viscosity of the solution.

3.4.4 Chemical reactions and kinetics

To capture the evolution of local chemistry inside the pit, we consider three types of homogeneous chemical reactions taking place in the electrolyte phase Ω_l including water dissociation, hydrolysis, and chloride complexation of metal ions, as follows

$$\begin{aligned} H^+ + OH^- &\rightleftharpoons H_2O, \\ M^{n+} + aH_2O &\rightleftharpoons MOH_a^{(n-a)+} + aH^+, \\ M^{n+} + aCl^- &\rightleftharpoons MCl_a^{(n-a)+}. \end{aligned}$$

where M refers to the constituent metallic elements that dissolve into electrolyte as cations through the oxidation reaction. For ferrous and nickel ions, $n = 2$ and $a = 1$ or 2, and for chromium and molybdenum ions, $n = 3$ and $a = 1$, 2 or 3. The calculation of equilibrium constants K_r for all three types of reactions is summarized in Appendix F.

3.5 Results and Discussion

In this section, we consider a 2D model of pitting corrosion as depicted in Figure 3.1(b). We assume a constant pit diameter $\varnothing = 50$ μm and different pit depths $d = \{50, 100, 150, 200, 250, 350, 500, 750, 1000\}$ μm. Because the movement of the corroding surface is neglected, the geometry of the pit does not change while dissolution is taking place. Following the example in [140], we take the dimension of the rectangular bulk electrolyte region above the pit to be $W \times L = 20 \times 10$ cm^2. In our previous work [148], we found that the size of time increment Δt should be less than 1% of the characteristic diffusion time scale $t_d = d^2/4D$ to ensure sufficient accuracy of the sequential non-iterative approach. We take the diffusion coefficient of metal ions (0.824×10^{-9} m^2/s) and the minimum pit depth (50 μm) to estimate the characteristic diffusion time scale. The size of time increment can then be calculated as $\Delta t = 1\% \times (50 \times 10^{-6})^2/(4 \times 0.8 \times 10^{-9}) \approx 0.01$ second. The governing equations of the model are solved using the standard finite element method in the open-source software FEniCS [9]. In accordance with the artificial pit experiments, the remainder of this section is organized by two experimental stages: stable pitting and repassivation.

3.5.1 Stage I: Stable dissolution under a salt film

At the first stage, we conduct a series of numerical studies by varying the pit depth, the temperature and the bulk concentration of the electrolyte. The ranges of these geometric and environmental parameters will be specified in the corresponding subsection. The initial conditions of concentrations and the electrical potential fields can be expressed as

$$\widetilde{C}_i(\mathbf{x},0) \;=\; C_i^{\infty} \;\text{ and }\; \phi(\mathbf{x},0) = 0 \quad \text{in } \Omega_l. \tag{3.18}$$

We define the metal cation "Me" as all species inside the pit that contain the primary alloying elements of 316L stainless steel (i.e., Fe, Cr, Ni, Mo). From in situ X-ray studies

on solutions of 18-8 stainless steel in chloride media conducted by Isaacs et al. [65], the saturated concentration of the metal cation C_{Me} near the pit base is reported as $C_{\mathrm{sat}} = 5.02$ M. Therefore, simulations are run until C_{Me} at the pit base reaches saturation (i.e., 5.02 M). Our goal in this section is to calculate the chemical composition (including the pH) and distribution inside active pits in order to provide a starting point for the analysis of repassivation during Stage II.

3.5.1.1 Local chemistry

We first investigate the local chemistry inside the pit in the saturated state at different depths. The temperature T and the bulk concentration of the sodium chloride electrolyte C^{∞} are taken as 25 °C and 0.6 M, respectively. In Figure 3.3(a), we show the concentrations of metal cation at the pit mouth together with the pH at the pit base with respect to different pit depths. The concentration of metal cation at the pit mouth decreases from 1.4 M ($\sim 28\%C_{\mathrm{sat}}$) to 0.2 M ($\sim 4\%C_{\mathrm{sat}}$) as the pit depth is increased from 50 to 1000 μm. This trend was also captured by the numerical results obtained from the 1D Fick's diffusion model [140]. For shallow pits, the characteristic length of cation mass transport is longer than the pit depth. Therefore, there exists the external hemispherical boundary layer such that the concentration of the metal cation outside the pit does not immediately vanish at the pit mouth. According to Srinivasan et al. [140], the flux of metal cations J_{Me} inside the pit can be calculated as

$$J_{\mathrm{Me}} = \frac{D\Delta C_{\mathrm{Me}}}{d} = \frac{D(C_{\mathrm{Me}}^{\mathrm{base}} - C_{\mathrm{Me}}^{\mathrm{mouth}})}{d} = \frac{DC_{\mathrm{sat}}}{d}. \tag{3.19}$$

Note that this calculation of flux is only based on the 1D Fick's law of diffusion. To ensure accuracy of this flux calculation, Srinivasan et al. [140] suggest choosing pit depths that are 8 to 10 times the pit diameter so that C_{Me} at the pit mouth approaches zero. Our predicted results also lead to a similar conclusion: for pits with diameter $\varnothing = 50$ μm, C_{Me} at the pit mouth is negligible ($< 4\%C_{\mathrm{sat}}$) only when the pit depth reaches 500 μm

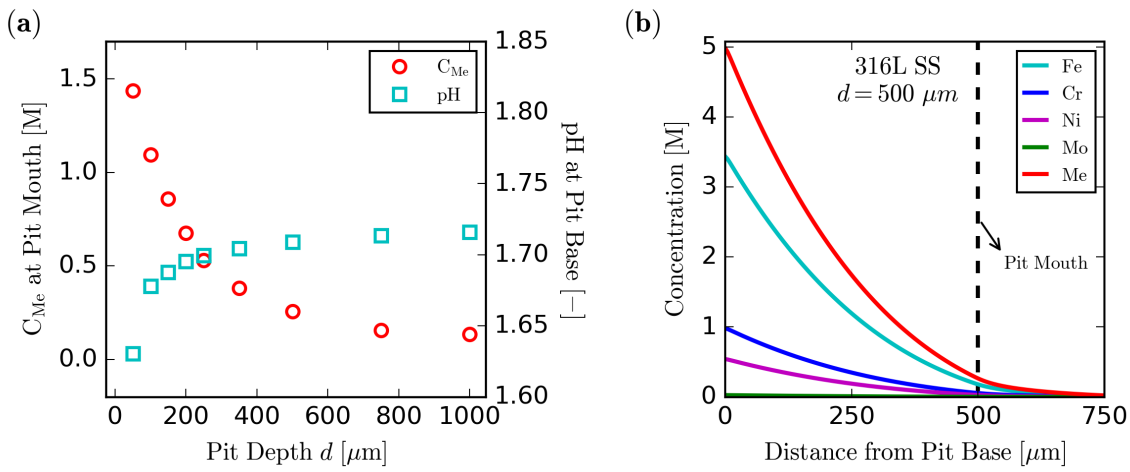

Figure 3.3: Numerical results of local chemistry inside the pit at the saturated state for pitting corrosion of 316L stainless steel wire within 0.6 M NaCl solution under room temperature $T = 25$ °C: (a) The concentration of metal cation at the pit mouth and the pH at the pit base with respect to different pit depths; (b) Concentration profiles of cations inside the pit with depth $d = 500$ μm.

($= 10\varnothing$). However, owing to the effect of electrolyte viscosity and electro-migration, the flux may not be calculated using Equation (3.19) in our simulation studies. As shown in Figure 3.3(b), the linear relationship between the concentration of cations and the spatial coordinate governed by Equation (3.2) is no longer valid. The flux varies non-linearly inside the pit, so it should be calculated using Equation (3.3).

From Figure 3.3(a), we also find that the pH at the pit base slightly increases with pit depth. Such a slight increase can be explained by considering the elapsed time of Stage I for different pit depths. The elapsed time t_{I} for shallow pits to reach to the saturated state is less than that of deep pits. Therefore, more H^+ generated from metal hydrolysis reactions diffuse out from the base of deep pits than that of shallow ones. The predicted values of the pH are all within the range of 1.63 to 1.71, which represent a locally acidic environment near the corroding surface. Srinivasan and Kelly [137] modeled the local chemistry near the corroding pit surface using the solution thermodynamics database of the OLI Analyzer Studio 9.2 (OLI Systems, Inc., Cedar Knolls, NJ) software. They found that formation of metal oxides, which isolates the pit base from acidic electrolyte, is dependent on the lo-

cal pH. According to their simulation results, the lowest pH that enabled the formation of metal oxide (CrO(OH)) is about 2.65. Based on this estimate, we conclude that our predicted chemistry near the pit base is aggressive enough that repassivation would not occur in this stage. Srinivasan and Kelly [137] also estimated the local pH near the pit base if only anodic dissolution was considered. This case corresponded to the absence of any local cathodic reaction, thus representing the conditions inside the pit during high-rate anodic dissolution, as expected when a salt film is present. The resulting pH predictions of as low as -0.25 may be due to the fact that they ignored the mass transport of individual cation species, and uniformly saturated the mixed solution of $FeCl_2$, $CrCl_3$, $NiCl_2$, and $MoCl_3$ in their calculations. The model introduced in this chapter is more comprehensive with respect to individual cation transport. Also, the predicted pH range at the corroding surface for high anodic dissolution (1.63 to 1.71) shows good agreement with the experimental data reported by Oldfield and Sutton [107], which measured the pH values of highly concentrated mixed solutions of $CrCl_3{\cdot}6H_2O$ and $FeCl_2{\cdot}4H_2O$ to be in the the range of 1.25 to 1.75. It is reasonable to compare their results with our prediction because of the chemical similarity between their prepared mixtures and our electrochemically produced solution.

3.5.1.2 Electrolytic resistance

To further quantitatively validate our model, we next focus on the prediction of the specific resistance of the electrolyte as the resistance of the pit is a measurable quantity. The electrolyte resistance in the pitting corrosion system consists of two parts: the resistance of the electrolyte in the pit, and that of the bulk solution [57]. Theoretically, the resistance of the pit R_{p} with a constant diameter is supposed to increase linearly with the increase of pit depth, whereas the bulk resistance is a constant and not dependent on the depth of the pit. Therefore, the pit electrolytic resistance is related to dimensions of the pit as given by

$$R_{\mathrm{p}} = \frac{4d\alpha_r}{\pi\varnothing^2}, \tag{3.20}$$

where α_r is the specific resistance of the electrolyte solution. The IR drop commonly refers to the decrease of electrical potential from the pit base to the mouth owing to the resistance of the electrolyte. According to Ohm's law, the IR drop within the pit can be expressed as

$$\Delta E_{\mathrm{IR}} = iR_{\mathrm{p}}, \tag{3.21}$$

where i is the electric current that passes through the entire pit system. In the first stage, the IR drop inside the pit can be calculated using the electrical potential at the pit base (ϕ_{b}) and mouth (ϕ_{m}) obtained from the SNIA. The corresponding current passing through the system is a constant, and is equal to the product of diffusion-limited current density (i_{L}) and the cross-sectional area of the 316L stainless steel wire. Therefore, the pit resistance can be estimated using the predicted electrical potential field obtained from our model as

$$R_{\mathrm{p}} = \frac{\Delta E_{\mathrm{IR}}}{i} = \frac{\phi_{\mathrm{b}} - \phi_{\mathrm{m}}}{i_{\mathrm{L}}\pi\left(\frac{\varnothing}{2}\right)^2}. \tag{3.22}$$

Substituting Equation (3.20) into Equation (3.22), we can then calculate the specific resistance α_r of the pit based on the theoretical understanding of the electrolyte resistance as

$$\alpha_r = \frac{\phi_{\mathrm{b}} - \phi_{\mathrm{m}}}{i_{\mathrm{L}} d}. \tag{3.23}$$

Experiments demonstrate that the specific resistance of solution decreases with the increase of solution concentration [119]. For the solution of chloride salt at room temperature $T = 25\ ^{\circ}\mathrm{C}$, the measured specific resistance decreases from 11.66 to 4.368 Ω·cm as the concentration of the solution increases from 1 to 5 M. In Figure 3.4, we show predicted specific resistances of the pit electrolyte with respect to different pit depths. With the increase of the pit depth, the predicted specific resistance of the pit electrolyte increases from 4.9 to 6.4 Ω·cm. However, the concentration of the electrolyte is not uniformly distributed inside the pit, as shown in Figure 3.3(b). To understand the relationship between the predicted α_r

and the electrolyte concentration, we need to consider the average electrolyte concentration inside the pit. The spatially averaged concentration of metal cation inside the pit obtained from our simulations is plotted in Figure 3.4, which decreases from 3.0 to 2.5 M as the pit depth increases from 50 to 1000 μm. We thus find that the specific resistance of the pit electrolyte and the concentration of the electrolyte are inversely proportional, which is consistent with the experimental observation [57]. Furthermore, the prediction obtained from our simulations shows a reasonable quantitative match with the experimental data. Specifically, the predicted α_r and the spatially averaged C_{Me} obtained from our simulations are within the range of the experimental results reported in [119]. From Figure 3.4, we also notice that there exists a plateau of α_r at approximately 6.4 Ω·cm when the pit depth is greater than 500 μm. This plateau implies that the specific solution resistance of the deep pit filled with specific type of electrolyte is a constant. As a consequence, the actual pit resistance increases linearly with its depth, which is attested to by calculations in the literature [83, 84]. The corollary result that the IR drop becomes constant for sufficiently deep pits is also consistent with prior work [81, 84].

3.5.1.3 Effect of temperature and bulk concentration

We next evaluate the effect of temperature and concentration of sodium chloride (bulk) solution on the local chemistry near the pit base and the specific resistance of the pit solution. We perform parametric studies on pitting corrosion of stainless steel by varying the temperature $T = \{25, 35, 45, 55\}$ °C and bulk concentrations $C_{\mathrm{bulk}} = \{0.6, 1.0, 3.0, 5.5\}$ M. To preclude any possible influence on those electrochemical factors caused by different pit depths, we here consider the pit with constant depth $d = 500$ μm. All simulations are run until a final (elapsed) time $t_{\mathrm{I}} = 400$ seconds to attain the saturated state of the solution inside the pit for $T = 25$ °C. As the ion motion increases with temperature, this final simulation time $t_{\mathrm{I}} = 400$ seconds ensures that saturation is reached at higher temperatures $T > 25$ °C.

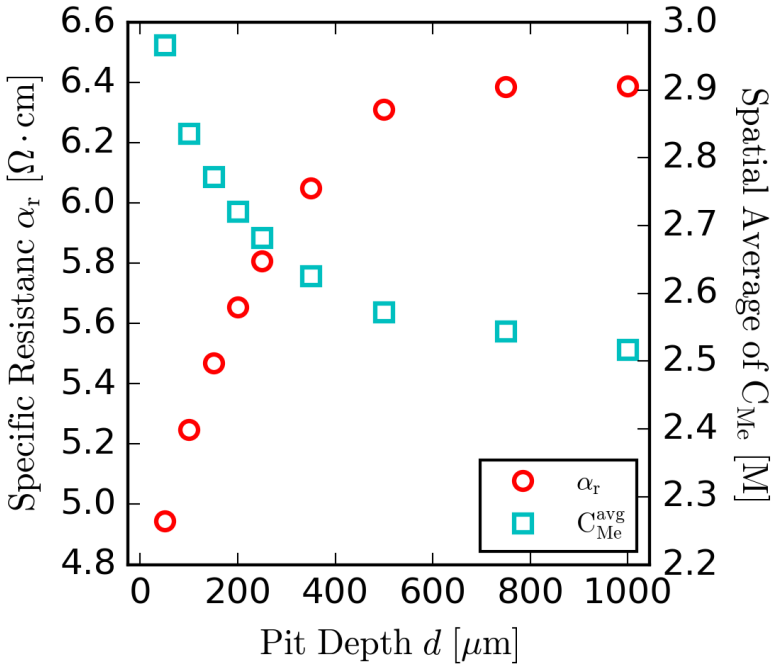

Figure 3.4: Numerical results of pit specific resistance and spatial average concentration of metal cation inside the pit with respect to different pit depths at the saturated state for pitting corrosion of 316L stainless steel wire within 0.6 M NaCl solution under room temperature $T = 25$ °C.

In Figure 3.5, we demonstrate the effect of temperature and bulk concentration on the local chemistry near the pit base. It is evident that the saturation concentration of metal cation increases with the increase of temperature, as shown in Figure 3.5(a). The same trend has also been reported based on experimental investigation of the ferrous chloride solution [36] and the corrosive electrolyte of 304L stainless steel [50, 75]. This result can be simply explained by the fact that the solubility of most salts increases with temperature [109]. From Figure 3.5(a), we also find that the saturation concentration of the metal cation decreases as the bulk concentration increases. Because of the common ion effect, the solubility of the metal cation decreases significantly with an increase in chloride concentration. This inverse relationship between the saturation concentration of metal cation and the bulk concentration of sodium chloride has also been noted by several experimental [51] and numerical studies [72, 73]. In Figure 3.5(b), we show the dependence of pH at the pit base on the temperature and bulk concentrations. Based on our previous analysis, the metal cation concentration at the pit base is higher in the system at higher temperature and lower bulk concentration. Under such circumstances, the hydrolysis of metal cations producing hydrogen ion is more intensive, which leads to the decrease of pH near the pit base [18, 92]. Therefore, the pH decreases with the increase of temperature and the decrease of the bulk concentration.

In Figure 3.6, we calculate the specific resistance of the pit solution at different temperature and bulk concentrations based on Equation (3.23). The pit specific resistance decreases with the increase of the temperature because of two important changes in the electrolyte: (1) the interionic attraction decreases with the temperature, so the ionic mobility increases [59]; (2) the degree of electrolyte dissociation increases with the temperature, so the number of ions available for conduction increases [15]. The pit specific resistance decreases with the increase in the concentration of the sodium chloride (bulk) solution, simply because the electrolyte with higher concentration has more charged particles capable of carrying an electrical current. However, the positive correlation between the electrolyte

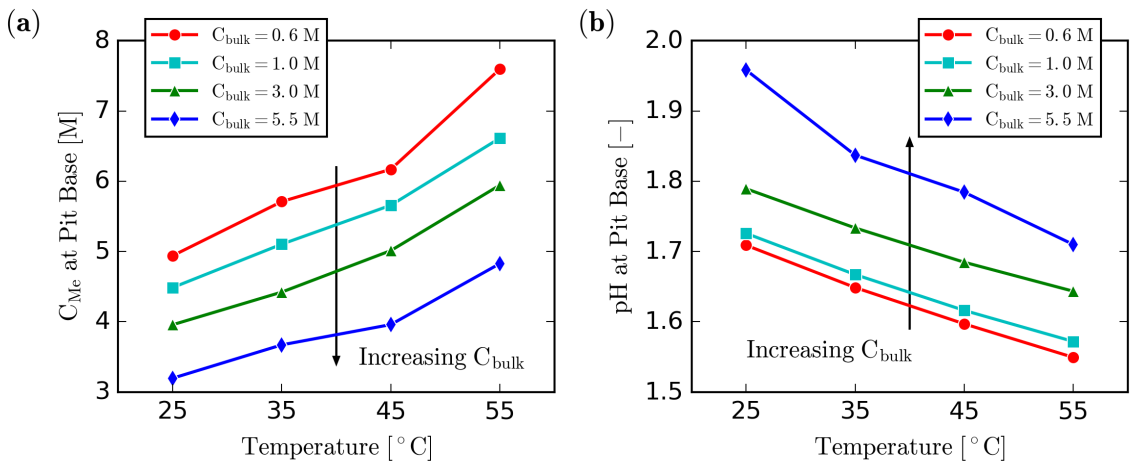

Figure 3.5: Parametric sensitivity of critical electrochemical factors with respect to temperature T and bulk concentrations C_{bulk}: (a) Concentration of metal cation C_{Me} at the pit base; (b) pH at the pit base.

concentration and conductivity may not always hold. As the electrolyte concentration increases above a certain value, the decrease of average distance between cation and anion can lead to more intensive interionic interaction and thereby limit the ionic mobility [115]. Such phenomena can be mathematically described using the activity coefficient (i.e., a function of the electrolyte ionic strength) [115, 143], providing a potential direction for future model extension.

3.5.2 Stage II: Film-free dissolution and transition to repassivation

We now perform simulations of localized corrosion inside pits with different depths in Stage II where the focus is repassivation. We take the constant temperature and concentration of the bulk solution as $T = 25$ °C and $C_{\text{bulk}} = 0.6$ M, respectively. All simulations are run until the final time t_{II} calibrated from the experimental data as detailed in Section 3.4.1 to ensure that the pit is repassivated. This stage is initialized by the conditions listed as follows

$$\widetilde{C}_i(\mathbf{x},0) \;=\; C_i(\mathbf{x},t_{\text{I}}) \;\text{ and }\; \phi(\mathbf{x},0) = \phi(\mathbf{x},t_{\text{I}}) \quad \text{in } \Omega_l. \tag{3.24}$$

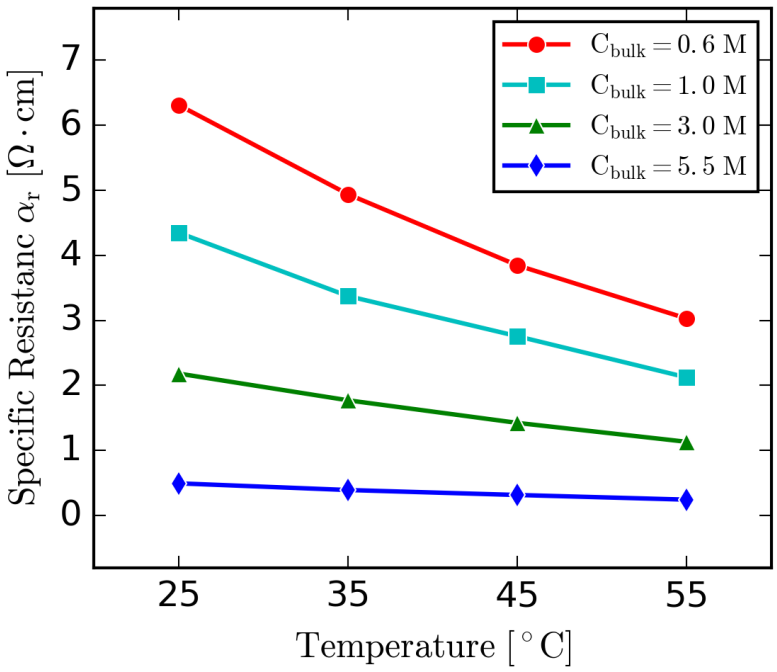

Figure 3.6: Parametric sensitivity of the pit specific resistance with respect to temperature T and bulk concentrations C_{bulk}.

where t_I represents the elapsed time of the corresponding Stage I simulation. Therefore, the initial electrochemical fields of Stage II are the saturated-state results obtained at the end of Stage I simulations. As noted in Section 3.4.1, the current density passing through the pit decreases with the decrease in applied electrical potential during Stage II. To accurately model the evolution of chemistry near the pit base during repassivation, it would be ideal to apply transient flux boundary conditions calibrated from the experimental data. However, Srinivasan and Kelly [138] showed that the critical pit chemistry determined using the transient flux boundary conditions is consistent with that determined using the constant flux boundary condition based on the repassivation current density i_{rp}. We therefore apply the simpler, constant flux boundary condition.

We first consider the pit with constant depth $d = 500$ μm as it is about to repassivate. In Figure 3.7, we compare the local chemistry inside the pit predicted by our model at the saturation and repassivation state. The dilution of metal cation at the corroding interface

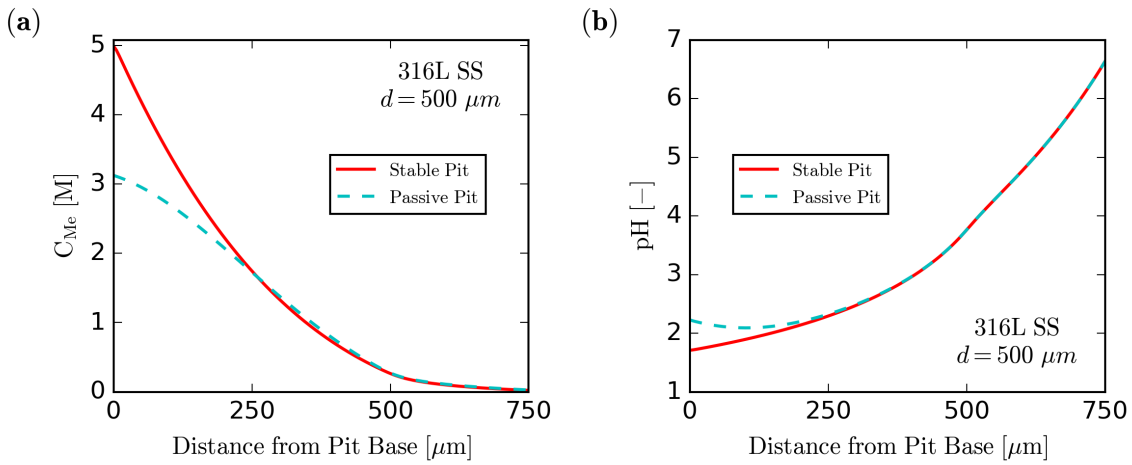

Figure 3.7: Comparison of the local chemistry inside the pit with depth $d = 500\mu$m at active (saturated state of Stage I) and passive (repassivated state of Stage II) states of pitting corrosion of 316L stainless steel wire within 0.6 M NaCl under room temperature $T =$ 25 °C: (a) Concentration of metal cation C_{Me}; (b) the pH.

is in evidence and the concentration of the metal cation at the pit base decreases from $C_{\text{sat}} = 5.02$ M to $61.16\%C_{\text{sat}} = 3.07$ M, as shown in Figure 3.7(a). There are two major mechanisms leading to the dilution of the metal cation at the pit base:

1. During the rapid polarization scan, the decrease of the applied electrical potential diminishes the current passing through the corroding surface. Therefore, the flux of metal cations entering the electrolyte via anodic dissolution at the pit base becomes almost negligible at the onset of repassivation;

2. Ion diffusion and electro-migration are controlled by the electrochemical potential gradient of the corresponding species [102]. Therefore the species of metal cations and salts will continuously move out of the pit, so long as the gradients of the concentration and/or the electrical potential exist, leading to the metal cation dilution during Stage II.

From Figure 3.7(b) we find that the pH near the corroding surface increases when the transition from pit stability to repassivation happens. As mentioned earlier, a sufficiently

low pH at the pit base is indicative that aggressive chemistry is necessary for continued pit stability is maintained. Therefore, an increase in pH at the pit base is naturally expected to take place for the pit to repassivate. Based on the qualitative analysis of the multi-species reactive transport model, we propose two underlying mechanisms that can cause the increase of the pH near the pit base:

1. The dilution of metal cations breaks the local chemical equilibrium of reactions listed in Section 3.4.4. To restore the chemical equilibrium, the hydrolysis of metal ions can occur in its backward direction, which consumes H^+ and produce metal cations. The consumption of H^+ can then lead to the production of OH^- through the water dissociation reaction and eventually cause the pH increase. We refer to this as the dilution-induced mechanism.

2. The local cathodic reaction, that is, the hydrogen electrode reaction, will be re-activated once the applied electrical potential approaches the repassivation potential. Therefore, the rate of the local cathodic reaction increases after the transition from pit stability to repassivation occurs. As the major product of the local cathodic reaction, the hydroxide ion causes a pH rise near the pit base. We refer to this as the HER-induced mechanism.

To further determine the dominant mechanism that leads to the pH increase near the corroding surface, we investigate the evolution of the critical chemistry at the pit base throughout stage II, as shown in Figure 3.8. The metal cation concentration at the pit base is continuously being diluted during Stage II as evident from Figure 3.8(a); whereas, the concentration of hydroxide ion at the pit base changes non-monotonically, that is, $[OH^-]$ increases initially, then decreases for a little while and eventually increases again. According to the previous analysis on the dilution-induced mechanism, the necessary condition for it to dominate the pH increase is that the concentration variation of both metal cation and hydroxide ion with respect to time should be synchronous. Therefore, in this study, the

dilution of metal cation cannot be the dominant mechanism that results in the pH increase near the pit base. To check that the HER-induced mechanism is dominant we calculate the flux of OH^- near the corroding surface. As depicted in Figure 3.8(b), we take an extremely small control volume at the pit base with the dimension of $1 \times 1\ \mu m^2$. To estimate the amount of OH^- inside the control volume, we compute the fluxes of OH^- passing through the top (f_t) and bottom (f_b) surfaces as

$$f_{t/b} = -D_{OH^-}\frac{\partial C_{OH^-}}{\partial y} + \frac{FD_{OH^-}C_{OH^-}}{R^*T}\frac{\partial \phi}{\partial y}, \tag{3.25}$$

where y is the vertical coordinate originated from the pit base. Two right hand side terms of Equation (3.25) correspond to the fluxes of ionic diffusion and electro-migration, respectively. And species entering into the volume is counted as positive flux, whereas species leaving from the volume as negative. The concentration of OH^- at the pit base can then be approximated as

$$C_{OH^-}(t) = C_{OH^-}(0) + \int (f_t + f_b)dt. \tag{3.26}$$

As shown in Figure 3.8(b), the bottom flux of hydroxide ion f_b is a positive constant, whereas the top flux of hydroxide ion f_t decreases sharply from positive to negative at the beginning of the repassivation stage and then keep increasing. At Stage II, because the repassivation current density is assumed to be constant, we enforce a constant flux of OH^- at the pit base as the boundary condition. Therefore, the bottom flux of hydroxide ion does not vary with time, which demonstrates that the change of OH^- concentration at the pit base is actually controlled by the top flux. The time evolution of the top flux can be well understood by analyzing the direction of hydroxide ion diffusion and electro-migration. Initially, the concentration of OH^- at the pit mouth is greater than that at the pit base, as shown in Figure 3.7(b). Thus, the direction of hydroxide ion diffusion inside the pit is from the mouth to the base. Because the direction of the electrical current is

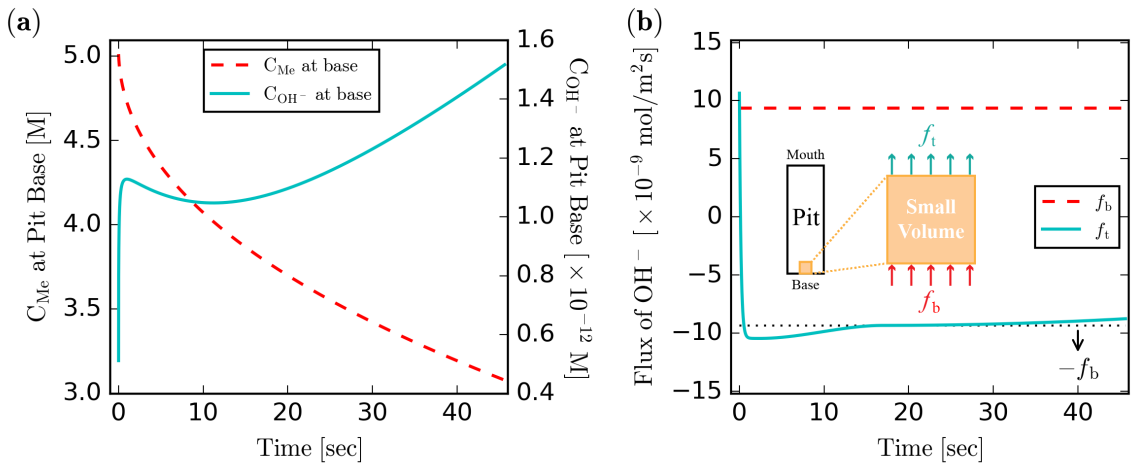

Figure 3.8: (a) Time dependence of metal cation and hydroxide ion concentration at the base of the pit with depth $d = 500\mu$m during Stage II under room temperature $T = 25$ °C in 0.6 M NaCl solution; (b) Schematic diagram of the pit base control volume and time dependence of the flux of hydroxide ion at the top and bottom surfaces of the volume.

always from the pit base to the pit mouth, the electrical potential is higher near the base and lower near the mouth. Considering the fact that OH^- is a negatively charged ion, its electro-migration direction is the same as the diffusion direction. Therefore, OH^- enters from both the top and bottom surface into the control volume at the beginning of Stage II, leading to the rapid increase of the hydroxide ion concentration at the pit base. However, such an increase causes the concentration of OH^- at the bottom surface to become greater than that at the top surface of the control volume. The diffusion direction of hydroxide ion inside the volume is then reversed (i.e., from the bottom to the top), which is the opposite of the electro-migration direction. Consequently, the electro-migration flux is offset by the diffusion flux at the top surface, and the hydroxide ion leaves the volume through the top surface because the diffusion gradually dominates the flux of OH^-. Despite the small increase in top flux at later times, the bottom flux remains the major source of increase in the hydroxide ion concentration inside the pit base control volume. Because the bottom flux of OH^- is generated from the local cathodic reaction, the HER-induced mechanism plays a dominant role in increasing the pH at the pit base.

We next evaluate the local chemistry at the base of pits with different depths when repassivation happens. As demonstrated in Figure 3.9, because the metal cation is saturated initially, the dilution of metal cation at the pit base occurs at all depths when repassivation happens but to different levels. Given the short diffusion length of the shallow pits, the concentration gradient of metal cation is greater than that of the deep pits. The species transport inside shallow pits is faster and hence the concentrations of the metal cations at the base of shallow pits are less than those at the base of deep pits. For sufficiently deep pits ($d/\varnothing > 8$), the critical surface concentration of metal cation is herein predicted to be in the range from 60% to 75% of saturation (3.012 to 3.765 M). Gaudet et al. [57] estimated the critical solution chemistry of pits approaching repassivation to be about 60% to 80% of saturation based on multiple intermediate steady states that follow the salt film-free dissolution of 304 stainless steel artificial pits . Ernst and Newman [51] determined the lower bound value for this concentration to be around 60% to 65% of saturation from artificial pit experiments on 316L stainless steel. Our prediction of the critical surface concentration is therefore consistent with these existing studies. Furthermore, we find that the pH of repassivation at the pit base is distinctly greater than the pH in the saturated state, as shown in Figure 3.9. As we argued above, the pH rise is mainly due to the production of hydroxide ion from the local cathodic reaction. Considering the fact that the flux of OH^- is a constant regardless of the pit depth, the increase of the pH at the pit base is actually proportional to the elapsed time of the second stage t_{II}. However, our predicted critical pH of repassivation is about 2.2, which is slightly less than the estimated critical pH of 2.65 that enables oxide nucleation [137]. Note that this simulated oxide nucleation pH is based on thermodynamics, which means any improved kinetic formulations can lead to the change of this estimation. Also, an underestimation of the ratio of the local cathodic current density to the anodic current density could have also resulted in the prediction of a lower repassivation pH as the OH^- is mainly produced via the local cathodic reaction.

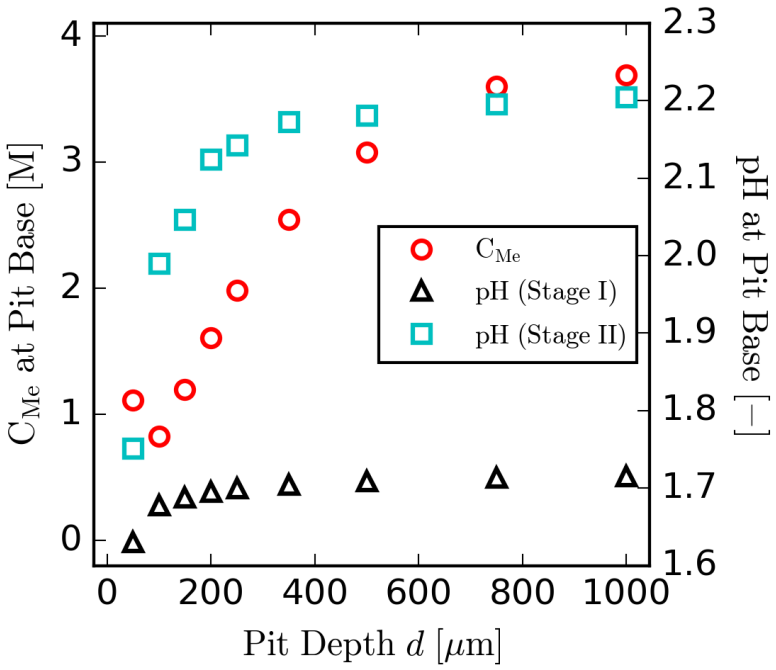

Figure 3.9: Numerical results of local chemistry inside the pit at the saturation (end of Stage I, replotted from Figure 3.3(a) for comparison) and the repassivation (end of Stage II) states for pitting corrosion of 316L stainless steel wire within 0.6 M NaCl solution under room temperature $T = 25$ °C: the concentration of metal cation and the pH at the pit base with respect to different pit depths.

3.6 Conclusions

In this chapter, we examined several critical electrochemical factors, including species concentrations, electrolyte pH and resistance, and electrical potential, for artificial pit experiments of 316L stainless steel wire using a multi-species reactive transport model. The electrolytic environment of experiments are highly-concentrated so that we implemented the extended Jones–Dole equation to estimate solution viscosity. The effects of viscosity and temperature on species diffusivity are considered and mathematically described using the Stokes-Einstein equation. The pit stability products and critical electrical potential (E_{T} and E_{rp}) collected from experiments are applied to estimate the electrode current density and the elapsed time of the simulation. We considered two stages of simulation based on the change of the electrical current density during the artificial pit experiments: stable dissolution under a salt film and film-free dissolution that transitions to repassivation. The main findings from these two sets simulations are:

1. At the saturated-state of Stage I, a salt film exists and the pH near the corroding surface is within the range of 1.63 to 1.71, which is small enough to sustain the aggressive chemistry necessary for sustained or stable pit growth. The predicted specific resistance of the pit solution shows a good agreement with the experiment results. For sufficiently deep pits, the specific resistance of electrolyte and the IR drop become constant. The effects of the temperature and the bulk concentration on pit electrochemical factors can be captured well using our model and are qualitatively consistent with existing experimental and numerical studies;

2. During Stage II, the dilution of metal cation and the increase of pH near the corroding surface from the range of $1.63 \sim 1.71$ to that of $1.76 \sim 2.21$ are evident from the numerical results. The dilution of metal cation at the pit base is due to the transport of corresponding species and the decrease of the anodic current density. The critical surface concentration of metal cation is predicted to be in the range from 60% to 75%

of saturation when repassivation occurs, assuming a current density at repassivation of 30 μA/cm^2. The pH increase at the pit base responsible for the onset of repassivation is a consequence of the contribution by the local cathodic reaction, which was suppressed during the high-rate anodic dissolution in Stage I.

In conclusion, the simulations conducted in this chapter are based on a more comprehensive multi-ionic reactive transport model, which provides a better description of species diffusion, electro-migration, and chemical reactions. These results provided an improved understanding of the critical electrochemical factors governing the transition from pit stability to repassivation in 316L stainless steel. The estimates of critical surface concentration that emerged from this study are central to developing accurate damage predictors such as maximum pit size for structural integrity analysis [34]. Additionally, useful insights into the influence of the local cathodic reaction at the dissolving pit base can be gained from this study. Our results qualitatively support and quantitatively improve the estimate of the pH at the corroding surface [137], which has been shown to be a key factor in inducing repassivation via oxide nucleation [106].

Chapter 4

A PHASE-FIELD PORO-DAMAGE MODEL FOR THE PROPAGATION OF WATER-FILLED CREVASSES IN GLACIERS AND ICE SHELVES

4.1 Introduction

Crevasses are predominantly mode I fractures and are ubiquitous in both Antarctic and Greenland glaciers and ice shelves. Most crevasses are shallow fractures as the longitudinal stress due to glacial deformation under self-gravity load changes from tensile to compressive at lower depths. Meltwater in surface crevasses and subglacial/ocean water in basal crevasses can apply pressure on crevasse walls and promote crevasse growth deeper into the glacier, a process that is often referred to as hydrofracture. Under certain conditions, water-filled crevasses can penetrate through the full thickness of the glacier leading to iceberg calving [19, 159, 165] and enhance basal sliding by altering subglacial hydrology [8, 80, 152]. However, the physical factors (e.g. glacier geometry, stress state, boundary conditions) enabling the full-depth propagation of hydrofractures are poorly understood. It is crucial that we investigate these factors in glacier and ice shelves to better describe iceberg calving and subglacial hydrology, which are two of most enigmatic glaciological processes. An advanced modeling approach for describing hydrofracture-driven ice shelf weakening and iceberg calving is essential to reducing the uncertainty in sea level rise projections. With this in mind, we develop a phase field model for hydrofracture of water-filled crevasses by extending the notion of poro-damage mechanics [99].

In the glaciology community, analytical linear elastic fracture mechanics (LEFM) models [134, 158, 159, 165] are still used to estimate the penetration depth of water-filled crevasses and predict iceberg calving [77, 79, 176]. However, analytical LEFM models use weight functions to evaluate the stress intensity factor by assuming idealized glacier geometries (e.g. rectangular) and basal boundary conditions (e.g. traction free or symmetric

edge), so their relevance to iceberg calving of real glaciers and ice shelves is somewhat limited [69]. Moreover, LEFM models only describe crack propagation, so *ad hoc* criteria are often necessary to describe when/where a crack will nucleate, and how much and in which direction it will propagate [54], but these criteria can alter crack trajectories and lead to non-physical outcomes [24, 48]. Despite advances in the numerical implementations of LEFM model [23, 61, 93, 135, 146], the underlying algorithms can be cumbersome and simulating crack branching and coalescence can still be challenging.

In contrast, continuum damage mechanics (CDM) models can describe both nucleation and propagation of cracks, including crack length and orientation [30, 100, 110, 113]. Specifically, CDM models describing creep fracture of glaciers [44, 45, 71, 116] can handle arbitrary glacier geometries and basal boundary conditions, without requiring complicated crack tracking algorithms or the assumption of pre-existing cracks. However, phenomenological CDM models can involve several empirical parameters and may not be thermodynamically or variationally consistent for describing brittle fracture. In contrast, cohesive zone models (CZMs), which can be categorized as a special type of CDM [6, 70, 85] can describe mixed-mode fracture propagation consistently with LEFM models. Although CZMs can describe both crack initiation and propagation, a major limitation is that special interface elements need to be inserted into the finite element mesh either a priori or dynamically, which can introduce additional mesh dependency issues or algorithmic complexity [1, 4, 58]. Nevertheless, CZMs have been implemented to simulate hydraulically drive fracture in two and three dimensions [29, 130].

To address the shortcomings of the LEFM and CDM models, the phase field model (PFM) for fracture introduced in the seminal works of [25, 54] that describes crack propagation in solids by minimizing the total potential energy based on Griffith's theory [60]. The PFM for fracture can be categorized as a continuum damage model, and as such enables robust simulation of complex crack growth, including crack initiation, propagation, and branching and merging. For brittle fracture, the crack is defined by a diffused damage

zone and material failure is characterized by a constitutive damage relation arising from variational [25] or thermodynamical arguments [96]. Kuhn and Müller [78] augmented Bourdin et al. [25] model by a Ginzburg-Landau type evolution equation for the phase-field/damage variable and incorporated an additional mobility parameter by representing cracking as a phase transition process. A major limitation of the phase-field models is its inability to capture asymmetric damage growth under multi-axial and mixed tensile and compressive stress states. To avoid the growth of damage under compression in PFMs and inter-penetr-ation of crack surfaces, *ad hoc* approaches were proposed based on: volumetric/deviatoric split of strain energy [11], spectral decomposition (positive/negative split) of strain tensor [95]. Hybrid formulations were also proposed with spectral decomposition of strain tensor only applied to damage evolution for tensile fracture [10].

In the past few years, numerous extensions and advanced implementations of PFMs for dynamic, cohesive and fatigue crack propagation have been developed [86, 117, 127, 160]. A comprehensive review of these developments is beyond the scope of this chapter, so here we limit the discussion to articles that proposed improvements to crack driving force functions for describing fracture under mixed-mode, compression-shear, and/or hydraulic loadings. Zhang et al. [177] proposed normalizing the volumetric and deviatoric part of the strain energy with fracture energy under pure mode I (opening) and mode II (sliding) loading, respectively, to define the crack driving force under mixed-mode loading, which was later extended to anisotropic rocks in [26]. However, this energy splitting approach can still unphysically evolve damage under certain stress states with all negative principal stress [167] and does not capture the crack boundary conditions correctly under compression and shear [142]. Zhou et al. [178] proposed a new crack driving force function to capture compression-shear fractures in rock-like materials that was validated with uniaxial compression tests. Santillán et al. [122, 123] developed a phase field model of hydraulic fracturing in poroelastic media, where they used the spectral decomposition scheme [95].

Despite recent advances, the phase field formulation is not still not well-established to

simulate fracture in geological media under self-gravity loading. Here we demonstrate that the multi-axial stress state and (flexure-like) tensile-compressive stress variation along with low fracture toughness of glacier results in unphysical damage patterns and computational challenges for existing PFMs. In this chapter, we take the first step towards extending the PFM to simulate quasi-static hydrofracture propagation and understand the conditions enabling the full-depth crevasses in glaciers and ice shelves due to surface melt water or basal ocean water. Unlike hydraulic fracture of rocks under high pressure, where fluid flow rate dictates the fracture process, we assume that water-filled crevasses can be modeled to propagate under quasi-static conditions using the poro-damage approach [47, 99]. Additionally, we assume that glacier ice on smaller time scales of crevasse propagation can exhibit compressible elastic behavior based on observational data [155]. The novelty and contribution of this objective is threefold:

1. We illustrate that the crack driving force function presented in Lo et al. [86] along with a fracture toughness threshold is a viable option for simulating tensile fracture in self-gravitating glaciers and ice shelves (which broadly applies to geological media);

2. We establish a thermodynamically-consistent alternative to the nonlocal continuum poro-damage mechanics model for quasi-static hydrofracture of glaciers and ice shelves [47];

3. We derive the analytical stress solution of compressible linear elastic glaciers based on theory of elasticity and membrane assumption, and compare the PFM results with those against the stress intensity factor based LEFM model for crevasse propagation [69, 77].

The rest of this chapter is organized as follows: in Section 4.2, we review the phase-field formulation for brittle fracture and extend it to simulate quasi-static hydrofracture based on the notion of poro-damage mechanics; in Section 4.3, we summarize the strategy adopted to solve the hybrid poro-damage phase-field model and implement it using the

standard finite element method; in Section 4.4, we compare the predictions of crevasses depths for grounded glaciers and floating ice shelves using the phase field method against that using the linear elastic fracture mechanics models; in Section 4.5, we conclude with a brief summary and closing remarks.

4.2 Model Formulation

In this section, we first review the fundamental concepts of the phase field model, where the brittle fracture is described by a scalar order parameter, that is, the phase-field damage variable. We next propose modified phase-field formulation for hydrofracture based on the notion of poro-damage mechanics that incorporates hydraulic pressure within the cracks and voids situated in the nonlocal damage zone. Finally, we summarize the strong form of the governing equations of the phase-field poro-damage model for quasi-static hydrofracture and the corresponding boundary conditions.

4.2.1 Review of phase-field formulation for brittle fracture

We consider an arbitrary solid domain $\Omega \subset \mathbb{R}^n$ with $n = 2$ in two dimensions, as shown in Figure 4.1. The domain Ω has an external boundary $\partial\Omega$ and an embedded crack interface that can be explicitly represented as a sharp discontinuity Γ or implicitly captured as a smooth damage zone using the phase-field variable $D(\mathbf{x},t)$. The boundary $\partial\Omega_u$ is enforced by the Dirichlet boundary condition with a prescribed displacement $\boldsymbol{u}^*$. Another partition of the external boundary $\partial\Omega_t$ is enforced by the Neumann boundary condition with an imposed traction $\boldsymbol{t}^*$. Boundaries $\partial\Omega_u$ and $\partial\Omega_t$ are two disjoint parts of $\partial\Omega$ such that $\partial\Omega_u \cap \partial\Omega_t = \emptyset$.

Based on Griffith's theory of brittle fracture [60], the total energy stored in a cracked solid body (Ψ) includes internal (Ψ_{int}) and external (Ψ_{ext}) components, which can be expressed as

$$\Psi = \Psi_{\text{int}} - \Psi_{\text{ext}} = \Psi_{\text{E}} + \Psi_{\text{D}} - \Psi_{\text{ext}}, \tag{4.1}$$

where Ψ_{E} is the elastic energy of Ω, and Ψ_{D} the fracture energy needed for the propagation of the crack interface Γ. The small strain tensor $\boldsymbol{\varepsilon}$ is defined by the symmetric part of the

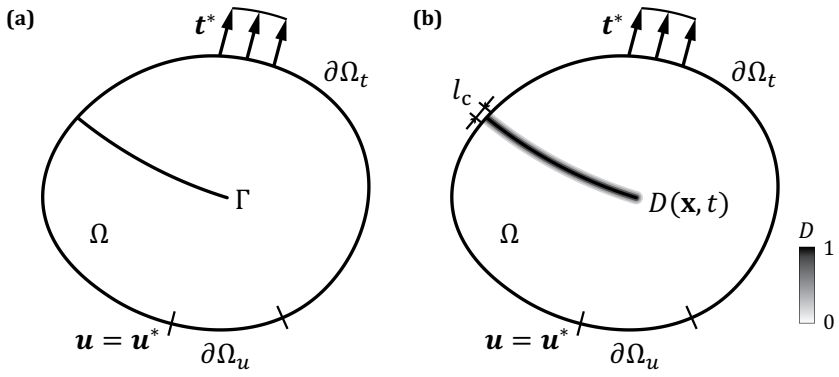

Figure 4.1: Schematic diagrams of the domain Ω with: (a) an internal sharp crack interface Γ; (b) a diffuse crack interface described by the phase-field damage variable $D(\mathbf{x},t) \in [0,1]$. The length scale of the diffuse interface is denoted by l_c.

displacement gradient tensor as given by

$$\varepsilon = \frac{1}{2}\left(\nabla \boldsymbol{u} + \nabla \boldsymbol{u}^{\mathrm{T}}\right). \tag{4.2}$$

where ∇ is the spatial gradient operator and $\boldsymbol{u}$ is the displacement vector. The damage state of a material point at position $\mathbf{x}$ at time t is given by $D(\mathbf{x},t) \in [0,1]$, such that $D = 0$ represents undamaged state and $D = 1$ the fully damaged state. The internal energy of the solid Ψ_{int} can be calculated as

$$\Psi_{\mathrm{int}} = \Psi_{\mathrm{E}} + \Psi_{\mathrm{D}} = \int_{\Omega} \psi_{\mathrm{e}}(\varepsilon, D)\, \mathrm{d}\Omega + \int_{\Gamma} \mathscr{G}_{\mathrm{c}}\, \mathrm{d}\Gamma, \tag{4.3}$$

where ψ_{e} is the elastic strain energy density function and $\mathscr{G}_{\mathrm{c}}$ is the critical strain energy release rate. The width of the diffuse interface is controlled by the length scale parameter l_{c} and its appropriate choice can provide experimentally supported crack growth prediction [111]. The fracture energy can then be approximated as

$$\Psi_{\mathrm{D}} = \int_{\Gamma} \mathscr{G}_{\mathrm{c}} \mathrm{d}\Gamma \approx \int_{\Omega} \mathscr{G}_{\mathrm{c}} \left(\frac{D^2}{2l_{\mathrm{c}}} + \frac{l_{\mathrm{c}}}{2}|\nabla D|^2\right) \mathrm{d}\Omega. \tag{4.4}$$

For isotropic linear elasticity, the strain energy density function of intact material ψ_{e}^0 is

given by

$$\psi_{\mathrm{e}}^{0}(\varepsilon) = \frac{\lambda}{2}\left(\mathrm{tr}(\varepsilon)\right)^{2} + \mu\ \mathrm{tr}(\varepsilon^{2}), \tag{4.5}$$

where λ and μ are the Lamé parameters. In the hybrid phase-field formulation for fracture [10], the strain energy density function of damaged material ψ_{e} is approximated as

$$\psi_{\mathrm{e}}(\varepsilon, D) = g_{\mathrm{d}}(D)\,\psi_{\mathrm{e}}^{0}(\varepsilon), \tag{4.6}$$

where we assume the quadratic degradation function $g_{\mathrm{d}} = (1-D)^{2}$. Therefore, the Cauchy stress tensor can be obtained as

$$\boldsymbol{\sigma} = \frac{\partial \psi_{\mathrm{e}}}{\partial \varepsilon} = g_{\mathrm{d}}(D)\left[\lambda\,\mathrm{tr}(\varepsilon)\boldsymbol{I} + 2\mu\varepsilon\right], \tag{4.7}$$

where $\boldsymbol{I}$ represents the identity tensor. However, Equation (4.6) can lead to physically unrealistic energy release due to fracture in both tension and compression. To remedy this issue, Miehe et al. [96] conducted an assumed additive decomposition of the elastic strain energy density and modified Equation (4.6) as

$$\psi_{\mathrm{e}}(\varepsilon, D) = g_{\mathrm{d}}(D)\,\psi_{\mathrm{e}}^{+}(\varepsilon) + \psi_{\mathrm{e}}^{-}(\varepsilon), \tag{4.8}$$

where ψ_{e}^{+} and ψ_{e}^{-} represent the contribution to the elastic strain energy from tensile and compressive strain states. The Cauchy stress tensor based on strain energy decomposition is defined as

$$\boldsymbol{\sigma} = \frac{\partial \psi_{\mathrm{e}}}{\partial \varepsilon} = g_{\mathrm{d}}(D)\frac{\partial \psi_{\mathrm{e}}^{+}}{\partial \varepsilon} + \frac{\partial \psi_{\mathrm{e}}^{-}}{\partial \varepsilon}. \tag{4.9}$$

Furthermore, the external energy of the solid Ψ_{ext} can be calculated as

$$\Psi_{\mathrm{ext}} = \int_{\Omega} \boldsymbol{b}\cdot\boldsymbol{u}\ \mathrm{d}\Omega + \int_{\partial\Omega_{u}} \boldsymbol{t}^{*}\cdot\boldsymbol{u}\ \mathrm{d}\Gamma, \tag{4.10}$$

where $\boldsymbol{b}$ represents the body force. Following Miehe et al. [95], the time evolution of

phase-field variable can be obtained by minimizing the total potential energy functional as

$$\eta\dot{D} = \frac{\partial\Psi}{\partial D} - \boldsymbol{\nabla}\cdot\left(\frac{\partial\Psi}{\partial\boldsymbol{\nabla}D}\right) = l_{\mathrm{c}}\boldsymbol{\Delta}D - \frac{D}{l_{\mathrm{c}}} + 2(1-D)\frac{\mathscr{H}}{\mathscr{G}_{\mathrm{c}}}, \tag{4.11}$$

where $\boldsymbol{\Delta} = \boldsymbol{\nabla}\cdot\boldsymbol{\nabla}$ is the Laplace operator, η is the viscous regularization parameter defined for numerical stabilization, and $\mathscr{H}$ the history field variable that ensures monotonic increase of the phase-field variable. Here we evaluate three different schemes for calculating the history field variable that were proposed in the literature.

Miehe's scheme: Miehe et al. [95] defined the history field variable as

$$\mathscr{H}(\mathbf{x},t) = \max_{\tau\in[0,t]} \psi_{\mathrm{e}}^{+}(\boldsymbol{\varepsilon}(\mathbf{x},\tau)), \tag{4.12}$$

where the positive component of elastic strain energy ψ_{e}^{+} is given by

$$\psi_{\mathrm{e}}^{+}(\boldsymbol{\varepsilon}) = \frac{\lambda}{2}\langle\mathrm{tr}(\boldsymbol{\varepsilon})\rangle^2 + \mu\,\mathrm{tr}(\langle\boldsymbol{\varepsilon}\rangle^2), \tag{4.13}$$

where $\langle\cdot\rangle = (\cdot + |\cdot|)/2$ denotes the Macaulay's bracket.

Zhang's scheme: To handle mixed mode fracture, Zhang et al. [177] defined the history field variable as

$$\mathscr{H}(\mathbf{x},t) = \max_{\tau\in[0,t]} \left(\frac{\mathscr{H}_{\mathrm{I}}(\mathbf{x},\tau)}{\mathscr{G}_{\mathrm{cI}}} + \frac{\mathscr{H}_{\mathrm{II}}(\mathbf{x},\tau)}{\mathscr{G}_{\mathrm{cII}}}\right)\mathscr{G}_{\mathrm{c}}, \tag{4.14}$$

where $\mathscr{H}_{\mathrm{I}} = \frac{\lambda}{2}\langle\mathrm{tr}(\boldsymbol{\varepsilon})\rangle^2$ and $\mathscr{H}_{\mathrm{II}} = \mu\,\mathrm{tr}(\langle\boldsymbol{\varepsilon}\rangle^2)$ are history field variables contributing to mode I and mode II fracture, respectively. Notably, Zhang's scheme based on Equation (4.14) recovers to Miehe's when G_{cII} is taken as the same as G_{cI}.

Lo's scheme: Lo et al. [86] asserted that the strain energy decomposition scheme proposed by Miehe et al. [96] does not guarantee the prohibition of damage accumulation in compressive regions due to Poisson's ratio effects. Therefore, they implemented a different decomposition scheme in three dimensions to ensure that compressive stresses do not contribute to crack growth. We reduce their formulation for the two-dimensional (2D) plane

strain case as follows:

$$\begin{cases} \textbf{if } \varepsilon_1 \geq \varepsilon_2 \geq 0, \\ \quad \textbf{then } \psi_e^+ = \frac{\lambda}{2}(\varepsilon_1+\varepsilon_2)^2 + \mu(\varepsilon_1^2+\varepsilon_1^2); \\ \textbf{elseif } \varepsilon_1 \geq 0 \geq \varepsilon_2 \textbf{ and } (1-\nu)\varepsilon_1 + \nu\varepsilon_2 > 0, \\ \quad \textbf{then } \psi_e^+ = \dfrac{E\left[(1-\nu)\varepsilon_1+\nu\varepsilon_2\right]^2}{2(1-2\nu)(1-\nu^2)}; \\ \textbf{else } \psi_e^+ = 0. \end{cases} \tag{4.15}$$

where $\varepsilon_1 \geq \varepsilon_2$ are taken as the ordered principal strains. The history field variable can then be updated using Equation (4.12).

4.2.2 Phase-field poro-damage approximation for quasi-static hydrofracture

We extend the phase-field formulation using the notion of poro-damage mechanics to simulate the propagation of fluid-filled fractures in geological media. As depicted in Figure 4.2, the specific physical problem consists of a glacier crevasse filled with either air or water depending on the water level within the damaged region ($D > 0$). Because the crevasse region is much smaller compared to the entire glacier or ice-shelf, we approximate it as a thin, finite-thickness damage zone. We also consider the plane strain approximation to simulate the crevasse problem in 2D, and thus reduce the computational burden. Five different physical representative volume elements (RVE) can be conceived to exist in the glacier domain. Figure 4.2(a) shows an intact physical RVE ($D = 0$) that does not contain microcracks or microvoids. Figures 4.2(b) and (d) show the damaged physical RVEs ($0 < D < 1$) where microvoids and microcracks are filled with air and water, respectively. Figures 4.2(c) and (e) show the fully damaged physical RVEs ($D = 1$) with a macrocrack that are located above and beneath the water level, respectively. The isotropic phase-field damage variable can be interpreted as the ratio of the area of microcracks and microvoids to the total area of the maximum principal plane. Thus, it is inherently related to porosity defined as the ratio

of the volume of microvoids to the total volume of the RVE.

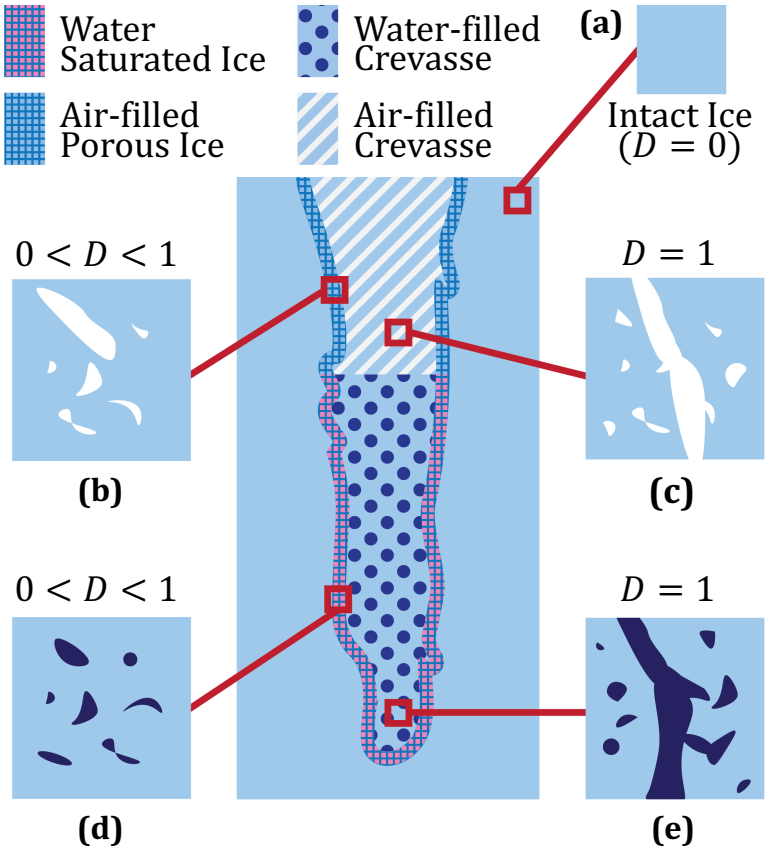

Figure 4.2: Schematic illustration of the damaged glacier. The fully damaged region ($D = 1$) of the crevasse is filled with either air or water depending on the assumed water level within the crevasse. The principal planes of the physical representative volume elements (RVE) for (a) intact ice ($D = 0$); (b) cracking ice with air-filled microcracks and microvoids ($0 < D < 1$); (c) air-filled broken ice ($D = 1$); (d) water saturated cracking ice ($0 < D < 1$); (e) water-filled broken ice ($D = 1$).

To account for the effect of fluid/poroelastic pressure on crack propagation, we interpret the damaged region of the crevasse beneath the water level as a fluid-saturated poroelastic medium. The total internal energy stored in this region can then be defined as

$$\Psi_{\text{int}} = \Psi_{\text{E}} + \Psi_{\text{D}} + \Psi_{\text{F}}, \tag{4.16}$$

where Ψ_{F} is the potential energy stored in the fluid. In the fully damaged region Ω_{D} of the

diffuse damage zone, the potential energy stored in the fluid (water) can be defined as [97]

$$\Psi_{\mathrm{F}} = \int_{\Omega_{\mathrm{D}}} \psi_{\mathrm{f}}(p, \boldsymbol{\nabla} \cdot \boldsymbol{u}) \, \mathrm{d}\Omega, \tag{4.17}$$

where p is the fluid/poroelastic pressure, and ψ_{f} is the potential energy density of the fluid. We assume water within the crevasse to be flowing slow enough and at times stagnant, so that the hydrostatic condition applies. In other words, we assume the fluid/poroelastic pressure within the fully damaged region is equal to the hydrostatic pressure p_{w}. The potential energy density of the fluid inside Ω_{D} can then be calculated as

$$\psi_{\mathrm{f}}(p, \boldsymbol{\nabla} \cdot \boldsymbol{u}) = -p\alpha \boldsymbol{\nabla} \cdot \boldsymbol{u} = -p_{\mathrm{w}} \alpha \mathrm{tr}(\boldsymbol{\varepsilon}), \tag{4.18}$$

where α is the Biot coefficient.

The hydrostatic/hydraulic pressure within the damaged region can be calculated by simply determining the water depth at a specific location. For illustration, consider a glacier that terminates at the ocean with a seawater level h_{w} containing both surface and basal crevasses, as shown in Figure 4.3. The depths of surface and basal crevasses are denoted by d_{s} and d_{b}, respectively. The surface crevasses can either partially or fully filled with freshwater depending on available amount of surface meltwater, so the water level of surface crevasses h_{s} is an independent variable. In contrast, the basal crevasses are assumed to be hydrologically connected to the external ocean water through 3-D networks of basal channels [17]. Thus, the basal crevasse is fully-filled with seawater if its crack tip is below the seawater level h_{w}, or partially filled with seawater up to h_{w} if the crack tip is above the seawater level. With the origin at the glacier base, we define the hydraulic pressure as

$$p_{\mathrm{w}}(z) = \begin{cases} \rho_{\mathrm{f}} g \langle h_{\mathrm{s}} - (z - z_{\mathrm{s}}) \rangle & \text{in surface crevasses,} \\ \rho_{\mathrm{s}} g \langle h_{\mathrm{w}} - z \rangle & \text{in basal crevasses,} \end{cases} \tag{4.19}$$

where g is the gravitational acceleration. In this chapter, we use the Cartesian coordinate system with $(x_1, x_2, x_3) = (x, y, z)$, where x and z represent in-plane horizontal and vertical coordinates, respectively; and the direction of y-axis must point into the x-z plane to obey the right-handed rule. Furthermore, we use z_s to denote the vertical coordinate of the surface crevasse tip in Equation (4.19).

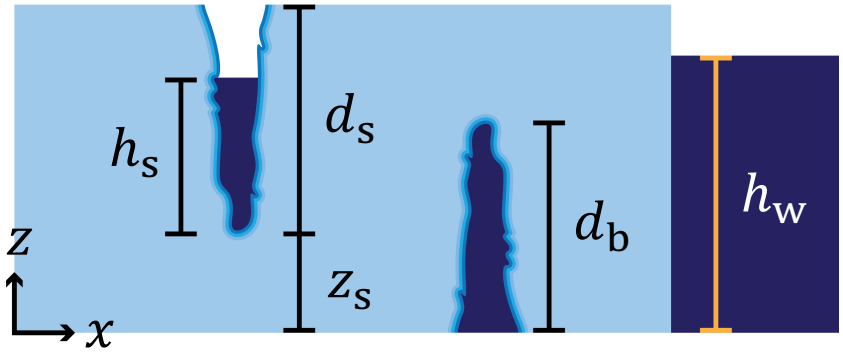

Figure 4.3: Schematic diagram of the glacier with both surface and basal crevasses. Seawater level at the terminus is denoted by h_w. Surface crevasse depth is d_s and freshwater level within the surface crevasse is h_s. Basal crevasse depth is d_b. To calculate hydraulic pressure p_w, the origin is set at the lower-left corner with x and z denoting the horizontal and vertical coordinates, respectively. The vertical coordinate of the surface crevasse tip is z_s.

Note that the integral in Equation (4.17) is defined over the fully damaged region Ω_D, which changes in size as the crack propagates. To account for the effect of fluid/poroelastic pressure in the entire the diffuse crack region ($0 < D \leq 1$), we modify Equation (4.18) as

$$\psi_f(p, \nabla \cdot \boldsymbol{u}, D) = -g_f(D) p_w \alpha \nabla \cdot \boldsymbol{u}, \tag{4.20}$$

where $g_f(D) = 1 - g_d(D)$ is an interpolation function that satisfies three conditions as

$$g_f(0) = 0,\ g_f(1) = 1,\ g_f'(1) = 0. \tag{4.21}$$

The first condition indicates that no fluid energy is stored in intact elastic medium, which

contains no microcrack or microvoid. The second condition ensures that Equation (4.20) reduces to Equation (4.17) in the fully-damage region (i.e. $D = 1$). The third condition ensures that the crack driving force leading to hydrofracture converges to a finite value if the phase-field variable converges to 1. The modified definition in Equation (4.20) allows us to define the integral in Equation (4.17) over the whole domain Ω, instead of just over Ω_{D}.

We employ the hybrid approach to solve the PFM for hydrofracture and decompose elastic strain energy only for calculation of the history field variable $\mathscr{H}$. Thus, the Cauchy stress tensor can be obtained as

$$\boldsymbol{\sigma} = \frac{\partial \psi}{\partial \varepsilon} = \frac{\partial \psi_{\mathrm{e}}}{\partial \varepsilon} + \frac{\partial \psi_{\mathrm{f}}}{\partial \varepsilon} = g_{\mathrm{d}}(D)\left[\lambda \mathrm{tr}(\varepsilon)\boldsymbol{I} + 2\mu\varepsilon\right] - g_{\mathrm{f}}(D) p_{\mathrm{w}} \alpha \boldsymbol{I}, \tag{4.22}$$

To further regularize the formulation, we modify the constitutive equation (4.22) as

$$\boldsymbol{\sigma} = \max\left(g_{\mathrm{d}}(D), \kappa\right)\left[\lambda \mathrm{tr}(\varepsilon)\boldsymbol{I} + 2\mu\varepsilon\right] - g_{\mathrm{f}}(D) p_{\mathrm{w}} \alpha \boldsymbol{I}, \tag{4.23}$$

where κ is a numerical parameter. Specifically, the value of κ is taken as 10^{-6} if $D = 1$, and 0 if $D < 1$. We note that the expression $\max\left(g_{\mathrm{d}}(D), \kappa\right)$ essentially the same as $(1-\kappa)g_{\mathrm{d}}(D) + \kappa$, which is more commonly used [178]. The phase-field evolution equation can be obtained by minimizing the modified total potential energy functional as

$$\eta \dot{D} = l_{\mathrm{c}} \boldsymbol{\Delta} D - \frac{D}{l_{\mathrm{c}}} + 2(1-D)\frac{\mathscr{H}}{\mathscr{G}_{\mathrm{c}}}, \tag{4.24}$$

where the history variable is given by

$$\mathscr{H}(\mathbf{x}, t) = \max_{\tau \in [0,t]} \left[\psi_{\mathrm{e}}^{+}\left(\varepsilon(\mathbf{x}, \tau)\right) + p_{\mathrm{w}} \alpha \mathrm{tr}\left(\varepsilon(\mathbf{x}, \tau)\right)\right]. \tag{4.25}$$

The phase-field poro-damage formulation here can model the propagation of both air-filled

and water-filled crevasses. Specifically, the constitutive relation is defined by Equation (4.23) and the history field variable is defined by Equation (4.25) with the positive elastic strain energy defined using the Lo's scheme in Equation (4.15). For air-filled crevasses, the poroelastic pressure $p = 0$ everywhere within Ω, which corresponds to the case when there is no surface melt water. In this case, the phase-field poro-damage formulation for hydrofracture reduces to that for brittle fracture introduced in Section 4.2.1.

4.2.3 Strong form of governing equations

The displacement field $\boldsymbol{u}$ is obtained by solving the elastostatic boundary value problem. The strong form of the corresponding governing equations and the boundary conditions are:

$$\begin{cases} \boldsymbol{\nabla} \cdot \boldsymbol{\sigma} + \boldsymbol{b} = 0 & \text{in } \Omega, \\ \boldsymbol{u} = \boldsymbol{u}^* & \text{on } \partial\Omega_{\mathrm{u}}, \\ \boldsymbol{\sigma} \cdot \mathbf{n} = \boldsymbol{t}^* & \text{on } \partial\Omega_{\mathrm{t}}, \end{cases} \tag{4.26}$$

where $\mathbf{n}$ denotes the unit normal to the boundary $\partial\Omega$ pointing outward from Ω, and the Cauchy stress $\boldsymbol{\sigma}$ is calculated using the constitutive equation (4.23). We apply self-weight as the body force with the magnitude of $-\rho g$ in the z-direction. Material density ρ is determined based on the interpretation of the phase-field variable as porosity, and can be calculated as

$$\rho = (1 - D)\rho_{\mathrm{i}} + D\rho_{\mathrm{w}}, \tag{4.27}$$

where ρ_{i} and ρ_{w} are densities of ice and water, respectively. For surface crevasses, ρ_{w} is taken as the density of freshwater ρ_{f}; and for basal crevasses, ρ_{w} is taken as the density of seawater ρ_{s}. The governing equation of phase-field variable evolution in the rate form and

the associated boundary condition are:

$$\begin{cases} \eta \dot{D} = l_{\mathrm{c}} \boldsymbol{\Delta} D - \frac{D}{l_{\mathrm{c}}} + 2(1-D)\frac{\mathscr{H}}{\mathscr{G}_{\mathrm{c}}} & \text{in } \Omega, \\ \boldsymbol{\nabla} D \cdot \mathbf{n} = 0 & \text{on } \partial\Omega. \end{cases} \tag{4.28}$$

4.3 Numerical Implementation

In this section, we first introduce the operator-splitting strategy adopted for solving the hybrid formulation of the phase field model. We next detail its implementation based on the standard finite element method.

4.3.1 Solution strategy

The hybrid phase-field formulation allows damage accumulation driven by the tensile elastic strain energy, but assumes the simpler constitutive damage law for defining the Cauchy stress, which significantly reduces the computational burden [10]. This feature of the hybrid formulation enables the usage of the staggered scheme, which provides greater flexibility and stability compared with the monolithic scheme [178]. In this study, we employ a three-step staggered numerical solution strategy at any given pseudo time increment as follows:

1. Compute the displacement $\boldsymbol{u}$ using static equilibrium along with its boundary conditions defined in Equation (4.26) and the constitutive damage law defined by Equation (4.23);

2. Compute the tensile elastic strain energy ψ_{e}^{+} and/or the history variable $\mathscr{H}$ using Equations (4.12), (4.14), or (4.25), then update the crack driving force $\mathscr{H}/\mathscr{G}_{\mathrm{c}}$;

3. Compute the isotropic damage variable D by solving the phase-field evolution equation (4.28).

As shown in Figure 4.4, we use the flowchart to illustrate our staggered implementation of the hybrid (decoupled) phase field model. The magenta arrows and numbers in blocks represent the direction and sequence of data transfer at the n^{th} pseudo time step.

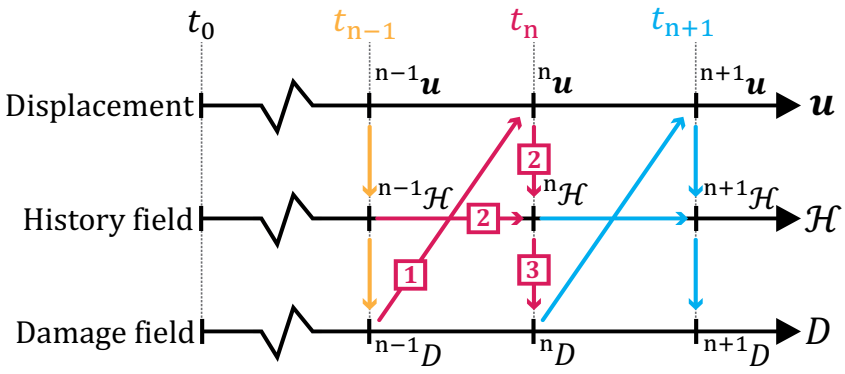

Figure 4.4: Flowchart of the staggered numerical solution strategy implemented to solve the hybrid phase field model.

4.3.2 Finite element approximation

We discretize and solve the governing equations of the PFM using the standard finite element method in the open-source software FEniCS [9]. The domain Ω is spatially discretized using three-noded triangular finite elements. At the pseudo time increment $n+1$, the time derivative of the phase-field variable D can be approximated based on the backward Euler scheme as

$$\dot{D} = \frac{^{n+1}D - {}^{n}D}{\Delta t}, \tag{4.29}$$

where Δt is the size of the pseudo time increment, and the left superscript index denotes the time increment. The Galerkin weak form for establishing the displacement and phase field at the pseudo time increment $n+1$ can be stated as follows:

Find $\tilde{\boldsymbol{u}} \in \mathscr{V}$ and $\tilde{D} \in \mathscr{S}$ such that $\forall\ \boldsymbol{v} \in \mathscr{V}$ and $\omega \in \mathscr{S}$,

$$\int_\Omega \boldsymbol{\sigma}(\tilde{\boldsymbol{u}}, {}^{n}D) : \boldsymbol{\varepsilon}(\boldsymbol{v})\, \mathrm{d}\Omega = \int_\Omega \boldsymbol{b}\cdot\boldsymbol{v}\, \mathrm{d}\Omega + \int_{\partial\Omega_t} \boldsymbol{t}^*\cdot\boldsymbol{v}\, \mathrm{d}S, \tag{4.30}$$

and

$$\begin{aligned}\int_\Omega \left\{ l_c \boldsymbol{\nabla}\tilde{D}\cdot\boldsymbol{\nabla}\omega + \left[\frac{\eta}{\Delta t} + \frac{1}{l_c} + \frac{2\mathscr{H}(^{n+1}\boldsymbol{u})}{\mathscr{G}_c}\right]\tilde{D}\omega \right\} \mathrm{d}\Omega \\ = \int_\Omega \left[\frac{2\mathscr{H}(^{n+1}\boldsymbol{u})}{\mathscr{G}_c}\omega + \frac{\eta}{\Delta t}\,{}^{n}D\omega\right] \mathrm{d}\Omega,\end{aligned} \tag{4.31}$$

where $\tilde{\boldsymbol{u}}$ and $\tilde{D}$ are trial functions corresponding to the displacement and phase field, and $\boldsymbol{v}$ as well as ω are test functions for the displacement and phase field, respectively. The appropriate vector and scalar function spaces are denoted by $\mathscr{V}$ and $\mathscr{S}$, respectively. To check the accuracy of our hybrid PFM implementation, we considered the benchmark test involving a single edge cracked specimen under unaxial tension using three different strain energy decomposition schemes introduced in Section 4.2.1. For more details see Appendix H.

4.4 Results and Discussion

In this section, we use the PFM for hydrofracture to simulate water-filled crevasse propagation in grounded glaciers and floating ice shelves. We then compare the predicted maximum crevasse depths against with those obtained from the linear elastic fracture mechanics (LEFM) model detailed in Appendix I. Glacier ice on smaller time scales of crevasse propagation is considered to exhibit compressible elastic behavior. Material properties and related phase field parameters assumed in this study are listed in Table 4.1. These properties are generally assumed from our prior studies [43, 47], and do not account for those of actual glacier ice cores [37, 118].

Table 4.1: Material properties of compressible, linear elastic ice and phase-field parameters for modeling the propagation of glacier crevasses. The Young's modulus and Poisson's ratio of ice are assumed from [43], and the densities of glacier ice and seawater are assumed from [69].

Parameter	Symbol	Value [Unit]
Biot coefficient	α	1.0 $[-]$
Viscous regularization parameter	η	50 $[\mathrm{N \cdot s/m^2}]$
Poisson's ratio	ν	0.35 $[-]$
Freshwater density	ρ_{f}	1000 $[\mathrm{kg/m^3}]$
Ice density	ρ_{i}	917 $[\mathrm{kg/m^3}]$
Seawater density	ρ_{s}	1020 $[\mathrm{kg/m^3}]$
Young's modulus	E	9500 [MPa]
Gravitational acceleration	g	9.81 $[\mathrm{m/s^2}]$
Length scale parameter	l_{c}	0.625 [m]

4.4.1 Grounded glacier

For grounded glacier, we consider the rectangular domain with length $L = 500$ m and height $H = 125$ m under plane strain assumptions. As shown in Figure 4.5, the free slip boundary condition is enforced at the left and bottom edges of the domain (indicated by rollers). We also consider different seawater depths h_{w} at the terminus of grounded glaciers. In the case of marine-terminating grounded glacier (i.e., $h_{\mathrm{w}} > 0$), we apply a hydrostatic

load with hydraulic head h_w to the right edge of the domain as a depth-varying (triangularly) distributed load. To simulate the propagation of a single isolated surface crevasse in the glacier and compare the result with the LEFM model, we prescribe a rectangular pre-damaged zone ($D = 0.99$) with $4l_c$ in width and d_s^0 in depth. The horizontal distance between the left edge of the domain and the center of the pre-damaged zone is denoted by x_s^0.

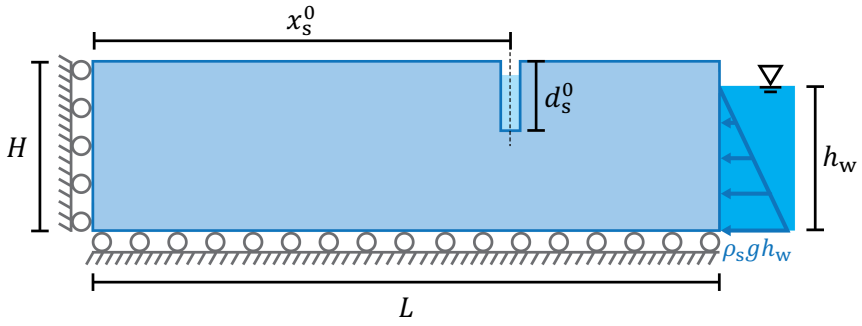

Figure 4.5: Schematic diagram of marine-terminating grounded glacier with free slip at the left edge and the base. A hydrostatic load with hydraulic head h_w is applied to the right edge of the domain as a depth-varying (triangularly) distributed load. A rectangular pre-damaged zone ($D = 0.99$) with width $4l_c$ and depth d_s^0 is defined to initiate the propagation of surface crevasse. The horizontal distance between the left edge of the domain and the center of the pre-damaged zone is denoted by x_s^0.

4.4.1.1 Stress state and crack driving force

We first evaluate the stress state in a pristine land-terminating glacier, that is, without a pre-damage zone and without seawater pressure acting at the right terminus (i.e., $h_w = 0$). As per the plane strain assumption, we have four components of the Cauchy stress tensor, including three normal stress components and one shear stress component in the x-z plane, which are plotted in Figure 4.6. We can see that the traction-free condition leads to non-uniformity in normal stress components at the terminus; whereas in the far-field region (away from the terminus) the three normal stress components vary linearly in the vertical (z) direction, but do not vary in the longitudinal (x) direction. On the other hand, the in-plane shear stress in the far-field region is negligibly small; whereas near the

terminus it show some non-uniformity and stress concentration. Furthermore, the far-field longitudinal stress σ_{xx} is positive (i.e. tensile) near the top surface and linearly changes to negative (i.e. compressive) with depth. Because most crevasses are mode I (opening) vertical fractures driven by tensile stress, they cannot propagate beyond a certain depth where the longitudinal stress becomes zero. Also, due to the self-gravitational load of glaciers, the far-field vertical stress σ_{yy} is always compressive (i.e. negative).

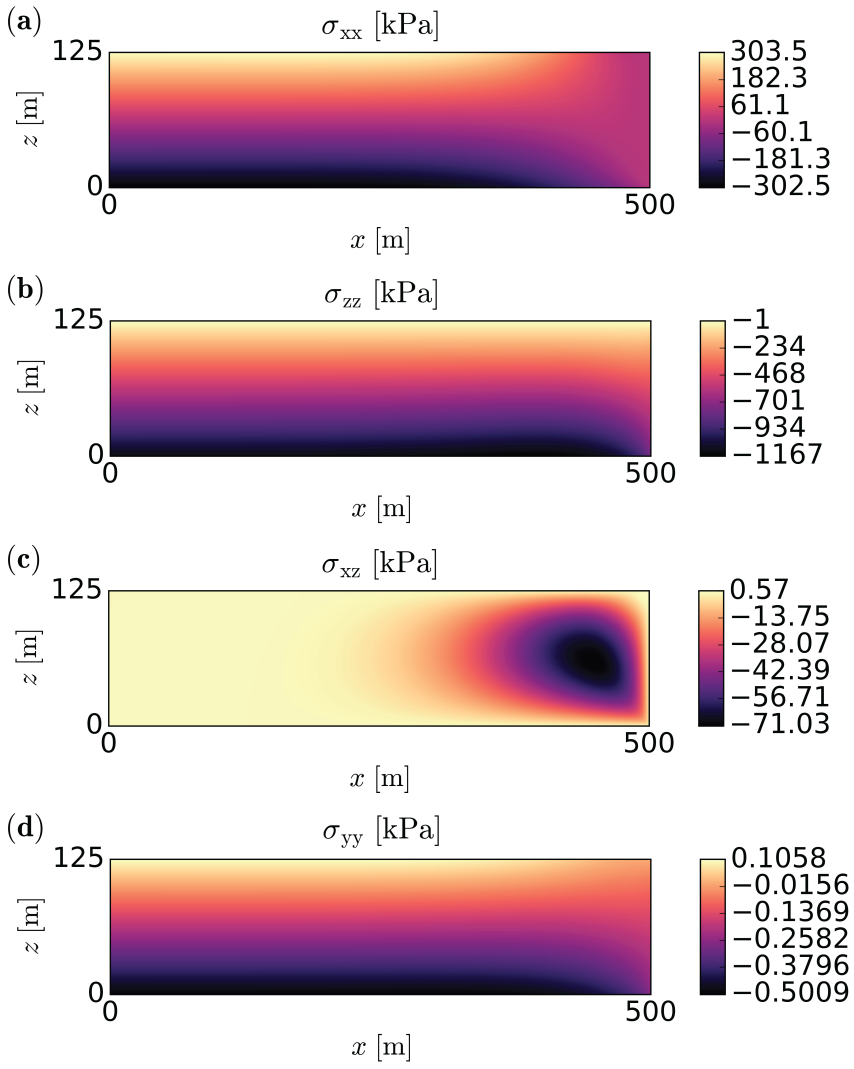

Figure 4.6: Stress state of intact land-terminating glaciers under plane strain assumptions using the finite element method (FEM): (a) σ_{xx}: normal stress in x-direction; (b) σ_{zz}: normal stress in z-direction; (c) σ_{xz}: shear stress in x-z plane; (d) σ_{yy}: normal stress in out-of-plane direction.

We next calculate the crack driving force in the pristine land-terminating glacier using

the three strain energy decomposition schemes described in Section 4.2.1. As shown in Figure 4.7(a), the maximum crack driving force calculated using Miehe's scheme occurs at the base of the near-terminus region. The maximum crack driving force computed from Zhang's scheme is at the top surface of the far-field region, as shown in Figure 4.7(b). However, with Zhang's scheme we notice that the crack driving force at the base of the near-terminus region is relatively larger than that at the surrounding area. Furthermore, the disparity in the magnitudes of crack driving forces computed from Miehe and Zhang schemes is quite significant. Regardless of the differences, the major concern is that both Miehe's and Zhang's schemes lead to finite crack driving force in regions where longitudinal normal stress σ_{xx} is negative. Consequently, the PFMs proposed by Miehe et al. [95] and Zhang et al. [177] predict fracture in the highly compressive regions of the glacier. This contradicts the results of the linear elastic fracture mechanics model for mode I fracture and violates the condition that damage should only evolve on in the tensile regions.

To further clarify the issue with Miehe's and Zhang's schemes, we calculate the in-plane strain components of the land-terminating glacier. As shown in Figure 4.8(a), the longitudinal strain ε_{xx} is positive almost everywhere; whereas the longitudinal stress σ_{xx} becomes negative with depth in the far-field region, as shown in Figure 4.6(b). Because the vertical strain ε_{zz} must be negative everywhere due to the self-gravitational load, the longitudinal strain must be positive everywhere due to the Poisson's ratio effect. According to Equations (4.12) and (4.14), the history field variable is dictated by the trace of $\langle\varepsilon\rangle^2$. Because the longitudinal strain is positive everywhere, the trace of $\langle\varepsilon\rangle^2$ and consequently the crack driving force are positive in Miehe's and Zhang's schemes, even in the regions where the longitudinal stress σ_{xx} is compressive. To ensure the compressive longitudinal stress does not contribute to mode I fracture, Lo et al. [86] introduced a modified scheme based on formulations for masonry-like materials. As shown in Figure 4.7(c), the crack driving force obtained from this modified scheme is zero for all regions where the longitudinal stress is negative, and reaches to the maximum at the surface of the far-field region.

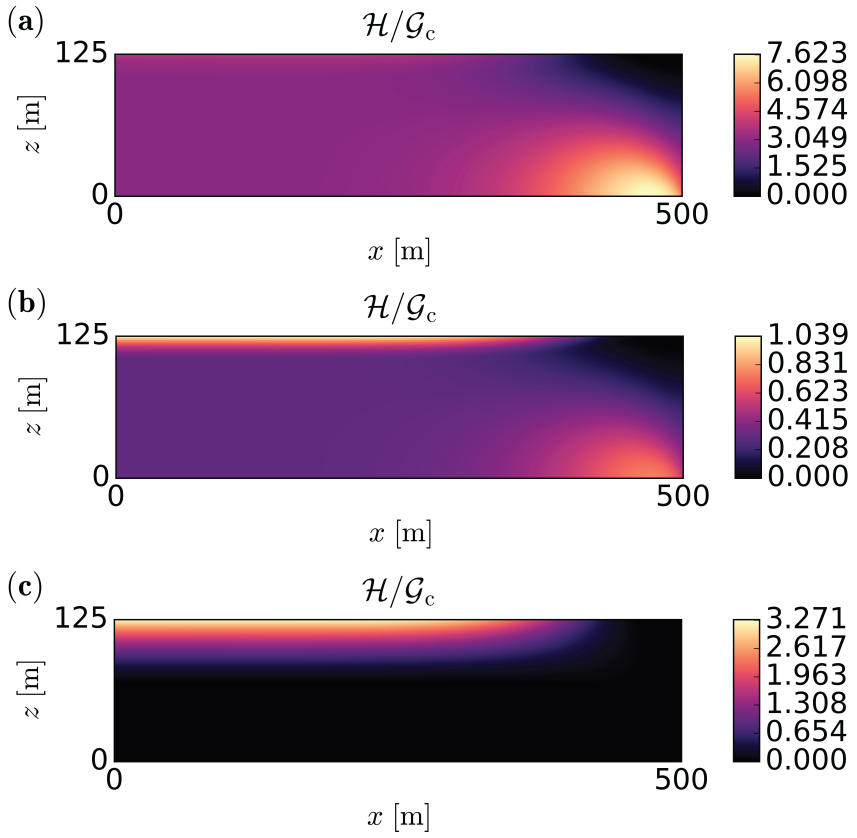

Figure 4.7: Crack driving force of intact land-terminating glaciers $\mathscr{H}/\mathscr{G}_c$ using three different strain energy decomposition schemes proposed by: (a) Miehe et al. [95]; (b) Zhang et al. [177]; (c) Lo et al. [86].

Thus, only the Lo's scheme leads to description of mode I fracture that is consistent with the LEFM model for self-gravitating geological media.

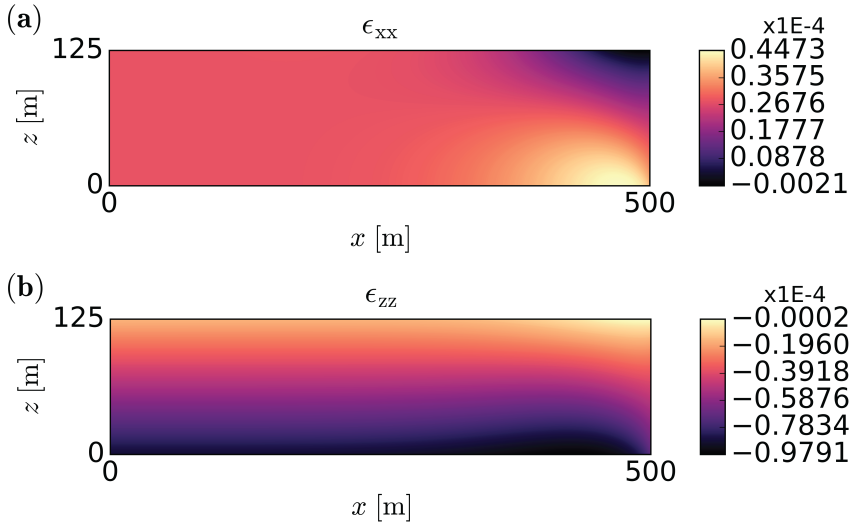

Figure 4.8: Normal strains of pristine land-terminating glaciers under plane strain assumptions: (a) ε_{xx} and (b) ε_{zz}.

4.4.1.2 Damage evolution with different schemes

We study the evolution of damage field corresponding to an air-filled surface crevasse in a land-terminating glacier using the PFM based on the Miehe's, Zhang's and Lo's schemes. We define the pre-damaged zone at $x_s^0 = 250$ m with depth $d_s^0 = 0.08H = 10$ m, and then compute the phase-field damage variable using three different schemes at the pseudo time step $n = 100$. The length scale parameter is taken as $l_c = 0.625$ m. According to Hillerborg et al. [63], l_c is indicative of the size of the fracture/damage process zone ahead of the crack tip and can be related to the cohesive strength σ_c as

$$l_c \approx \frac{E\mathscr{G}_{cI}}{\sigma_c^2} = \frac{(1-\nu^2)K_{cI}^2}{\sigma_c^2}, \tag{4.32}$$

where K_{cI} is the critical stress intensity factor (SIF) for mode I fracture. For glacier ice, the value of K_{cI} is taken as 0.1 MPa$\sqrt{\text{m}}$ [69]. Thus, the cohesive strength corresponding to $l_c = 0.625$ m is 0.1185 MPa. The damage fields of grounded glaciers predicted by

Miehe's and Zhang's schemes are plotted in Figure 4.9(a) and (b), respectively. These two figures indicate the nucleation and propagation of damage (indicative of surface crevasses) with the final damage $D \approx 1$ everywhere in the glacier domain, which is neither realistic nor consistent with LEFM. In contrast, the results from the Lo's scheme in Figure 4.9(c) show the localization of damage with a crack-like feature propagating to a final depth $d_{\mathrm{s}} = 0.955H$, which is consistent with the LEFM model result.

In Figure 4.9(c), we also notice that a second crack-like feature nucleates and propagates near the left edge of the domain. The left crack seems to develop as the central crack ceases to propagate, illustrating the ability of the PFM to capture crevasse initiation. Thus, the PFM can be an indispensable approach for understanding the fracture mechanics of closely-spaced glacier crevasses that are widely observed [38]. However, in this study our aim is to verify the PFM with the LEFM model by comparing the predicted maximum (or final) depth of isolated crevasses, and examine the conditions that enable the full-depth penetration of the isolated surface crevasse under different boundary conditions. Therefore, to promote the localized propagation of a single surface crevasse at the pre-damaged zone (i.e. $x_s^0 = 250$ m) and prevent the initiation of new surface crevasses, we decrease l_c to 0.1 m. This has the effect of increasing the cohesive strength σ_{c} to 0.2962 MPa such that damage evolution only occurs at pre-damaged zone due to the local stress concentration. Figure 4.9(d) shows the final damage field with Lo's scheme with $l_{\mathrm{c}} = 0.1$ m at the pseudo time step $n = 100$. The maximum penetration depth of this surface crevasse is predicted to be $d_{\mathrm{s}} = 0.949H$, which shows good agreement with the previous result $d_{\mathrm{s}} = 0.955H$ for $l_{\mathrm{c}} = 0.625$ m.

By comparing Figure 4.9(c) to (d), we find that the final damage field with smaller length scale is more localized and resembles an isolated surface crevasse. Because this corresponds to the assumption of larger cohesive strength of glacier ice, this suppresses the initiation of damage except near the pre-damaged zone. However, a significant drawback of decreasing l_c is the increased computational burden arising from the need to resolve the

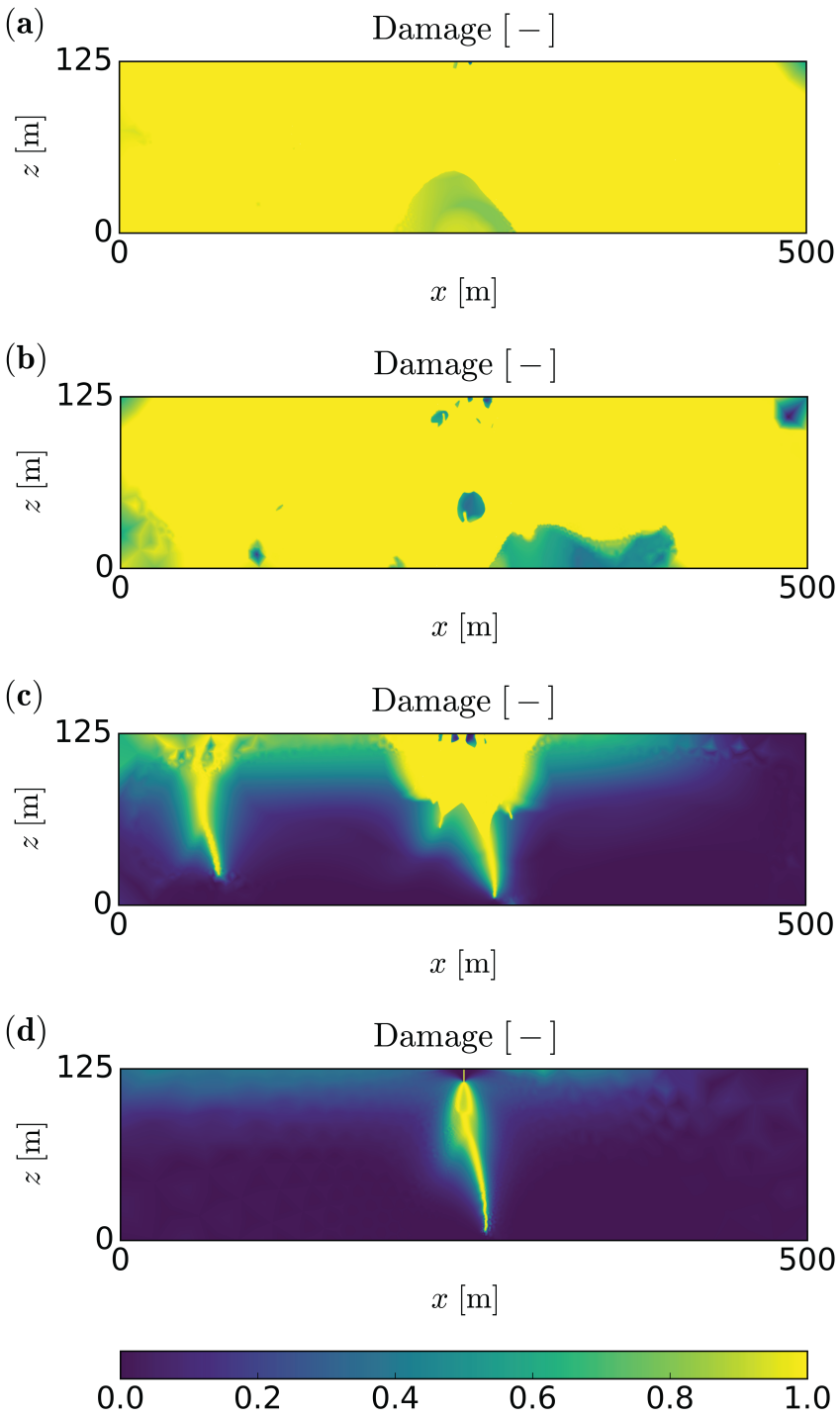

Figure 4.9: Predicted damage fields at pseudo time step $n = 100$ using the phase field models based on decomposition schemes proposed by: (a) Miehe et al. [95] with $l_c = 0.625$ m; (b) Zhang et al. [177] with $l_c = 0.625$ m; (c) Lo et al. [86] with $l_c = 0.625$ m; (d) Lo et al. [86] with $l_c = 0.1$ m, for air-filled surface crevasse propagation on land-terminating glacier.

damage zone with an extremely fine mesh. For the sake of numerical accuracy of the PFM, it is customary that the finite element mesh size needs to be sufficiently smaller than the chosen length scale. Consequently, defining $l_c = 0.1$ can be unnecessarily burdensome for evaluating the depth/height of glacier crevasses. Therefore, here we implement a somewhat *ad hoc* approach to localize the surface crevasse at the pre-damaged zone by assuming a threshold $\mathscr{F}^{\text{th}}$ for the crack driving force. Specifically, at each pseudo time step, we evaluate the crack driving force $\mathscr{H}/\mathscr{G}_c$ at each integration point using the Lo's scheme and set it to zero if $\mathscr{H}/\mathscr{G}_c \leq \mathscr{F}^{\text{th}}$. We take the value of this threshold as the maximum crack driving force calculated based on the stress state of pristine glacier for the specific boundary condition. The thresholds assumed for grounded glaciers with different seawater levels at terminus in this study are listed in Table 4.2. Note that for a near-floating grounded glacier (i.e., $h_w = 0.9H$), $\mathscr{F}^{\text{th}} = 0$ because the compressive seawater pressure at the terminus nullifies the crack driving force in the far-field region of the glacier.

Table 4.2: Thresholds of crack driving force for grounded glaciers with different seawater level at terminus.

h_w/H	0%	50%	90%
$\mathscr{F}^{\text{th}}$	3.271	0.754	0

4.4.1.3 Maximum surface crevasse depth

We next evaluate the maximum penetration depths of crevasses from the PFM and compare them with those predicted by the LEFM model. In Figure 4.10(a) shows the final damage field corresponding to an air-filled surface crevasse in a land-terminating glacier, which looks like an inverted teardrop with the maximum penetration depth $d_s = 0.953H$. The application of threshold $\mathscr{F}^{\text{th}} = 3.271$ (refer to Table 4.2) localizes the propagation of the crevasse near the assumed pre-damaged region. To test the sensitivity of the predicted maximum depth to the threshold value, we increase the threshold by ten times (i.e. $\mathscr{F}^{\text{th}} = 32.71$) and re-run the simulation. As shown in Figure 4.10(b), the width of

the damaged zone decreases significantly, but the predicted maximum depth remains at $d_s = 0.953H$, demonstrating the lack of sensitivity.

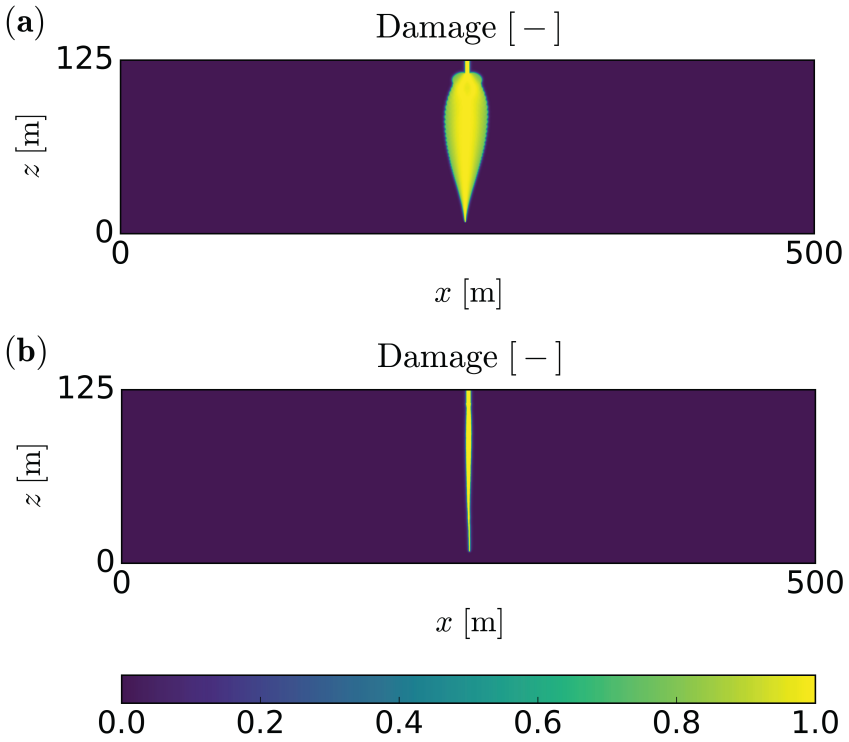

Figure 4.10: Final damage fields predicted by PFM using the Lo's scheme for an air-filled surface crevasse (i.e., $h_s = 0$) in a land-terminating glacier with threshold: (a) $\mathscr{F} = 3.271$; (b) $\mathscr{F}^{\text{th}} = 32.71$. The predicted maximum crevasse depth is insensitive to the assumed value of the threshold.

We next check the efficacy of the threshold to localize a partially water-filled (i.e., $h_s = 0.375d_s$) surface crevasse in a marine-terminating glacier with seawater level $h_w = 0.5H$ at the terminus. As shown in Figure 4.11(a), without the assumption of threshold (i.e. $\mathscr{F}^{\text{th}} = 0$), the pre-defined damaged zone propagates to $d_s = 0.655H$, but two surface crevasses nucleate and propagate on both sides of the original crevasse. By taking the threshold $\mathscr{F}^{\text{th}} = 0.754$, a single surface crevasse can be effectively localized at the pre-defined damage zone, as demonstrated by Figure 4.11(b). The maximum depth of the single surface crevasse $d_s = 0.655H$, which is the same as that obtained without the threshold. Furthermore, increasing the threshold to $\mathscr{F}^{\text{th}} = 7.54$ (i.e tenfold increase) we obtain the maximum penetration depth $d_s = 0.654H$, illustrating the lack of sensitivity. The above

two studies show that the thresholds values listed in Table 4.2 allow the propagation of a single isolated crevasse without affecting the prediction of maximum crevasse depths. Increasing the threshold value only decreases the width of the damaged zone resulting a sharp crack-like feature.

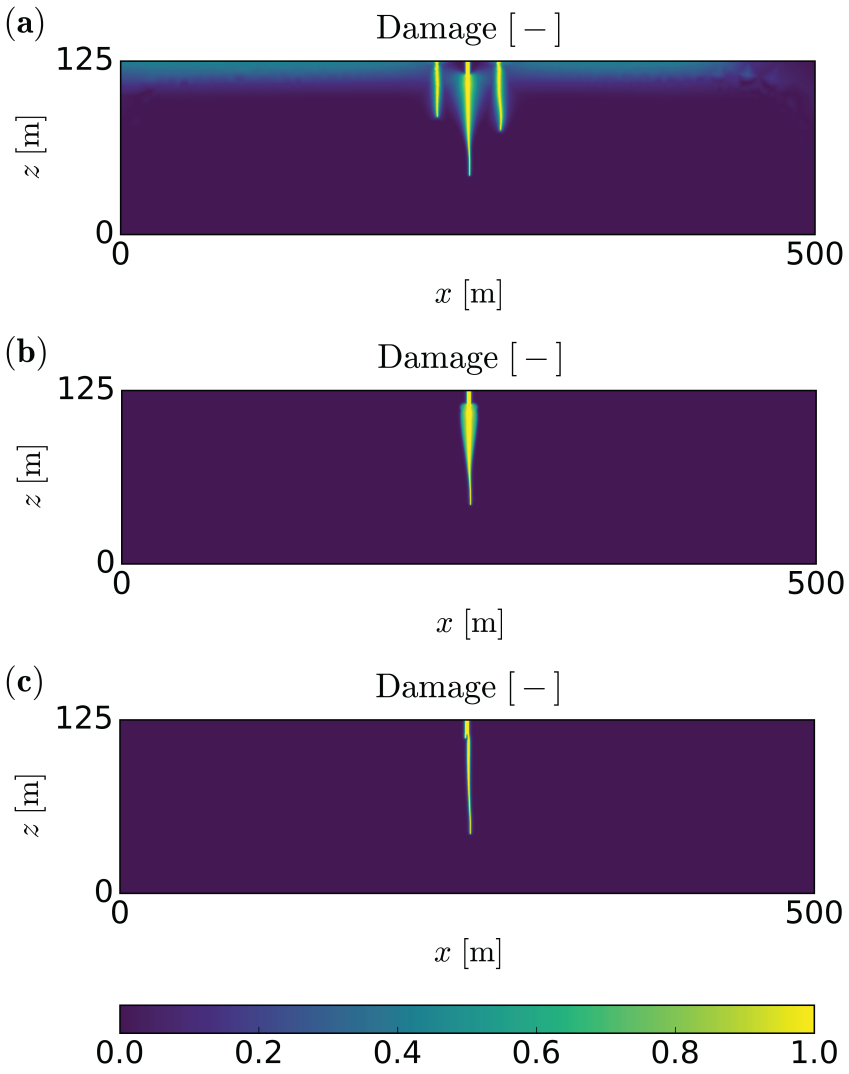

Figure 4.11: Final damage fields predicted by PFM using the Lo's scheme for a partially water-filled surface crevasse (i.e., $h_s = 0.375 d_s$) in a marine-terminating glacier with sea-water level $h_w = 0.5H$ and threshold: (a) $\mathscr{F} = 0$; (b) $\mathscr{F}^{th} = 0.754$; (c) $\mathscr{F}^{th} = 7.54$. The predicted maximum crevasse depth is insensitive to the assumed value of the threshold.

4.4.1.4 Comparison with the LEFM model

Figure 4.12 shows the normalized final crevasse depths d_s/H for isolated surface crevasses filled with freshwater to different levels, $h_s/d_s = \{0,\ 12.5,\ 25,\ 37.5,\ 50,\ 62.5,\ 75,\ 87.5,\ 100\}\%$, within grounded glaciers terminating at the ocean with varying sea levels, $h_w/H = \{0,\ 50,\ 90\}\%$. As before, surface crevasses are initiated by a pre-damaged zone at $x_s^0 = 250$ m with depth $d_s^0 = 0.08H = 10$ m. Because we are only interested in predicting the crevasse depth, all the PFM simulations we use the Lo's scheme with the threshold applied to calculate crack driving force and $l_c = 0.625$ m. The LEFM model results are obtained using the symmetric double edge-cracked plate weight functions as detailed in Appendix I. From Figure 4.12, it is evident that the PFM results are in excellent agreement with those from the LEFM model for all cases. In the scenario of land-terminating glaciers (i.e., $h_w = 0$), ice slabs are extremely vulnerable because there is no compressive seawater pressure acting on the terminus to restrict the glacier flow. In this case, an air-filled surface crevasse can propagate to 95.5% of the thickness of glacier. As the seawater level at terminus is increased, the propagation of surface crevasses requires the presence of melt water to enable hydrofracture. For example, a surface crevasse in a marine-terminating grounded glacier with seawater level $h_w/H = 50\%$ can propagate to 65% of the glacier thickness if it is partially filled with meltwater ($h_s = 0.375 d_s$). The same crevasse if filled with more melt water ($h_s/d_s \geq 50\%$) can penetrate the entire thickness of the marine-terminating glacier, leading to iceberg calving. However, in a grounded marine-terminating glacier that is near-floatation (i.e., $h_w/H \approx 90\%$), the propagation of surface crevasse is arrested even if there is enough meltwater to fully-fill the crevasse.

The above study leads us to the conclusion that an isolated surface crevasse in a near-floating glacier cannot propagate and cause iceberg calving. However, this result is dependent on the assumption of pre-damaged zone size. To illustrate this further, in Figure 4.13(a) we plot the net mode I SIF K_I^{net} at the tip of the surface crevasse with depth d_s for three different meltwater levels within the crevasses, $h_s/d_s = \{87.5,\ 93.75,\ 100\}\%$. We

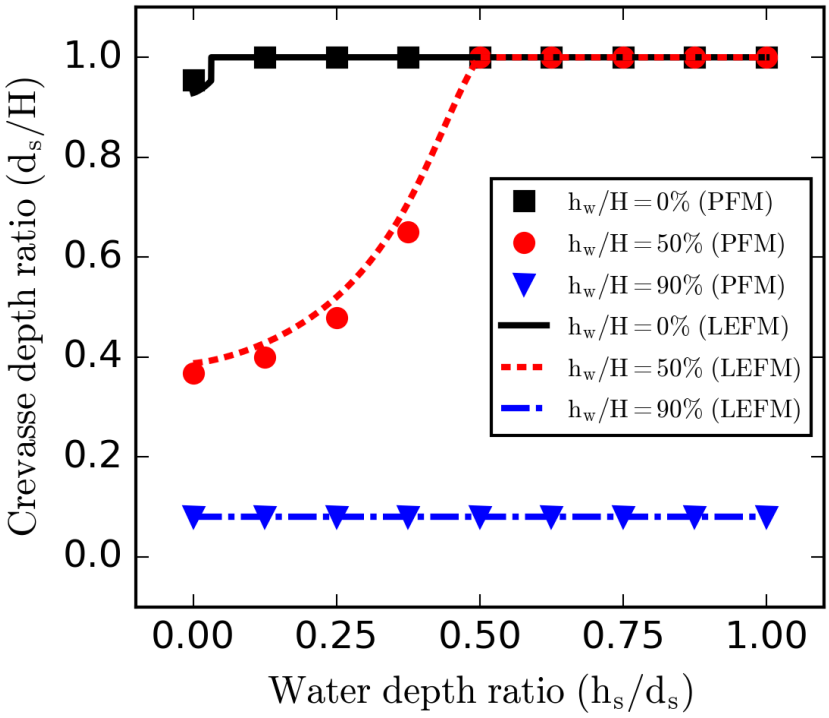

Figure 4.12: Surface crevasse depth d_s normalized with the domain height $H = 125$ m for varying freshwater levels h_s filling the surface crevasse within grounded glaciers. The solid and dashed lines depict the 'double edge cracks' LEFM model result for different seawater depths h_w at the terminus. The markers (i.e. black squares, red dots, and blue triangles) represent phase field method (PFM) results based on strain energy decomposition scheme proposed by Lo et al. [86] with threshold $\mathscr{F}^{\text{th}}$ applied.

find that the surface crevasse filled with meltwater up to 87.5% of the crevasse depth cannot propagate because the SIF is always negative (see blue solid line in Figure 4.13(a)). However, if we assume the crevasse filled with more freshwater, we find that the SIFs change from negative to positive along with the increase of normalized crevasse depth ratio d_s/H. That means a sufficiently deep pre-crack can penetrate through the full depth of a near-floatation grounded glacier. The pre-crack depths that can lead to the calving of near-floatation glaciers are estimated to be $0.68H$ and $0.52H$ for the crevasses filled with freshwater in levels of $h_s/d_s = 93.75\%$ and 100%, respectively. We also conduct phase field studies to validate the influence of pre-crack depth on near-floatation glaciers calving. As shown in Figure 4.13(b), we consider four different depths of the pre-defined damaged zone, $d_s^0/H = \{8, 40, 50, 70\}\%$. When the crevasse is fully filled with freshwater (i.e., $h_s/d_s = 100\%$), a pre-crack with $0.5H$ in depth can cause glacier calving; whereas, for water level inside the crevasse as $0.9375d_s$, calving can occur only if a deeper pre-crack with $0.7H$ in depth exists. Therefore, PFM results are consistent with LEFM predictions for understanding the effect of pre-crack length on near-floatation glaciers calving. However, note that such deep crevasses are unlikely to pre-exist in reality, which means calving of near-floatation glaciers may only occur in extreme scenarios.

4.4.2 Floating ice shelves

As a marine-terminating glacier enters the ocean it gradually goes from grounded to floating, thus forming an ice shelf. By definition an ice shelf is a floating glacier, which typically are several kilometers long. Here we consider a rectangular domain with length $L = 5000$ m and height $H = 125$ m under plane strain assumptions. As shown in Figure 4.14, the free slip boundary condition is enforced at the left edge of the domain (indicated by rollers) and buoyant force is applied at the base of the domain (indicated by yellow arrows). The buoyancy pressure on the ice shelf base is enforced as a Robin/mixed boundary

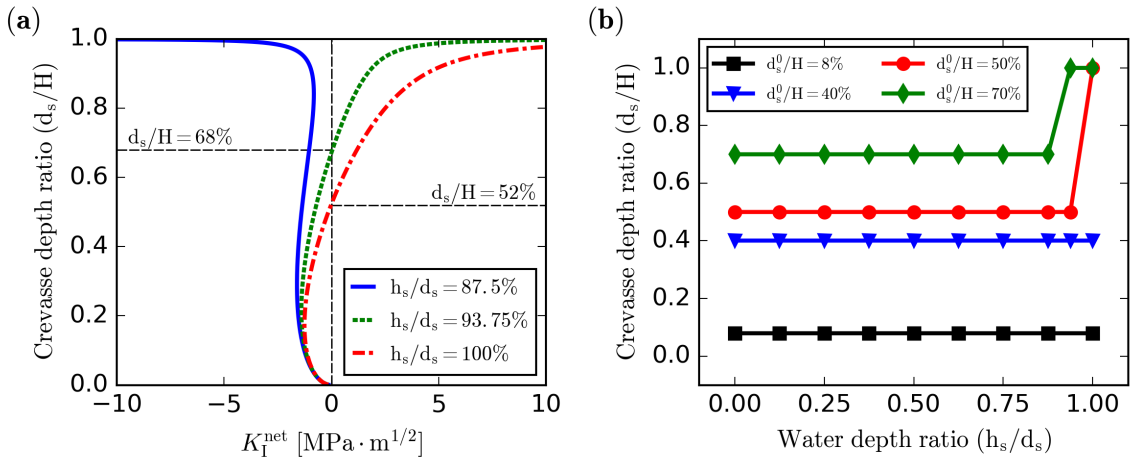

Figure 4.13: (a) Mode I net stress intensity factor K_I^{net} computed at the tip of surface crevasses with depth d_s penetrating through a near-floatation grounded glacier with thickness $H = 125$ m using the 'double edge cracks' LEFM model. Surface crevasses are filled with freshwater to different levels $h_s/d_s = \{87.5, 93.75, 100\}\%$; (b) the maximum penetration depths d_s of surface crevasses with different pre-crack depths d_s^0 for varying freshwater levels h_s filling the surface crevasse predicted by phase field models.

condition given by

$$\boldsymbol{\sigma} \cdot \mathbf{n} = \begin{bmatrix} 0 & \rho_s g(h_w - u_z) \end{bmatrix}^T \text{ on } \partial\Omega_b, \tag{4.33}$$

where u_z is the vertical component of the displacement vector, and $\partial\Omega_b$ represents the base of the domain where buoyancy is applied. The seawater depth at the terminus is determined by the ratio of ice density to sea water density (i.e., $h_w/H = \rho_i/\rho_s \approx 90\%$). The seawater pressure with hydraulic head h_w is applied to the right edge of the domain as a depth-varying (triangularly) distributed load. As noted by Nick et al. [105], ice-shelf calving is associated with propagation of both surface and basal crevasses. Therefore, we consider the preset damaged zone not only on the surface of ice shelves but also at the base of the domain. This starter crevasse is still defined as a rectangular damaged zone ($D = 0.99$) with $4l_c$ in width. The initial depths for surface and basal crevasses are represented by d_s^0 and d_b^0, respectively. The horizontal distance between the left edge of the domain and the center of the starter crevasse on the surface and base of ice shelves are denoted by x_s^0 and x_b^0, respectively.

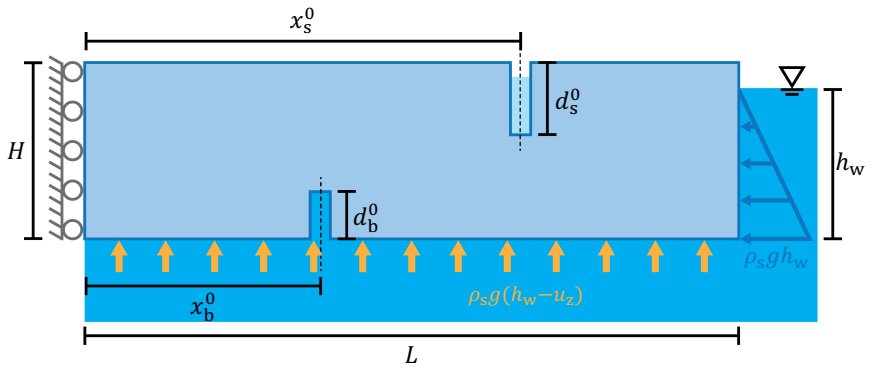

Figure 4.14: Schematic diagram of floating ice shelves with free slip at the left edge and buoyancy applied at the base. A hydrostatic load with hydraulic head $h_w = 90\%H$ is applied to the right edge of the domain as a depth-varying (triangularly) distributed load. A rectangular pre-damaged zone ($D = 0.99$) with width $4l_c$ is defined to initiate the propagation of surface and basal crevasses. The depths of pre-damaged zone on the surface and base of the ice shelves are denoted by d_s^0 and d_b^0, respectively. The horizontal distance between the left edge of the domain and the center of pre-damaged zones on the surface and base of ice shelves are denoted by x_s^0 and x_b^0, respectively.

4.4.2.1 Stress state and near-terminus edge effect

We first evaluate the stress state of a pristine floating ice shelf. In Figure 4.15, we plot the longitudinal normal stress σ_{xx} through the ice shelf thickness at four different locations $x = \{0, 2500, 4750, 4950\}$ m obtained using the FEM. We compare the FEM result with the analytical solution of σ_{xx} given by Equation (G.16), which is derived using the theory of elasticity along with the membrane stress assumption in Appendix G. At locations that are farther from the terminus (i.e., $x = 0$ and 2500 m), the longitudinal normal stress evaluated using the FEM are in good agreement with the analytical solution Equation (G.16). However, at locations that are nearer to the terminus (i.e., $x = 4750$ and 4950 m) we find that there is significant discrepancy between the longitudinal normal stresses evaluated using the FEM and the analytical solution. This indicates that the near-terminus edge effect on the longitudinal normal stress in a floating ice shelf is still significant at the location $x = 4750$ m, which is 250 m away from the terminus. In contrast, the near-terminus edge effect on the longitudinal normal stress in a grounded glacier becomes negligible at a

location that is 250 m away from the right edge of the domain, as shown in Figure 4.6(a). From Figure 4.15, we also find that the longitudinal stress σ_{xx} is tensile (positive) at the surface only near the terminus (i.e. $x = 4750$ and 4950 m), whereas it is compressive (negative) over the entire depth away from the terminus (i.e., $x = 0$ and 2500 m). Thus, the stress state in an ice shelf is different from that in a grounded glacier, owing to flexural (bending) deformation caused by the buoyancy condition at the basal surface and seawater pressure at the terminus.

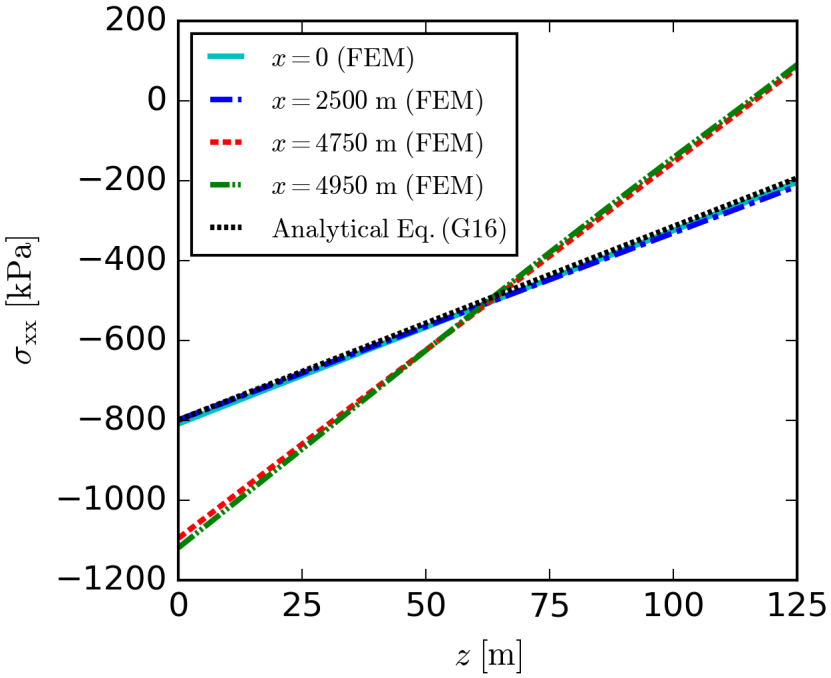

Figure 4.15: Comparison of the longitudinal normal stress σ_{xx} through the thickness of intact floating ice shelf at four different locations $x = \{0, 2500, 4750, 4950\}$ m obtained using the finite element method (FEM) with analytical solution Equation (G.16) based on the theory of compressible linear elasticity.

4.4.2.2 Surface crevasse propagation

We simulate surface crevasse propagation in a floating ice shelves to better understand the effects of near-terminus and far-field stress states. We initiate the localized propagation of isolated surface crevasses by a pre-crack with $d_s^0 = 0.08H = 10$ m in depth at three

different horizontal locations $x_s^0 = \{2500, 4750, 4950\}$ m. The levels of freshwater filling the surface crevasse are taken as $h_s/d_s = \{0, 12.5, 25, 37.5, 50, 62.5, 75, 87.5, 100\}\%$. Figure 4.16 shows the normalized final crevasse depths d_s/H for isolated surface crevasses within floating ice shelves obtained from both PFM and LEFM models. The PFM results are obtained using the Lo's scheme along with a threshold on the crack driving force. The LEFM model results are obtained using the single edge crack weight function described in Appendix I. To evaluate the near-terminus edge effect on crevasse propagation using the LEFM model, we use a linear approximation of the stress variation with depth at $x = 4750$ m and 4950 m in Figure 4.15 to calculate the SIFs. In the far-field, we use the analytical solution given by Equation (G.16) to calculate the SIFs. In Figure 4.16, we show the predicted final depths of surface crevasses initiated at different horizontal locations.

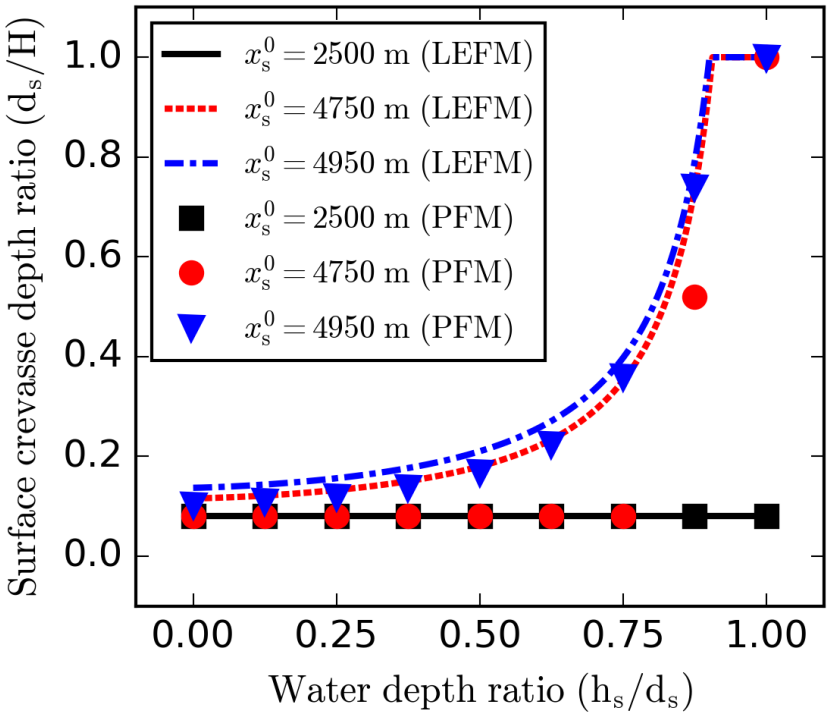

Figure 4.16: Surface crevasse depth d_s normalized with the domain height $H = 125$ m for varying freshwater levels h_s filling the surface crevasse within floating ice shelves. The solid and dashed line depict the 'single edge cracks' LEFM model result. The markers (i.e. black squares, red dots, and blue triangles) represent numerical results with pre-crevasse defined at three different locations using phase field method (PFM) based on strain energy decomposition scheme proposed by Lo et al. [86].

According to both PFM and LEFM models, the surface crevasse in the far-field region ($x = 2500$ m) cannot propagate no matter how much freshwater filled into it. However, ice-shelf calving can occur when fully water-filled crevasses (i.e., $h_s/d_s = 100\%$) are initiated in the near-terminus region ($x = 4750$ and 4950 m). This is due to the fact that the longitudinal normal stress on the surface of ice shelves is in tension for the near-terminus region while in compression for the far-field region. Furthermore, for surface crevasses filled with the same level of freshwater, the less the distance between the crevasse and the terminus, the deeper the crevasse can propagate to. Therefore, the surface crevasse can make floating ice shelves more vulnerable as the place where it is initiated getting closer to the terminus. In other words, ice-shelf calving is more likely to happen near the terminus. This could possibly explain the reason why the size of detached iceberg is much less than that of ice shelves. We do notice the quantitative discrepancy between PFM and LEFM results of the predicted final depths of near-terminus surface crevasses. Note that the weight function utilized here for the LEFM model is originally formulated for evaluating the SIF for a rectangular, finite-width plate with a single edge-crack subjected to far-field uniaxial normal stress. Therefore, it may not be completely applicable for predicting calving from floating ice shelves owing to differences in boundary conditions [69]. We shelve the quantitative discrepancy as for now because numerical predictions of crevasses depths obtained from both PFM and LEFM models yield the same qualitative analysis for the near-terminus edge effect on surface crevasse propagation.

4.4.2.3 Basal crevasse propagation

We next evaluate the near-terminus edge effect on propagation of basal crevasses within floating ice shelves. The propagation of isolated basal crevasses are also initiated by a pre-crack with $d_b^0 = 8\%H = 10$ m in depth at three different locations $x_b^0 = \{2500, 4750, 4950\}$ m. Because basal crevasses are hydrologically connected to the external seawater, the level of seawater filling basal crevasses will increase associated with crevasses propagation until

reaching to the seawater level at ice-shelf terminus h_w.

Figure 4.17(a) shows mode I net SIFs (K_I^{net}) computed at the tip of basal crevasses with depth d_b penetrating through a floating ice shelf using the single edge cracks LEFM model. The longitudinal normal stress of two near-terminus locations utilized to calculate SIFs are obtained from curve fitting as introduced in Section 4.4.2.2. For basal crevasse initiated at the far-field region ($x = 2500$ m), SIF computed at the crevasse tip is always positive so that the corresponding basal crevasse can penetrate the entire thickness of the ice shelf. The same prediction is provided by LEFM models for basal crevasse initiated at the location 250 m away from the terminus (see red dashed line in Figure 4.17(a)). However, for the basal crevasse initiated at $x_b^0 = 4950$ m, the SIF changes from positive to negative when the normalized basal crevasse depth increases to $d_b/H = 88\%$. Therefore, the basal crevasse at the location 50 m away from the terminus will stop propagating when its depth reaching to $88\%H$. Figure 4.17(b) shows pseudo time history of basal crevasses propagation from three different locations of floating ice shelves using PFM. For the far-field basal crevasse, both PFM and LEFM models provide the same prediction of its final depth, which equals to the entire thickness of the floating ice shelf. Furthermore, the near-terminus basal crevasse can propagate to $79.8\%H$ if initiated at $x_b^0 = 4750$ m according to PFM results; whereas, no propagation occurs if the basal crevasse is initiated closer to the terminus at $x_b^0 = 4950$ m. Despite the discrepancy of predicting near-terminus basal crevasses depths using PFM and LEFM models, the underlying edge effect of the terminus on basal crevasses propagation is consistent: the propagation of basal crevasses is suppressed as its nucleating location getting closer to the terminus.

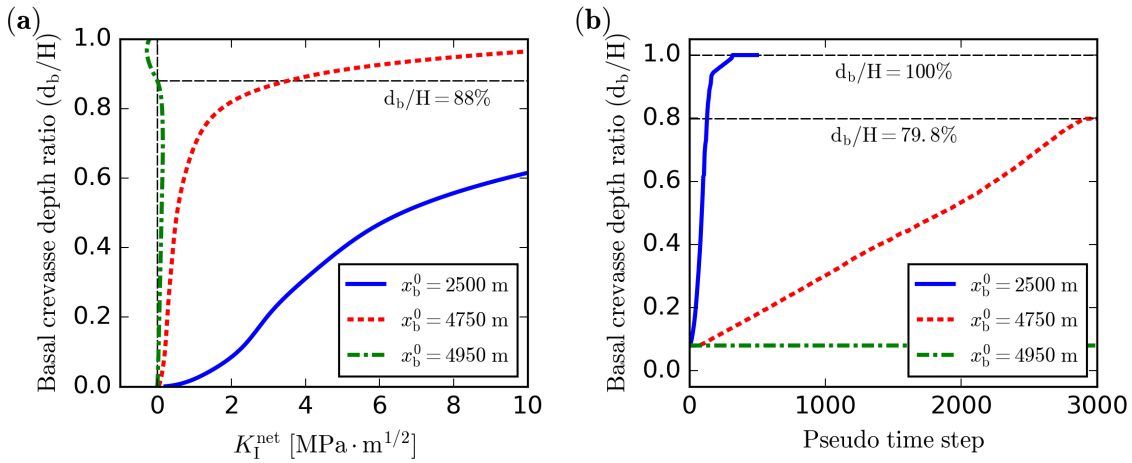

Figure 4.17: (a) Mode I net stress intensity factor K_I^{net} computed at the tip of basal crevasses with depth d_b penetrating through a floating ice shelf with thickness $H = 125$ m using the 'single edge cracks' LEFM model at three different locations $x_b^0 = \{2500, 4750, 4950\}$ m; (b) pseudo time history of basal crevasses propagation within floating ice shelves at three different locations $x_b^0 = \{2500, 4750, 4950\}$ m.

4.5 Conclusions

In this chapter, we present a phase-field poro-damage model for hydrofracturing and use it to simulate the propagation of water-filled crevasses in glaciers and ice shelves. The displacement and damage fields are solved in a staggered manner using the standard finite element method in the open-source software FEniCS. Three elastic strain energy decomposition schemes are implemented to calculate the crack driving force (history field variable), which are proposed by Miehe et al. [95], Zhang et al. [177], and Lo et al. [86], respectively. The maximum penetration depths of crevasses in grounded glaciers and floating ice shelves are evaluated using the proposed phase field model (PFM), and then compared to the corresponding predictions based on linear elastic fracture mechanics (LEFM) models. The results of our study reveal several important findings as follows:

1. The crack driving force calculated using schemes proposed by Miehe et al. [95] and Zhang et al. [177] predicts damage accumulation in regions where the longitudinal normal stress is in compression. This is contrary to LEFM and violates the tension-compression asymmetry of damage evolution normally assumed for brittle materials;

2. Strain energy decomposition scheme modified by Lo et al. [86] nullifies positive crack driving force in regions where the longitudinal stress is negative thus leading to an accurate description of fracture, especially in geological media that subjected to self-gravitational load;

3. For land- and marine-terminating grounded glaciers, applying a sufficiently large threshold on crack driving force calculated using Lo's scheme is an efficient *ad hoc* approach to effectively localize the propagation of preset crevasses without significantly affecting the prediction of final crevasses depths;

4. The maximum penetration depths of water-filled surface crevasses within grounded glaciers predicted using PFM are in good agreement with those evaluated based on

double edge crack LEFM models;

5. For floating ice shelves, there exists near-terminus edge effect on water-filled crevasses propagation according to both PFM and LEFM results: growth of surface crevasses will be promoted while that of basal crevasses will be suppressed as nucleated locations of crevasses approaching to the terminus.

In conclusion, the phase-field poro-damage model based on the strain energy decomposition scheme proposed by Lo et al. [86] can effectively simulate glacier crevasses propagation resulting from hydrofracture and self-gravitational load. Useful insights into the near-terminus edge effect of floating ice shelves on crevasses propagation can be gained from this study. Compared to widely used LEFM models, the PFM model can describe the formation and propagation of crevasses in glaciers with more complex geometries and boundary conditions. However, the current PFM model is based on the assumption of ice compressibility, which is contrary to observations reported from field experiments on glaciers [39]. Furthermore, glacier ice is generally considered as visco-elastic/plastic material, but the PFM is not well established for such materials despite some recent attempts [174]. Therefore, our future work will focus on extending the current poro-damage phase-field formulation to make it applicable for different rheology.

Chapter 5

CONCLUSIONS

This dissertation presented novel decoupled approaches to model the corrosive dissolution of iron alloys and hydraulic fracture in glaciers, and discusses their implementation using the standard finite element method (FEM). Simulation studies, including verification and validation studies, were conducted to establish the flexibility, efficiency, and accuracy of the decoupled FEM and address specific science questions in the areas of corrosion and glaciology, which shows the broader applicability of the decoupled method.

In Chapter 2, we proposed a sequential non-iterative approach (SNIA) to model the multi-ionic species reactive transport in the liquid (electrolyte) phase during localized corrosion. We used the concept of total solute concentration to de-couple the governing equations of electro-diffusive mass transport from homogeneous equilibrium chemical reactions, leading to a two-step staggered numerical solution strategy. We compared and validated the accuracy and robustness of the SNIA by conducting two sets of simulations studies focusing on corrosion of carbon steel and Fe-Cr binary alloys within 1D cavity and 2D crevice. Specifically, we conducted studies evaluating the error (relative to Sharland's approach) in resolving ionic concentrations and corrosion current densities as a function of the time increment size. Figure 2.4 indicates that an appropriate size of time increment chosen based on the characteristic diffusion time scale of the corrosion system will ensure sufficient numerical accuracy of the SNIA. We also demonstrated the robustness of the SNIA by varying the values of electrochemical and crevice geometry parameters. For the larger metal potential $\phi_{\mathrm{M}} = -0.1$ V (see Figure 2.8), the one-step coupled formulation (see Appendix B) encountered difficulty with numerical convergence; whereas, there were no convergence issues with the SNIA. Furthermore, the parametric study examining the variation of steady-state pH at the crevice mouth (see Figure 2.11) and total amount of

ferrous and chromium ions in relation to the chromium weight fraction (see Figure 2.12) during crevice corrosion of Fe-Cr binary alloys showed good agreement between results obtained from SNIA and the experimental data reported by Bogar and Fujii [22]. While the advantages of the SNIA are its robustness and flexibility, the disadvantage is reduced computational efficiency due to time increment size restrictions to ensure sufficient numerical accuracy.

In Chapter 3, we examined several critical electrochemical factors, including species concentrations, electrolyte pH and resistance, and electrical potential, for artificial pit experiments of 316L stainless steel wire using a multi-species reactive transport model. The pit stability products and critical electrical potential (E_{T} and E_{rp}) collected from experiments are applied to estimate the electrode current density and the elapsed time of the simulation. We considered two stages of simulation based on the change of the electrical current density during the artificial pit experiments: stable dissolution under a salt film and film-free dissolution that transitions to repassivation. In the first stage, a salt film exists and the pH near the corroding surface is within the range of 1.63 to 1.71, which is small enough to sustain the aggressive chemistry necessary for sustained or stable pit growth. The predicted specific resistance of the pit solution shows a good agreement with the experiment results. The effects of the temperature and the bulk concentration on pit electrochemical factors can be captured well using our model and are qualitatively consistent with existing experimental and numerical studies. In the second stage, the dilution of metal cation and the increase of pH near the corroding surface from the range of $1.63 \sim 1.71$ to that of $1.76 \sim 2.21$ are evident from the numerical results. The dilution of metal cation at the pit base is due to the transport of corresponding species and the decrease of the anodic current density. The critical surface concentration of metal cation is predicted to be in the range from 60% to 75% of saturation when repassivation occurs, assuming a current density at repassivation of 30 μA/cm^2. The pH increase at the pit base responsible for the onset of repassivation is a consequence of the contribution by the local cathodic reaction, which

was suppressed during the high-rate anodic dissolution in the first stage. The simulations conducted in this chapter are based on a more comprehensive multi-ionic reactive transport model, which provides a better description of species diffusion, electro-migration, and chemical reactions compared to existing numerical studies.

In Chapter 4, we presented a phase-field poro-damage model for hydrofracturing and used it to simulate the propagation of water-filled crevasses in glaciers and ice shelves. Specifically, the phase-field formulation for brittle fracture is extended by the addition of the fluid stored energy term into the total energy functional of glaciers. The displacement and damage fields are solved in a staggered manner using the standard finite element method in the open-source software FEniCS. Three elastic strain energy decomposition schemes are implemented to calculate the crack driving force (history field variable), which are proposed by Miehe et al. [95], Zhang et al. [177], and Lo et al. [86], respectively. Among these schemes, the one based on formulations for masonry-like materials proposed by Lo et al. [86] is validated to provide an accurate description of fracture in geological media that subjected to self-gravitational load. We further modified this scheme by applying thresholds on crack driving force to localize the propagation of isolated crevasses. The maximum penetration depths of surface crevasses within grounded glaciers predicted using PFM are in good agreement with those obtained from linear elastic fracture mechanics (LEFM) models. Useful insights into the near-terminus edge effect on crevasses propagation within floating ice shelves are gained from both PFM and LEFM models: growth of surface crevasses will be promoted while that of basal crevasses will be suppressed as nucleated locations of crevasses approaching to the terminus. While PFM shows broader applicability for describing the formation and propagation of crevasses in glaciers with more complex geometries and boundary conditions compared to LEFM models, the current PFM model is based on the assumption of ice compressibility, which is contrary to observations reported from field experiments on glaciers [39].

APPENDIX

Appendix A Proof of species mass balance

The chemical species in Ω_l can be classified into primary species and secondary species. Primary species refers to those produced from the oxidation of metallic electrode, while secondary species, which consists of the same metal element as the primary species, are products from homogeneous chemical reactions. For example, Fe^{2+} is one of the primary species considered in the localized corrosion of Fe-Cr binary alloys. Because $FeOH^+$ and $FeCl^+$ are products from homogeneous chemical reactions involving Fe^{2+}, they are the secondary species of Fe^{2+}. In this appendix, we illustrate that the concentration correction according to Equation (2.12) satisfies local mass balance of primary and corresponding secondary species. If we consider local mass balance of Fe^{2+}, then the total amount of Fe^{2+} together with $FeOH^+$ and $FeCl^+$ should be the same before and after the concentration correction. In general, the total local masses of primary and secondary species before ($\widetilde{M}$) and after (M) the concentration correction can be evaluated as

$$\begin{aligned} \widetilde{M} &= V_w \sum_{s=1}^{n} \tau_{ps} \widetilde{C}_s, \\ M &= V_w \sum_{s=1}^{n} \tau_{ps} C_s, \end{aligned} \tag{A.1}$$

where V_w [L] is the local volume of water and assumed to be constant, τ_{ps} [–] is the ratio of the stoichiometric coefficients of the primary species p to the secondary species s and $\tau_{pp} = 1$. Substituting Equation (2.12) into Equation (A.1), the difference between $\widetilde{M}$ and M is given by

$$M = V_w \sum_{s=1}^{n} \tau_{ps} \left(\widetilde{C}_s + \sum_{i=1}^{n_r} \omega_{is} \nu_{is} \widehat{C}_i \right) = \widetilde{M} + V_w \sum_{i=1}^{n_r} \sum_{s=1}^{n} \tau_{ps} \omega_{is} \nu_{is} \widehat{C}_i. \tag{A.2}$$

We now consider the i^{th} chemical reaction which consumes primary species p and pro-

duces secondary species s. From the law of conservation of mass, for substances containing the same metal element, the amount consumed and produced within the i^{th} reaction should be equal

$$-\tau_{pp}\omega_{ip}\nu_{ip} = \sum_{j\neq p}^{n} \tau_{pj}\omega_{ij}\nu_{ij}, \quad \Longrightarrow \quad \sum_{j=1}^{n} \tau_{pj}\omega_{ij}\nu_{ij} = 0. \tag{A.3}$$

Substituting Equation (A.3) into Equation (A.2), the last term in the right-hand side of Equation (A.2) becomes zero. Thus, the total local masses of primary and secondary species before and after the concentration correction are the same.

Appendix B Model formulation of Sharland and Tasker [131]

In Sharland's approach [131], reaction terms R_i can be eliminated by linear combination of the steady-state mass transport equations defined by

$$D_i \nabla^2 C_i + \frac{z_i D_i F}{R^* T} \nabla \cdot (C_i \nabla \phi) + R_i = 0. \tag{B.1}$$

Missing degrees of freedom can then be compensated by chemical equilibrium equation (2.11). For the Fe-NaCl electrochemical system described in Section 2.4.1.1, there are six ionic species taken into consideration: Fe^{2+}, $FeOH^+$, Na^+, Cl^-, H^+, and OH^-; these species are numbered in this order from $i = 1$ to 6 and denoted by the right subscript of variables. Then, the reaction term R_i in Equation (B.1) can be written as

$$\begin{aligned} R_1 &= -R_2 = -k_1(K_1 C_1 - C_2 C_5), \\ R_3 &= R_4 = 0, \\ R_5 &= k_1(K_1 C_1 - C_2 C_5) + k_2(K_2 - C_5 C_6), \\ R_6 &= k_2(K_2 - C_5 C_6). \end{aligned} \tag{B.2}$$

After rearrangement of equations (B.1) following Sharland's approach, the governing equations for this specific system includes the modified mass-transport equations, chemical equilibrium equations and LEN condition:

$$
\begin{cases}
D_1\nabla^2 C_1 + D_2\nabla^2 C_2 + \frac{F}{R^*T}\nabla\cdot\left[\left(z_1 D_1 C_1 + z_2 D_2 C_2\right)\nabla\phi\right] = 0, \\
D_1\nabla^2 C_1 + D_5\nabla^2 C_5 - D_6\nabla^2 C_6 + \frac{F}{R^*T}\nabla\cdot\left[\left(z_1 D_1 C_1 + z_5 D_5 C_5 - z_6 D_6 C_6\right)\nabla\phi\right] = 0, \\
D_3\nabla^2 C_3 + \frac{z_3 D_3 F}{R^*T}\nabla\cdot\left(C_3\nabla\phi\right) = 0, \\
D_4\nabla^2 C_4 + \frac{z_4 D_4 F}{R^*T}\nabla\cdot\left(C_4\nabla\phi\right) = 0, \\
C_2 C_5 - K_1 C_1 = 0, \\
C_5 C_6 - K_2 = 0, \\
\sum_{i=1}^{6} z_i C_i = 0.
\end{cases}
\tag{B.3}
$$

Then governing equations (B.3) are linearized using the Newton-Raphson method, discretized using the standard finite element method, and solved in FEniCS software. Element types and mesh are the same as we used for the implementation of the SNIA.

Table C.1: Pit stability products obtained from artificial pit experiments of type 300 stainless steel wire in the NaCl environment under different temperature as reported in [a] Srinivasan and Kelly [138]; [b] Katona et al. [75].

C_{bulk} [M]	25 °C	35 °C	45 °C	55 °C
0.6	0.90[a]	1.06[b]	1.10[b]	1.45[b]
1.0	0.75[b]	0.88[b]	1.00[b]	1.08[b]
3.0	0.54[b]	0.60[b]	0.70[b]	0.90[b]
5.5	0.20[b]	0.36[b]	0.40[b]	0.64[b]

Appendix D Diffusion coefficient

Table D.1: Reference values of species diffusion coefficients D_{ref} under room temperature 298.15 K.

Species	D_{ref} [10^{-9} m^2/s]	Reference	Species	D_{ref} [10^{-9} m^2/s]	Reference
H^+	9.31	[31]	OH^-	5.27	[31]
Na^+	1.33	[31]	Cl^-	2.03	[31]
Fe^{2+}	0.824	[57]	Cr^{3+}	0.824	[57]
Ni^{2+}	0.824	[57]	Mo^{3+}	0.824	[57]
$FeCl^+$	0.824	[57]	$FeCl_2$	0.008	–
$FeOH^+$	0.824	[57]	$Fe(OH)_2$	0.008	–
$CrCl^{2+}$	0.824	[57]	$CrCl_2{}^+$	0.824	[57]
$CrCl_3$	0.008	–	$CrOH^{2+}$	0.824	[57]
$Cr(OH)_2{}^+$	0.824	[57]	$Cr(OH)_3$	0.008	–
$NiCl^+$	0.824	[57]	$NiCl_2$	0.008	–
$NiOH^+$	0.824	[57]	$Ni(OH)_2$	0.008	–

Appendix E Temperature-pressure dependence of solution viscosity

Parameters ζ_{mn} calibrated from experiments [5] are listed in Table E.1, which are used for the calculation of coefficient a_i describing temperature-pressure dependence of solution viscosity as introduced in Equation (3.17). The solution viscosity under room temperature (298.15 K) and standard atmosphere can then be estimated in accordance with different concentrations, as shown in Figure E.1.

Table E.1: Parameters describing temperature-pressure dependence of solution viscosity calibrated from experiments [5].

ζ_{mn}	n	$m=0$	$m=1$
a_0	0	7.65306227×10^{-1}	–
	1	-1.78087723	-1.39287121×10^{-2}
	2	1.25374926	1.50838568×10^{-2}
	3	-1.61102861×10^{-1}	3.08379974×10^{-3}
	4	-7.27978696×10^{-2}	-5.27719410×10^{-3}
a_1	1	9.84225044×10^{-2}	2.22367778×10^{-2}
	2	2.43031313×10^{-1}	-3.68121974×10^{-2}
	3	-2.05007685×10^{-1}	1.57724556×10^{-2}
a_2	1	1.62231138×10^{-1}	-5.78612528×10^{-3}
	2	-2.91448434×10^{-1}	9.45954845×10^{-3}
	3	1.31605764×10^{-1}	-3.96672431×10^{-3}
a_3	1	-2.08142179×10^{-2}	5.49316850×10^{-4}
	2	3.80923122×10^{-2}	-9.01751419×10^{-4}
	3	-1.66477653×10^{-2}	3.77212002×10^{-4}

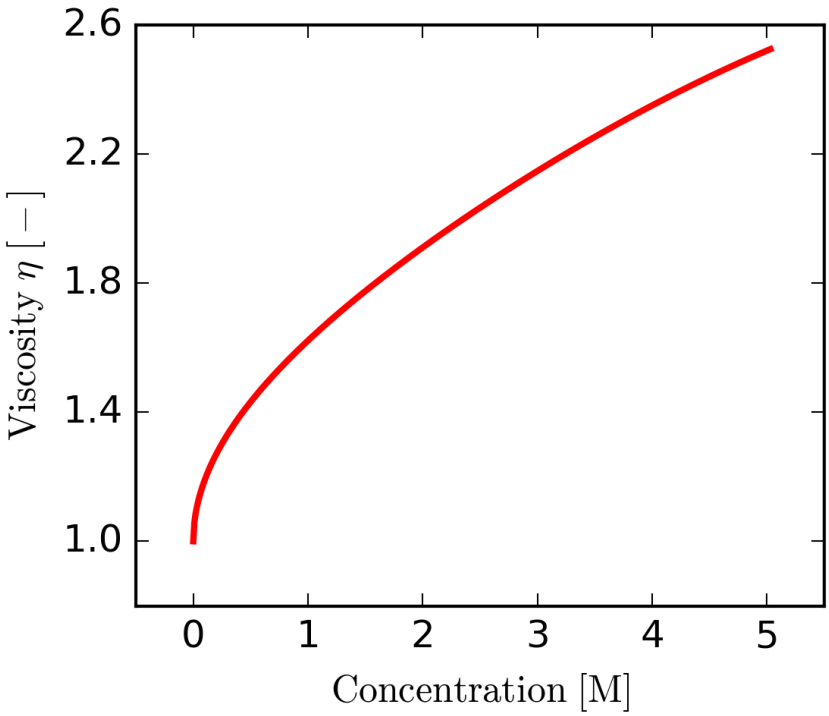

Figure E.1: Estimation of solution viscosity with respect to solution concentrations under room temperature (298.15 K) and standard atmosphere using Equation (3.17).

Appendix F Calculation of chemical reaction equilibrium constants

To better capture the temperature dependence of chemical reaction properties, we calculate the chemical reaction equilibrium constants K_r following the calibrated formulation obtained from the Thermoddem database [21]

$$\log_{10} K_r = b_0 + b_1 T + b_2 T^{-1} + b_3 \log_{10}(T) + b_4 T^{-2}, \tag{F.1}$$

where b_i are calibrated coefficients directly available from the database. We list b_i for the equilibrium constants calculation of all chemical reactions considered in this work as below.

Table F.1: Calibrated coefficients obtained from the Thermoddem database [21] for calculation of the chemical reaction equilibrium constants.

Chemical Reaction	b_0	b_1	b_2	b_3	b_4
$Fe^{2+} + Cl^- \rightleftharpoons FeCl^+$	808.65	0.1318	−45088.15	−294.24	2772595.80
$Fe^{2+} + 2Cl^- \rightleftharpoons FeCl_2$	1614.41	0.2611	−93454.00	−584.79	5352140.98
$Fe^{2+} + H_2O \rightleftharpoons FeOH^+ + H^+$	200.44	0.0301	−13947.78	−72.51	648026.46
$Fe^{2+} + 2H_2O \rightleftharpoons Fe(OH)_2 + 2H^+$	333.01	0.0508	−21902.65	−120.42	927522.20
$Cr^{3+} + Cl^- \rightleftharpoons CrCl^{2+}$	1135.49	0.1860	−62020.19	−413.21	3569091.70
$Cr^{3+} + 2Cl^- \rightleftharpoons CrCl_2{}^+$	1774.63	0.2887	−97135.39	−646.34	5661676.10
$Cr^{3+} + H_2O \rightleftharpoons CrOH^{2+} + H^+$	233.14	0.0362	−15165.61	−83.27	837406.70
$Cr^{3+} + 3H_2O \rightleftharpoons Cr(OH)_3 + 3H^+$	547.11	0.0791	−33332.58	−195.38	1349304.75
$Ni^{2+} + Cl^- \rightleftharpoons NiCl^+$	796.76	0.1293	−44201.34	−289.74	2667655.45
$Ni^{2+} + 2Cl^- \rightleftharpoons NiCl_2$	1567.32	0.2550	−90038.91	−568.86	5124711.71
$Ni^{2+} + H_2O \rightleftharpoons NiOH^+ + H^+$	236.97	0.0362	−16157.56	−86.36	945152.34
$Ni^{2+} + 2H_2O \rightleftharpoons Ni(OH)_2 + 2H^+$	329.16	0.0511	−21713.41	−118.92	979036.43
$H^+ + OH^- \rightleftharpoons H_2O$	701.95	0.1127	−36168.25	−253.60	2423273.05

Appendix G Derivation of the far-field longitudinal (horizontal) normal stress σ_{xx}

We consider a freely floating ice shelf (i.e., no tangential traction at the base) under plane strain assumptions, as depicted in Figure G.1(a). A body force with magnitude of $-\rho_i g$ in the z-direction is applied as the gravity loading. And a hydrostatic load with hydraulic head h_w is applied to the right terminus of the ice shelf as a depth-varying (triangularly) distributed load. Under such circumstance, we have the far-field equilibrium equations in three dimensions as given by

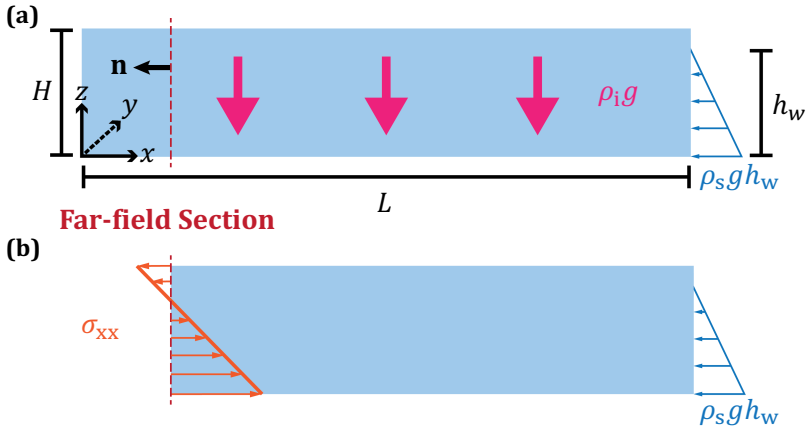

Figure G.1: (a) Schematic diagram of the floating ice shelf ($L \gg H$) with no tangential traction at the base. A body force with magnitude $-\rho_i g$ in the z-direction is applied as the gravity loading. And a hydrostatic load with hydraulic head h_w is applied to the right terminus of the ice shelf as a depth-varying (triangularly) distributed load. The out-of-plane direction is denoted by y; (b) Free body diagram of forces in x-direction applied on the far-field section of the ice shelf cut at the red dashed line with the surface normal vector denoted by $\boldsymbol{n}$.

$$\begin{cases} \frac{\partial \sigma_{xx}}{\partial x} + \frac{\partial \sigma_{xy}}{\partial y} + \frac{\partial \sigma_{xz}}{\partial z} = 0, \\ \frac{\partial \sigma_{xy}}{\partial x} + \frac{\partial \sigma_{yy}}{\partial y} + \frac{\partial \sigma_{yz}}{\partial z} = 0, \\ \frac{\partial \sigma_{zx}}{\partial x} + \frac{\partial \sigma_{zy}}{\partial y} + \frac{\partial \sigma_{zz}}{\partial z} + \rho_i g = 0. \end{cases} \tag{G.1}$$

We assume that far-field stresses are invariant with x-coordinate and out-of-plane stresses

are zero. We can now simplify Equation (G.1) as

$$\begin{cases} \frac{\partial \sigma_{xy}}{\partial y} = 0, \\ \frac{\partial \sigma_{yy}}{\partial y} = 0, \\ \frac{\partial \sigma_{zz}}{\partial z} + \rho_i g = 0. \end{cases} \tag{G.2}$$

At z-direction, we can solve the stress component σ_{zz} based on the feature of gravitational loading. The corresponding boundary conditions for Equation (G.2c) can be expressed as

$$\begin{cases} \sigma_{zz} = -\rho_i g H & \text{at } z = 0, \\ \sigma_{zz} = 0 & \text{at } z = H. \end{cases} \tag{G.3}$$

Therefore, the vertical normal stress σ_{zz} can be expressed as

$$\sigma_{zz}(z) = -\rho_i g (H - z). \tag{G.4}$$

Based on the theory of compressible linear elasticity, we have the constitutive relations as given by

$$\begin{cases} \varepsilon_{xx} = \frac{1}{E}\left[\sigma_{xx} - \nu\left(\sigma_{yy} + \sigma_{zz}\right)\right], \\ \varepsilon_{yy} = \frac{1}{E}\left[\sigma_{yy} - \nu\left(\sigma_{xx} + \sigma_{zz}\right)\right], \\ \varepsilon_{zz} = \frac{1}{E}\left[\sigma_{zz} - \nu\left(\sigma_{xx} + \sigma_{yy}\right)\right]. \end{cases} \tag{G.5}$$

Based on the plane strain assumption (i.e., $\varepsilon_{yy} = 0$), we can further simplify Equation (G.5b) as

$$\sigma_{yy} = \nu\left(\sigma_{xx} + \sigma_{zz}\right). \tag{G.6}$$

Upon substituting Equation (G.6) into Equation (G.5a), we have

$$\varepsilon_{xx} = \frac{1}{E}\left[\left(1 - \nu^2\right)\sigma_{xx} - \nu\left(1 + \nu\right)\sigma_{zz}\right]. \tag{G.7}$$

Furthermore, the length of typical ice shelves is at the level of kilometers, whereas its thickness is at the level of hundred meters. Therefore, we here adopt the membrance stress assumption based on the geometric feature of glaciers. The horizontal displacement is then assumed to be vertically invariant, which can be expressed as

$$\frac{\partial u}{\partial z} = \frac{\partial v}{\partial z} = 0 \implies \frac{\partial}{\partial x}\left(\frac{\partial u}{\partial z}\right) = 0. \tag{G.8}$$

The above partial derivative is interchangeable, we thus have

$$\frac{\partial}{\partial z}\left(\frac{\partial u}{\partial x}\right) = 0 \implies \frac{\partial \varepsilon_{\mathrm{xx}}}{\partial z} = 0, \tag{G.9}$$

which means the horizontal strain component is depth invariant. Upon taking derivative on both sides of Equation (G.7) with z and simplifying it based on Equation (G.9), we have

$$\frac{\partial \sigma_{\mathrm{xx}}}{\partial z} = \frac{\nu}{1-\nu}\frac{\partial \sigma_{\mathrm{zz}}}{\partial z}. \tag{G.10}$$

Combining Equations (G.10) and (G.2c), we have

$$\frac{\partial \sigma_{\mathrm{xx}}}{\partial z} = -\frac{\nu}{1-\nu}\rho_{\mathrm{i}} g. \tag{G.11}$$

We know that far-field stresses are invariant with x-coordinate and for the plane strain problem

$$\frac{\partial \sigma_{\mathrm{xx}}}{\partial y} = 0. \tag{G.12}$$

Therefore, the stress component σ_{xx} is only dependent on z-coordinate. Equation (G.11) can be integrated with respect to z as

$$\sigma_{\mathrm{xx}} = -\frac{\nu}{1-\nu}\rho_{\mathrm{i}} g z + C, \tag{G.13}$$

where C is an unknown constant. We next consider the force balance in x-direction based on the free body diagram of a far-field section of the floating ice shelf cut at the red dashed line, as shown in Figure G.1(b). The equilibrium equation in x-direction can be written as

$$\sum F_{\mathrm{x}} = \int_0^H \sigma_{\mathrm{xx}} \mathrm{d}z + F_{\mathrm{w}} = 0, \tag{G.14}$$

where $F_{\mathrm{w}} = \frac{1}{2}\rho_{\mathrm{s}} g h_{\mathrm{w}}^2$ is the resultant force caused by the hydrostatic load. Substituting Equation (G.13) into Equation (G.14), we have

$$C = \frac{\nu}{2(1-\nu)}\rho_{\mathrm{i}} g H - \frac{1}{2}\rho_{\mathrm{s}} g \frac{h_{\mathrm{w}}^2}{H}. \tag{G.15}$$

Combining Equations (G.13) and (G.15), we have the expression of far-field longitudinal normal stress through ice thickness as

$$\sigma_{\mathrm{xx}} = \frac{\nu}{1-\nu}\left[\frac{1}{2}\rho_{\mathrm{i}} g H - \rho_{\mathrm{i}} g\,(H-z)\right] - \frac{1}{2}\rho_{\mathrm{s}} g \frac{h_{\mathrm{w}}^2}{H}. \tag{G.16}$$

Appendix H Numerical verification study: single edge notched tension test

To verify our staggered implementation of the hybrid phase field model introduced in Section 4.2.1, we conduct a standard benchmark study of the single edge notched specimen subjected to tensile loading. As shown in Figure H.1, we consider a square plate containing a horizontal notch with a length of 0.5 mm located at mid-height of the left boundary. The specimen is pinned at the bottom and tensile loading is realized by a monotonic displacement u applied on the top boundary.

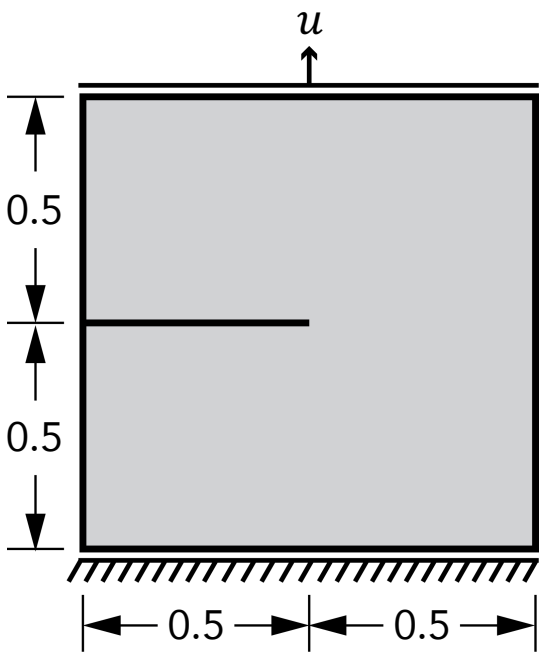

Figure H.1: Geometry and boundary conditions of a square single edge notched specimen subjected to tensile loading.

The parameters of material properties and phase field model are chosen to be the same as those used by Miehe et al. [95], as listed in Table H.1. We consider three different strain energy decomposition schemes proposed by Miehe et al. [95], Zhang et al. [177], and Lo et al. [86], respectively. Note that for Zhang's scheme, the critical strain energy release rate for mode I fracture $\mathscr{G}_{\mathrm{cI}}$ is taken as the same value of $\mathscr{G}_{\mathrm{c}}$ listed in Table H.1. The displacement control is applied with a constant increment $\Delta u = 10^{-5}$ mm in the first 500

time steps. After that, the displacement increment is adjusted to 10^{-6} mm owing to the rapid propagation of the crack.

Table H.1: Parameters of material properties and phase field modeling of single edged notch tension test [95].

Parameter	Value	Unit
λ	121.5	$\mathrm{kN/mm^2}$
μ	80.7	$\mathrm{kN/mm^2}$
$\mathscr{G}_\mathrm{c}$	2.7×10^{-3}	$\mathrm{kN/mm}$
l_c	0.015	mm
η	10^{-6}	$\mathrm{kN \cdot s/m^2}$

Figure H.2 shows three load-displacement curves obtained from phase field modeling based on corresponding strain energy decomposition schemes. The benchmark solution is plotted as black circular markers, which is digitized from Figure 9 of [10]. The results computed from our models using Miehe's and Lo's schemes are in good agreement with the benchmark solution; whereas, the discrepancy between the benchmark solution and the result obtained using Zhang's scheme is caused by the choice of critical strain energy release rate for mode II fracture $\mathscr{G}_\mathrm{cII} = 10\mathscr{G}_\mathrm{cI}$.

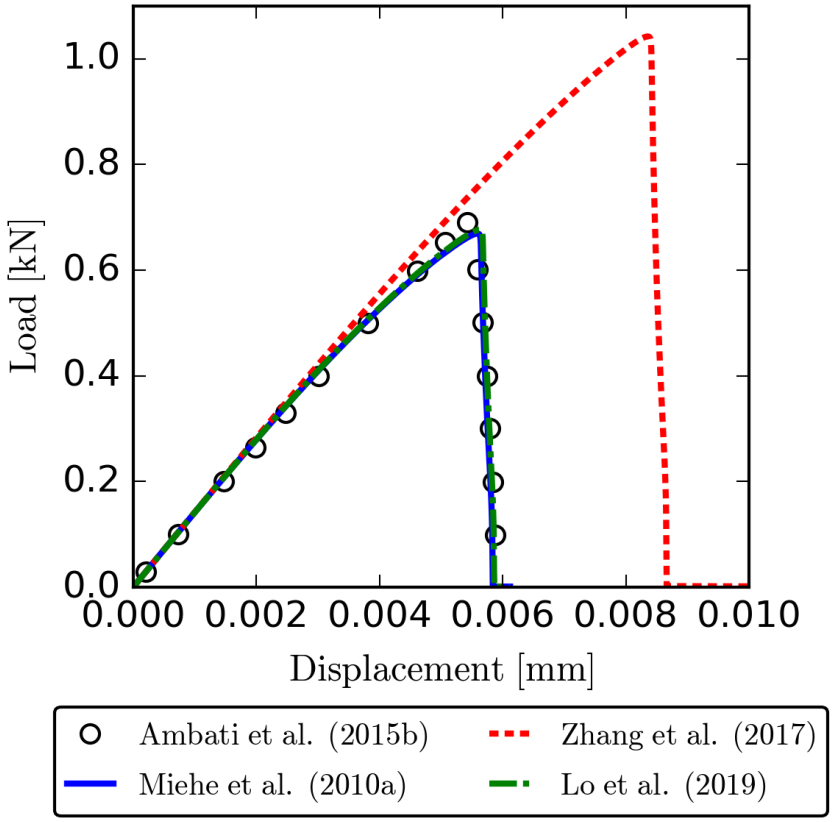

Figure H.2: Load-displacement curves for single edge notched tension test. The solid and dashed lines depict the numerical results obtained from phase field model based on the corresponding strain energy decomposition schemes. The black circular maker represents the benchmark solution digitized from Figure 9 of [10].

Appendix I LEFM model applied to predict the final depths of crevasses

The LEFM models proposed by Smith [134], Van der Veen [158, 159], and Krug et al. [77] are ideally suited for a rectangular plate-like glacier made of linear elastic ice with a single edge crack subjected to the far-field longitudinal normal stress given by Equation (G.16), as shown in Figure I.1(a). In this appendix, we consider two scenarios: i. surface crevasse propagation in grounded glaciers, and ii. surface or basal crevasse propagation in floating ice shelves. The single edge crack can approximate a surface or basal crevasse in a floating ice shelf. Furthermore, a surface crevasse in a grounded glacier with free tangential slip can be represented by double edge cracks as shown in Figure I.1(b).

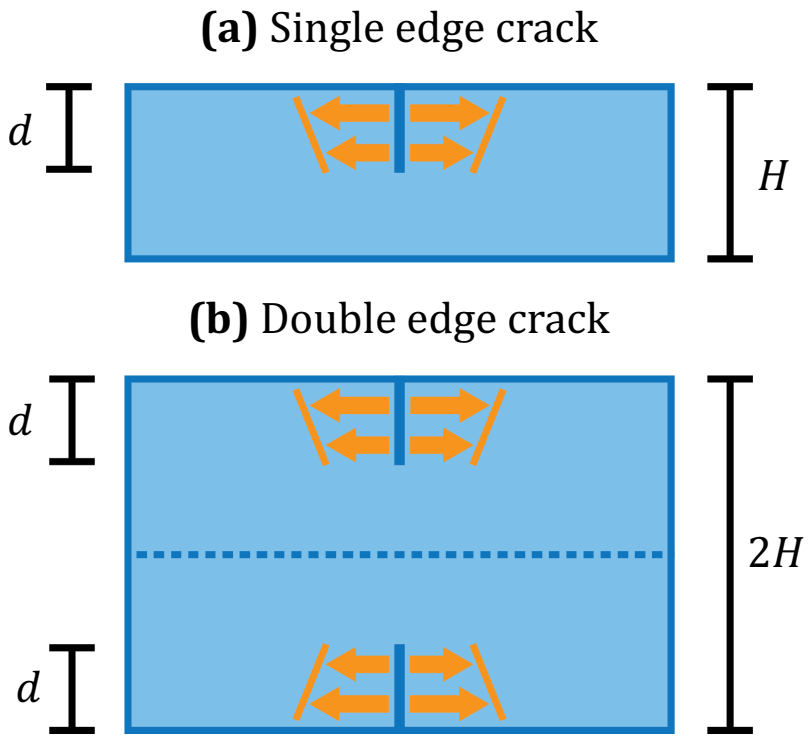

Figure I.1: (a) Single edge crack and (b) double edge cracks through finite slabs with H in width and d in crack length. The yellow arrows indicate applied loading on the crack surface that leads to crack opening. The dashed line of symmetry in (b) represent the free slip surface at the base of the glacier.

In LEFM models, the crack propagation is governed by the stress intensity factor (SIF) at the crack tip, which depends on the applied far-field stress and the initial crack length. The maximum penetration depth of crevasses can be determined by equating the mode I net SIF $K_{\mathrm{I}}^{\mathrm{net}}$ at the crevasse tip to the experimentally measured critical SIF of ice $K_{\mathrm{cI}} = 0.1\ \mathrm{MPa}\cdot\mathrm{m}^{\frac{1}{2}}$. The mode I net SIF can be evaluated as

$$K_{\mathrm{I}}^{\mathrm{net}} = \int_0^d M(\zeta, H, d)\sigma_{\mathrm{net}}(\zeta)\mathrm{d}\zeta, \tag{I.1}$$

where $M(\zeta, H, d)$ is an appropriate weight function for specific geometry and boundary conditions, and σ_{net} is the net longitudinal stress that leads to crevasse opening, which can be expressed as [16, 68, 105]

$$\sigma_{\mathrm{net}}(z) = \sigma_{\mathrm{xx}}(z) + p_{\mathrm{w}}(z), \tag{I.2}$$

where the hydraulic pressure p_{w} is given by Equation (4.19).

For the single edge crack LEFM model, we choose the weight function $M_{\mathrm{S}}(\zeta, H, d)$ utilized by Krug et al. [77]

$$\begin{aligned} M_{\mathrm{S}}(\zeta, H, d) = & \frac{2}{\sqrt{2\pi(d-\zeta)}}\left[1 + M_1\left(1-\frac{\zeta}{d}\right)^{1/2}\right. \\ & \left. + M_2\left(1-\frac{\zeta}{d}\right) + M_3\left(1-\frac{\zeta}{d}\right)^{3/2}\right], \end{aligned} \tag{I.3}$$

where $d = d_{\mathrm{s}}$ and $\zeta = H - z$ for surface crevasses; whereas, for basal crevasses, $d = d_{\mathrm{b}}$ and $\zeta = z$. Furthermore, M_1, M_2, and M_3 are given by polynomial functions listed below, which

are calibrated based on the geometry of the glacier

$$\begin{aligned} M_1 = {} & 0.0719768 - 1.513476\chi - 61.1001\chi^2 \\ & + 1554.95\chi^3 - 14583.8\chi^4 + 71590.7\chi^5 \\ & - 205384\chi^6 + 356469\chi^7 - 368270\chi^8 \\ & + 208233\chi^9 - 49544\chi^{10}, \end{aligned} \tag{I.4}$$

$$\begin{aligned} M_2 = {} & 0.246984 + 6.47583\chi + 176.456\chi^2 \\ & - 4058.76\chi^3 + 37303.8\chi^4 - 181755\chi^5 \\ & + 520551\chi^6 - 904370\chi^7 + 936863\chi^8 \\ & - 531940\chi^9 + 127291\chi^{10}, \end{aligned} \tag{I.5}$$

$$\begin{aligned} M_3 = {} & 0.529659 - 22.3235\chi + 532.074\chi^2 \\ & - 5479.53\chi^3 + 28592.2\chi^4 - 81388.6\chi^5 \\ & + 128746\chi^6 - 106246\chi^{+}35780.7\chi^8, \end{aligned} \tag{I.6}$$

where the term $\chi = \zeta/H$. As noted by Jiménez and Duddu [69], because the buoyancy force applied on the base is not captured by the LEFM models, the single edge crack case is not an exact analogy to a crevasse in a floating ice shelf. Therefore, LEFM predictions of the maximum penetration depths in Figures 4.16 and 4.17 can only be considered as reference results. The weight function for the double edge cracks LEFM model has been given by Tada et al. [150] as

$$M_{\mathrm{D}}(\zeta, H, d) = \frac{2}{\sqrt{2H}} \left[1 + f_1\left(\frac{\zeta}{d}\right) f_2\left(\frac{d}{H}\right) \right] \phi\left(\frac{d}{H}, \frac{\zeta}{H}\right), \tag{I.7}$$

where the function f_1 is given as

$$f_1\left(\frac{\zeta}{d}\right) = 0.3 \left[1 - \left(\frac{\zeta}{d}\right)^{5/4} \right], \tag{I.8}$$

and the function f_2 is given as

$$f_2\left(\frac{d}{H}\right) = \frac{1}{2}\left[1-\sin\left(\frac{\pi d}{2H}\right)\right]\left[2+\sin\left(\frac{\pi d}{2H}\right)\right], \tag{I.9}$$

and the function ϕ is given as

$$\phi\left(\frac{d}{H},\frac{\zeta}{H}\right) = \frac{\sqrt{\tan\left(\frac{\pi d}{2H}\right)}}{\sqrt{1-\left[\cos\left(\frac{\pi d}{2H}\right)/\cos\left(\frac{\pi \zeta}{2H}\right)\right]^2}}. \tag{I.10}$$

To obtain the LEFM predicted final depths of crevasses as plotted in Figures 4.12 and 4.16, we next equate the mode I net SIF evaluated using Equation (I.1) to the experimentally determined critical SIF. These nonlinear equations with the unknowns of maximum penetration depths are solved using an iterative algorithm based on the bisection method.

REFERENCES

[1] R. Abedi and R. B. Haber. Spacetime simulation of dynamic fracture with crack closure and frictional sliding. *Adv. Model Simul. Eng. Sci.*, 5(1):1–22, 2018.

[2] A. A. Abubakar, S. S. Akhtar, and A. F. M. Arif. Phase field modeling of V_2O_5 hot corrosion kinetics in thermal barrier coatings. *Comput. Mater. Sci.*, 99:105–116, 2015.

[3] I. Adlakha, B. G. Bazehhour, N. Muthegowda, and K. Solanki. Effect of mechanical loading on the galvanic corrosion behavior of a magnesium-steel structural joint. *Corros. Sci.*, 133:300–309, 2018.

[4] S. C. Aduloju and T. J. Truster. A variational multiscale discontinuous galerkin formulation for both implicit and explicit dynamic modeling of interfacial fracture. *Comput. Meth. Appl. Mech. Eng.*, 343:602–630, 2019.

[5] A. A. Aleksandrov, E. Dzhuraeva, and V. Utenkov. Viscosity of aqueous solutions of sodium chloride. *High Temp.*, 50(3):354–358, 2012.

[6] G. Alfano and M. Crisfield. Finite element interface models for the delamination analysis of laminated composites: mechanical and computational issues. *Int. J. Numer. Meth. Eng.*, 50(7):1701–1736, 2001.

[7] R. Alkire and D. Siitari. The location of cathodic reaction during localized corrosion. *J. Electrochem. Soc.*, 126(1):15–22, 1979.

[8] R. B. Alley, T. K. Dupont, B. R. Parizek, and S. Anandakrishnan. Access of surface meltwater to beds of sub-freezing glaciers: preliminary insights. *Ann. Glaciol.*, 40: 8–14, 2005.

[9] M. S. Alnæs, J. Blechta, J. Hake, A. Johansson, B. Kehlet, A. Logg, C. Richardson, J. Ring, M. E. Rognes, and G. N. Wells. The FEniCS project version 1.5. *Arch. Numer. Softw.*, 3(100):9–23, 2015.

[10] M. Ambati, T. Gerasimov, and L. De Lorenzis. A review on phase-field models of brittle fracture and a new fast hybrid formulation. *Comput. Mech.*, 55(2):383–405, 2015.

[11] H. Amor, J.-J. Marigo, and C. Maurini. Regularized formulation of the variational brittle fracture with unilateral contact: Numerical experiments. *J. Mech. Phys. Solids*, 57(8):1209–1229, 2009.

[12] A. Anderko, N. Sridhar, and D. Dunn. A general model for the repassivation potential as a function of multiple aqueous solution species. *Corros. Sci.*, 46(7):1583–1612, 2004.

[13] T. Q. Ansari, Z. Xiao, S. Hu, Y. Li, J.-L. Luo, and S.-Q. Shi. Phase-field model of pitting corrosion kinetics in metallic materials. *npj Comput. Mater.*, 4(1):38, 2018.

[14] J. Arnold, R. Duddu, K. Brown, and D. S. Kosson. Influence of multi-species solute transport on modeling of hydrated portland cement leaching in strong nitrate solutions. *Cement Concrete Res.*., 100:227–244, 2017.

[15] V. S. Bagotsky. *Fundamentals of electrochemistry*, volume 44. John Wiley & Sons, 2005.

[16] J. N. Bassis. The statistical physics of iceberg calving and the emergence of universal calving laws. *J. Glaciol.*, 57(201):3–16, 2011.

[17] J. N. Bassis and C. Walker. Upper and lower limits on the stability of calving glaciers from the yield strength envelope of ice. *Proc. Math. Phys. Eng. Sci.*, 468(2140):913–931, 2012.

[18] J. H. T. Bates, S. S. Wagers, R. J. Norton, L. M. Rinaldi, and C. G. Irvin. Hydrolysis of cations. In *Inorganic Complexes*. Plenum Press, 1976.

[19] D. I. Benn, C. R. Warren, and R. H. Mottram. Calving processes and the dynamics of calving glaciers. *Earth-Sci. Rev.*, 82(3-4):143–179, 2007.

[20] C. M. Bethke. *Geochemical and Biogeochemical Reaction Modeling*. Cambridge University Press, 2 edition, 2007.

[21] P. Blanc, A. Lassin, P. Piantone, M. Azaroual, N. Jacquemet, A. Fabbri, and E. C. Gaucher. Thermoddem: A geochemical database focused on low temperature water/rock interactions and waste materials. *Appl. Geochem.*, 27(10):2107–2116, 2012.

[22] F. Bogar and C. Fujii. Solution chemistry in crevices on Fe-Cr binary alloys. Technical report, Naval Research Laboratory Washington D.C., 1974.

[23] S. Bordas, T. Rabczuk, and G. Zi. Three-dimensional crack initiation, propagation, branching and junction in non-linear materials by an extended meshfree method without asymptotic enrichment. *Eng. Fract. Mech.*, 75(5):943–960, 2008.

[24] P.-O. Bouchard, F. Bay, and Y. Chastel. Numerical modelling of crack propagation: automatic remeshing and comparison of different criteria. *Comput. Meth. Appl. Mech. Eng.*, 192(35-36):3887–3908, 2003.

[25] B. Bourdin, G. A. Francfort, and J.-J. Marigo. Numerical experiments in revisited brittle fracture. *J. Mech. Phys. Solids*, 48(4):797–826, 2000.

[26] E. C. Bryant and W. Sun. A mixed-mode phase field fracture model in anisotropic rocks with consistent kinematics. *Comput. Meth. Appl. Mech. Eng.*, 342:561–584, 2018.

[27] G. Burstein, P. Pistorius, and S. Mattin. The nucleation and growth of corrosion pits on stainless steel. *Corros. Sci.*, 35(1-4):57–62, 1993.

[28] S. Caines, F. Khan, J. Shirokoff, and W. Qiu. Experimental design to study corrosion under insulation in harsh marine environments. *J. Loss Prevent. Proc.*, 33:39–51, 2015.

[29] B. Carrier and S. Granet. Numerical modeling of hydraulic fracture problem in permeable medium using cohesive zone model. *Eng. Fract. Mech.*, 79:312–328, 2012.

[30] J. L. Chaboche. Continuum Damage Mechanics: Part I—General Concepts. *J. Appl. Mech.*, 55(1):59–64, 03 1988.

[31] H.-Y. Chang, Y.-S. Park, and W.-S. Hwang. Modeling of crevice solution chemistry on the initiation stage of crevice corrosion in Fe-Cr alloys. *Met. Mater.*, 4(6):1199–1206, 1998.

[32] J. Chang and K. Nakshatrala. Variational inequality approach to enforcing the non-negative constraint for advection-diffusion equations. *Comput. Methods Appl. Mech. Eng.*, 320:287 – 334, 2017.

[33] Z. Chen and F. Bobaru. Peridynamic modeling of pitting corrosion damage. *J. Mech. Phys. Solids*, 78:352–381, 2015.

[34] Z. Chen and R. Kelly. Computational modeling of bounding conditions for pit size on stainless steel in atmospheric environments. *J. Electrochem. Soc.*, 157(2):C69, 2009.

[35] Z. Chen, G. Zhang, and F. Bobaru. The influence of passive film damage on pitting corrosion. *J. Electrochem. Soc.*, 163(2):C19, 2015.

[36] I. M. Chou and L. D. Phan. Solubility relations in the system potassium chloride-ferrous chloride-water between 25 and 75°C at 1 atm. *J. Chem. Eng. Data*, 31(2): 154–156, 1986.

[37] J. Christmann, R. Müller, K. Webber, D. Isaia, F. Schader, S. Kipfstuhl, J. Freitag, and A. Humbert. Measurement of fracture toughness of polycrystalline bubbly ice from an antarctic ice core. *Earth Syst. Sci. Data*, 7:87–92, 2015.

[38] W. Colgan, H. Rajaram, W. Abdalati, C. McCutchan, R. Mottram, M. S. Moussavi, and S. Grigsby. Glacier crevasses: Observations, models, and mass balance implications. *Rev Geophys*, 54(1):119–161, 2016.

[39] K. M. Cuffey and W. S. B. Paterson. *The physics of glaciers*. Academic Press, 2010.

[40] D. Deconinck, S. Van Damme, and J. Deconinck. A temperature dependent multiion model for time accurate numerical simulation of the electrochemical machining process. Part II: numerical simulation. *Electrochim. Acta*, 69:120–127, 2012.

[41] K. B. Deshpande. Validated numerical modelling of galvanic corrosion for couples: Magnesium alloy (AE44)–mild steel and AE44–aluminium alloy (AA6063) in brine solution. *Corros. Sci.*, 52(10):3514–3522, 2010.

[42] R. Duddu. Numerical modeling of corrosion pit propagation using the combined extended finite element and level set method. *Comput. Mech.*, 54(3):613–627, 2014.

[43] R. Duddu and H. Waisman. A temperature dependent creep damage model for polycrystalline ice. *Mech. Mater.*, 46:23–41, 2012.

[44] R. Duddu and H. Waisman. A nonlocal continuum damage mechanics approach to simulation of creep fracture in ice sheets. *Comput. Mech.*, 51(6):961–974, 2013.

[45] R. Duddu, J. Bassis, and H. Waisman. A numerical investigation of surface crevasse propagation in glaciers using nonlocal continuum damage mechanics. *Geophys. Res. Lett.*, 40(12):3064–3068, 2013.

[46] R. Duddu, N. Kota, and S. M. Qidwai. An extended finite element method based

approach for modeling crevice and pitting corrosion. *J. Appl. Mech.*, 83(8):081003, 2016.

[47] R. Duddu, S. Jiménez, and J. Bassis. A non-local continuum poro-damage mechanics model for hydrofracturing of surface crevasses in grounded glaciers. *J. Glaciol.*, 66(257):415–429, 2020.

[48] P. Dumstorff and G. Meschke. Crack propagation criteria in the framework of X-FEM-based structural analyses. *Int. J. Numer. Anal. Meth. Geomech.*, 31(2):239–259, 2007.

[49] P. Ernst and R. Newman. Pit growth studies in stainless steel foils. I. Introduction and pit growth kinetics. *Corros. Sci.*, 44(5):927–941, 2002.

[50] P. Ernst and R. Newman. Pit growth studies in stainless steel foils. II. Effect of temperature, chloride concentration and sulphate addition. *Corros. Sci.*, 44(5):943–954, 2002.

[51] P. Ernst and R. Newman. Explanation of the effect of high chloride concentration on the critical pitting temperature of stainless steel. *Corros. Sci.*, 49(9):3705–3715, 2007.

[52] A. Fick. Ueber diffusion. *Ann. Phys.*, 170(1):59–86, 1855.

[53] A. Fossati, F. Borgioli, E. Galvanetto, and T. Bacci. Corrosion resistance properties of glow-discharge nitrided AISI 316L austenitic stainless steel in NaCl solutions. *Corros. Sci.*, 48(6):1513–1527, 2006.

[54] G. A. Francfort and J.-J. Marigo. Revisiting brittle fracture as an energy minimization problem. *J. Mech. Phys. Solids*, 46(8):1319–1342, 1998.

[55] G. Frankel and N. Sridhar. Understanding localized corrosion. *Mater. Today*, 11 (10):38 – 44, 2008.

[56] J. R. Galvele. Transport processes and the mechanism of pitting of metals. *J. Electrochem. Soc.*, 123(4):464, 1976.

[57] G. Gaudet, W. Mo, T. Hatton, J. Tester, J. Tilly, H. S. Isaacs, and R. Newman. Mass transfer and electrochemical kinetic interactions in localized pitting corrosion. *AIChE J.*, 32(6):949–958, 1986.

[58] G. Ghosh, R. Duddu, and C. Annavarapu. A stabilized finite element method for enforcing stiff anisotropic cohesive laws using interface elements. *Comput. Meth. Appl. Mech. Eng.*, 348:1013–1038, 2019.

[59] S. Glasstone. *An introduction to electrochemistry*. Read Books Ltd, 2011.

[60] A. Griffith. The phenomena of rupture and flow in solids. *Phil. Trans. R. Soc. Lond.*, 221:163–198, 1921.

[61] P. Gupta, C. A. Duarte, and A. Dhankhar. Accuracy and robustness of stress intensity factor extraction methods for the generalized/eXtended finite element method. *Eng. Fract. Mech.*, 179:120–153, 2017.

[62] J. Herzer and W. Kinzelbach. Coupling of transport and chemical processes in numerical transport models. *Geoderma*, 44(2-3):115–127, 1989.

[63] A. Hillerborg, M. Modéer, and P.-E. Petersson. Analysis of crack formation and crack growth in concrete by means of fracture mechanics and finite elements. *Cement Concrete Res.*, 6(6):773–781, 1976.

[64] H. Isaacs. The behavior of resistive layers in the localized corrosion of stainless steel. *J. Electrochem. Soc.*, 120(11):1456, 1973.

[65] H. Isaacs, J.-H. Cho, M. Rivers, and S. Sutton. In situ X-Ray microprobe study of salt layers during anodic dissolution of stainless steel in chloride solution. *J. Electrochem. Soc.*, 142(4):1111, 1995.

[66] S. Jafarzadeh, Z. Chen, and F. Bobaru. Peridynamic modeling of repassivation in pitting corrosion of stainless steel. *Corros.*, 74(4):393–414, 2017.

[67] S. Jafarzadeh, Z. Chen, and F. Bobaru. Peridynamic modeling of repassivation in pitting corrosion of stainless steel. *Corrosion*, 74(4):393–414, 2018.

[68] K. C. Jezek. A modified theory of bottom crevasses used as a means for measuring the buttressing effect of ice shelves on inland ice sheets. *J. Geophys. Res. Solid Earth*, 89(B3):1925–1931, 1984.

[69] S. Jiménez and R. Duddu. On the evaluation of the stress intensity factor in calving models using linear elastic fracture mechanics. *J. Glaciol.*, 64(247):759–770, 2018.

[70] S. Jiménez, X. Liu, R. Duddu, and H. Waisman. A discrete damage zone model for mixed-mode delamination of composites under high-cycle fatigue. *Int. J. Fract.*, 190 (1-2):53–74, 2014.

[71] S. Jiménez, R. Duddu, and J. Bassis. An updated-lagrangian damage mechanics formulation for modeling the creeping flow and fracture of ice sheets. *Comput. Meth. Appl. Mech. Eng.*, 313:406–432, 2017.

[72] J. Jun, G. Frankel, and N. Sridhar. Effect of chloride concentration and temperature on growth of 1D pit. *J. Solid State Electr.*, 19(12):3439–3447, 2015.

[73] J. Jun, G. Frankel, and N. Sridhar. Further modeling of chloride concentration and temperature effects on 1D pit growth. *J. Electrochem. Soc.*, 163(14):C823–C829, 2016.

[74] J. Jun, T. Li, G. Frankel, and N. Sridhar. Corrosion and repassivation of Super 13Cr stainless steel in artificial 1D pit electrodes at elevated temperature. *Corros. Sci.*, page 108754, 2020.

[75] R. Katona, J. Carpenter, E. Schindelholz, and R. Kelly. Prediction of maximum pit sizes in elevated chloride concentrations and temperatures. *J. Electrochem. Soc.*, 166 (11):C3364, 2019.

[76] K. Kontturi, L. Murtomäki, and J. A. Manzanares. *Ionic transport processes: in electrochemistry and membrane science*. OUP Oxford, 2008.

[77] J. Krug, J. Weiss, O. Gagliardini, and G. Durand. Combining damage and fracture mechanics to model calving. *The Cryosphere*, 8(6):2101–2117, 2014.

[78] C. Kuhn and R. Müller. A continuum phase field model for fracture. *Eng. Fract. Mech.*, 77(18):3625–3634, 2010.

[79] C.-Y. Lai, J. Kingslake, M. G. Wearing, P.-H. C. Chen, P. Gentine, H. Li, J. J. Spergel, and J. M. van Wessem. Vulnerability of antarctica's ice shelves to meltwater-driven fracture. *Nature*, 584(7822):574–578, 2020.

[80] D. Lampkin, N. Amador, B. Parizek, K. Farness, and K. Jezek. Drainage from water-filled crevasses along the margins of jakobshavn isbræ: A potential catalyst for catchment expansion. *J. Geophys. Res. Solid Earth*, 118(2):795–813, 2013.

[81] N. Laycock and R. Newman. Localised dissolution kinetics, salt films and pitting potentials. *Corros. Sci.*, 39(10-11):1771–1790, 1997.

[82] N. Laycock, S. White, J. Noh, P. Wilson, and R. Newman. Perforated covers for propagating pits. *J. Electrochem. Soc.*, 145(4):1101–1108, 1998.

[83] T. Li, J. Scully, and G. Frankel. Localized corrosion: passive film breakdown vs. pit growth stability: Part III. a unifying set of principal parameters and criteria for pit stabilization and salt film formation. *J. Electrochem. Soc.*, 165(11):C762, 2018.

[84] T. Li, J. Scully, and G. Frankel. Localized corrosion: passive film breakdown vs.

pit growth stability: part IV. the role of salt film in pit growth: a mathematical framework. *J. Electrochem. Soc.*, 166(6):C115, 2019.

[85] X. Liu, R. Duddu, and H. Waisman. Discrete damage zone model for fracture initiation and propagation. *Eng. Fract. Mech.*, 92:1–18, 2012.

[86] Y.-S. Lo, M. J. Borden, K. Ravi-Chandar, and C. M. Landis. A phase-field model for fatigue crack growth. *J. Mech. Phys. Solids*, 132:103684, 2019.

[87] D. Macdonald and G. Engelhardt. *Shreir's Corrosion*, chapter 2.39 Predictive Modeling of Corrosion, pages 1630–1679. Elsevier, Amsterdam, 2010.

[88] W. Mai and S. Soghrati. A phase field model for simulating the stress corrosion cracking initiated from pits. *Corros. Sci.*, 125:87–98, 2017.

[89] W. Mai and S. Soghrati. New phase field model for simulating galvanic and pitting corrosion processes. *Electrochim. Acta*, 260:290–304, 2018.

[90] W. Mai, S. Soghrati, and R. G. Buchheit. A phase field model for simulating the pitting corrosion. *Corros. Sci.*, 110:157–166, 2016.

[91] B. Malki, T. Souier, and B. Baroux. Influence of the alloying elements on pitting corrosion of stainless steels: A modeling approach. *J. Electrochem. Soc.*, 155(12): C583–C587, 2008.

[92] J. Mankowski and Z. Szklarska-Smialowska. Studies on accumulation of chloride ions in pits growing during anodic polarization. *Corros. Sci.*, 15(6-12):493–501, 1975.

[93] B. Mazurowski, A. Sanchez-Rivadeneira, N. Shauer, and C. Duarte. High-order stable generalized/extended finite element approximations for accurate stress intensity factors. *Eng. Fract. Mech.*, page 107308, 2020.

[94] E. McCafferty. *Introduction to Corrosion Science*. Springer Science & Business Media, 2010.

[95] C. Miehe, M. Hofacker, and F. Welschinger. A phase field model for rate-independent crack propagation: Robust algorithmic implementation based on operator splits. *Comput. Meth. Appl. Mech. Eng.*, 199(45-48):2765–2778, 2010.

[96] C. Miehe, F. Welschinger, and M. Hofacker. Thermodynamically consistent phase-field models of fracture: Variational principles and multi-field FE implementations. *Int. J. Numer. Methods. Eng.*, 83(10):1273–1311, 2010.

[97] A. Mikelić, M. F. Wheeler, and T. Wick. Phase-field modeling of a fluid-driven fracture in a poroelastic medium. *Comput. Geosci.*, 19(6):1171–1195, 2015.

[98] M. H. Moayed and R. Newman. The relationship between pit chemistry and pit geometry near the critical pitting temperature. *J. Electrochem. Soc.*, 153(8):B330, 2006.

[99] M. E. Mobasher, R. Duddu, J. N. Bassis, and H. Waisman. Modeling hydraulic fracture of glaciers using continuum damage mechanics. *J. Glaciol.*, 62(234):794–804, 2016.

[100] S. Murakami. *Continuum damage mechanics: a continuum mechanics approach to the analysis of damage and fracture*, volume 185. Springer Science & Business Media, 2012.

[101] K. Nakshatrala, M. K. Mudunuru, and A. J. Valocchi. A numerical framework for diffusion-controlled bimolecular-reactive systems to enforce maximum principles and the non-negative constraint. *J. Comput. Phys.*, 253:278–307, 2013.

[102] W. Nernst. *Zur kinetik der in lösung befindlichen körper*. Universitätsbibliothek Johann Christian Senckenberg, 2009.

[103] S. Nešić. Key issues related to modelling of internal corrosion of oil and gas pipelines–a review. *Corros. Sci.*, 49(12):4308–4338, 2007.

[104] R. Newman and H. Isaacs. Diffusion-coupled active dissolution in the localized corrosion of stainless steels. *J. Electrochem. Soc.*, 130(7):1621, 1983.

[105] F. M. Nick, C. J. Van der Veen, A. Vieli, and D. I. Benn. A physically based calving model applied to marine outlet glaciers and implications for the glacier dynamics. *J. Glaciol.*, 56(199):781–794, 2010.

[106] T. Okada. Considerations of the stability of pit repassivation during pitting corrosion of passive metals. *J. Electrochem. Soc.*, 131(5):1026, 1984.

[107] J. Oldfield and W. Sutton. Crevice corrosion of stainless steels: II. Experimental studies. *Br. Corros. J.*, 13(3):104–111, 1978.

[108] J. Ožbolt, G. Balabanić, and M. Kušter. 3D numerical modelling of steel corrosion in concrete structures. *Corros. Sci.*, 53(12):4166–4177, 2011.

[109] L. Pauling. *General chemistry*. Courier Corporation, 1988.

[110] R. H. Peerlings, R. de Borst, W. M. Brekelmans, and J. De Vree. Gradient enhanced damage for quasi-brittle materials. *Int. J. Numer. Meth. Eng.*, 39(19):3391–3403, 1996.

[111] K. Pham, K. Ravi-Chandar, and C. Landis. Experimental validation of a phase-field model for fracture. *Int. J. Fract.*, 205(1):83–101, 2017.

[112] R. M. Pidaparti, L. Fang, and M. J. Palakal. Computational simulation of multi-pit corrosion process in materials. *Comput. Mater. Sci.*, 41(3):255–265, 2008.

[113] G. Pijaudier-Cabot and Z. P. Bažant. Nonlocal damage theory. *J. Eng. Mech.*, 113 (10):1512–1533, 1987.

[114] P. Pistorius and G. Burstein. Metastable pitting corrosion of stainless steel and the transition to stability. *Philos. Trans. Royal Soc. A*, 341(1662):531–559, 1992.

[115] K. S. Pitzer. Thermodynamics of electrolytes. I. Theoretical basis and general equations. *J. Phys. Chem.*, 77(2):268–277, 1973.

[116] A. Pralong and M. Funk. Dynamic damage model of crevasse opening and application to glacier calving. *J. Geophys. Res. Solid Earth*, 110(B1), 2005.

[117] H. Ren, X. Zhuang, C. Anitescu, and T. Rabczuk. An explicit phase field method for brittle dynamic fracture. *Comput. Struct.*, 217:45–56, 2019.

[118] M. Rist, P. Sammonds, S. Murrell, P. Meredith, C. Doake, H. Oerter, and K. Matsuki. Experimental and theoretical fracture mechanics applied to antarctic ice fracture and surface crevassing. *J. Geophys. Res. Solid Earth*, 104(B2):2973–2987, 1999.

[119] R. A. Robinson and R. H. Stokes. *Electrolyte solutions*. Courier Corporation, 2002.

[120] J. Samper, T. Xu, and C. Yang. A sequential partly iterative approach for multicomponent reactive transport with CORE 2D. *Comput. Geosci.*, 13(3):301, 2009.

[121] E. Samson and J. Marchand. Modeling the transport of ions in unsaturated cement-based materials. *Comput. Struct.*, 85(23-24):1740–1756, 2007.

[122] D. Santillán, R. Juanes, and L. Cueto-Felgueroso. Phase field model of fluid-driven fracture in elastic media: Immersed-fracture formulation and validation with analytical solutions. *J. Geophys. Res. Solid Earth*, 122(4):2565–2589, 2017.

[123] D. Santillán, R. Juanes, and L. Cueto-Felgueroso. Phase field model of hydraulic fracturing in poroelastic media: Fracture propagation, arrest, and branching under fluid injection and extraction. *J. Geophys. Res. Solid Earth*, 123(3):2127–2155, 2018.

[124] S. Sarkar, J. E. Warner, and W. Aquino. A numerical framework for the modeling of corrosive dissolution. *Corros. Sci.*, 65:502 – 511, 2012.

[125] S. Scheiner and C. Hellmich. Stable pitting corrosion of stainless steel as diffusion-controlled dissolution process with a sharp moving electrode boundary. *Corros. Sci.*, 49(2):319–346, 2007.

[126] S. Scheiner and C. Hellmich. Finite volume model for diffusion-and activation-controlled pitting corrosion of stainless steel. *Comput. Methods Appl. Mech. Eng.*, 198(37-40):2898–2910, 2009.

[127] A. Schlüter, A. Willenbücher, C. Kuhn, and R. Müller. Phase field approximation of dynamic brittle fracture. *Comput. Mech.*, 54(5):1141–1161, 2014.

[128] M. Schorr, B. Valdez, R. Salinas, R. Ramos, N. Nedey, and M. Curiel. Corrosion control in military assets. *MRS Online Proceedings Library Archive*, 1815, 2016.

[129] A. Sedriks. Corrosion resistance of austenitic Fe-Cr-Ni-Mo alloys in marine environments. *Int. Met. Rev.*, 27(1):321–353, 1982.

[130] R. R. Settgast, P. Fu, S. D. Walsh, J. A. White, C. Annavarapu, and F. J. Ryerson. A fully coupled method for massively parallel simulation of hydraulically driven fractures in 3-dimensions. *Int. J. Numer. Anal. Meth. Geomech.*, 41(5):627–653, 2017.

[131] S. M. Sharland. A mathematical model of crevice and pitting corrosion–ii. the mathematical solution. *Corros. Sci.*, 28(6):621–630, 1988.

[132] S. M. Sharland. A mathematical model of the initiation of crevice corrosion in metals. *Corros. Sci.*, 33(2):183–201, 1992.

[133] S. M. Sharland and P. W. Tasker. A mathematical model of crevice and pitting corrosion–i. the physical model. *Corros. Sci.*, 28(6):603–620, 1988.

[134] R. Smith. The application of fracture mechanics to the problem of crevasse penetration. *J. Glaciol.*, 17(76):223–228, 1976.

[135] C. Song, E. T. Ooi, and S. Natarajan. A review of the scaled boundary finite element method for two-dimensional linear elastic fracture mechanics. *Eng. Fract. Mech.*, 187:45–73, 2018.

[136] N. Sridhar, C. Brossia, D. Dunn, and A. Anderko. Predicting localized corrosion in seawater. *Corrosion*, 60(10):915–936, 2004.

[137] J. Srinivasan and R. Kelly. Evaluating the critical chemistry for repassivation at the corroding surface using mass transport model-based artificial pit experiments. *J. Electrochem. Soc.*, 163(13):C768–C777, 2016.

[138] J. Srinivasan and R. Kelly. One-dimensional pit experiments and modeling to determine critical factors for pit stability and repassivation. *J. Electrochem. Soc.*, 163 (13):C759–C767, 2016.

[139] J. Srinivasan, M. McGrath, and R. Kelly. A high-throughput artificial pit technique to measure kinetic parameters for pitting stability. *J. Electrochem. Soc.*, 162(14): C725–C731, 2015.

[140] J. Srinivasan, C. Liu, and R. Kelly. Geometric evolution of flux from a corroding one-dimensional pit and its implications on the evaluation of kinetic parameters for pit stability. *J. Electrochem. Soc.*, 163(10):C694–C703, 2016.

[141] C. I. Steefel and A. C. Lasaga. A coupled model for transport of multiple chemical species and kinetic precipitation/dissolution reactions with application to reactive flow in single phase hydrothermal systems. *Am. J. Sci.*, 294(5):529–592, 1994.

[142] C. Steinke and M. Kaliske. A phase-field crack model based on directional stress decomposition. *Comput. Mech.*, 63(5):1019–1046, 2019.

[143] R. H. Stokes and R. A. Robinson. Ionic hydration and activity in electrolyte solutions. *J. Am. Chem. Soc.*, 70(5):1870–1878, 1948.

[144] H.-H. Strehblow and M. Ives. On the electrochemical conditions within small pits. *Corros. Sci.*, 16(5):317–321, 1976.

[145] M. Stroe, R. Oltra, and B. Vuillemin. Modeling of crevice corrosion of Fe-Cr alloys in chloride media. *ECS Trans.*, 11(12):1–9, 2008.

[146] N. Sukumar, D. L. Chopp, E. Béchet, and N. Moës. Three-dimensional non-planar crack growth by a coupled extended finite element and fast marching method. *Int. J. Numer. Meth. Eng.*, 76(5):727–748, 2008.

[147] W. Sun, L. Wang, T. Wu, and G. Liu. An arbitrary lagrangian–eulerian model for modelling the time-dependent evolution of crevice corrosion. *Corros. Sci.*, 78:233–243, 2014.

[148] X. Sun and R. Duddu. A sequential non-iterative approach for modeling multi-ionic species reactive transport during localized corrosion. *Finite Elem. Anal. Des.*, 166: 103318, 2019.

[149] Z. Szklarska-Smialowska and J. Mankowski. Crevice corrosion of stainless steels in sodium chloride solution. *Corros. Sci.*, 18(11):953–960, 1978.

[150] H. Tada, P. C. Paris, and G. R. Irwin. *The Stress Analysis of Cracks Handbook, Third Edition*. ASME Press, 01 2000. ISBN 0791801535.

[151] J. Tester and H. Isaacs. Diffusional effects in simulated localized corrosion. *J. Electrochem. Soc.*, 122(11):1438, 1975.

[152] P. A. Tuckett, J. C. Ely, A. J. Sole, S. J. Livingstone, B. J. Davison, J. M. van Wessem, and J. Howard. Rapid accelerations of antarctic peninsula outlet glaciers driven by surface melt. *Nat. Commun.*, 10(1):1–8, 2019.

[153] A. Turnbull. Theoretical evaluation of the dissolved oxygen concentration in a crevice or crack in a metal in aqueous solution. *Br. Corros. J.*, 15(4):162–171, 1980.

[154] A. Turnbull and J. Thomas. A model of crack electrochemistry for steels in the active state based on mass transport by diffusion and ion migration. *J. Electrochem. Soc.*, 129(7):1412–1422, 1982.

[155] L. Ultee, C. Meyer, and B. Minchew. Tensile strength of glacial ice deduced from observations of the 2015 eastern skaftá cauldron collapse, vatnajökull ice cap, iceland. *J. Glaciol.*, pages 1–10, 2020.

[156] A. Vagbharathi and S. Gopalakrishnan. An extended finite-element model coupled with level set method for analysis of growth of corrosion pits in metallic structures. *Proceedings of the Royal Society A: Mathematical, Physical and Engineering Sciences*, 470(2168):20140001, 2014.

[157] A. J. Valocchi and M. Malmstead. Accuracy of operator splitting for advection-dispersion-reaction problems. *Water Resour. Res.*, 28(5):1471–1476, 1992.

[158] C. Van der Veen. Fracture mechanics approach to penetration of bottom crevasses on glaciers. *Cold Reg. Sci. Technol.*, 27(3):213–223, 1998.

[159] C. Van der Veen. Fracture mechanics approach to penetration of surface crevasses on glaciers. *Cold Reg. Sci. Technol.*, 27(1):31–47, 1998.

[160] C. V. Verhoosel and R. de Borst. A phase-field model for cohesive fracture. *Int. J. Numer. Methods. Eng.*, 96(1):43–62, 2013.

[161] A. Walter, E. Frind, D. Blowes, C. Ptacek, and J. Molson. Modeling of multicomponent reactive transport in groundwater: 1. model development and evaluation. *Water. Resour. Res.*, 30(11):3137–3148, 1994.

[162] J. Walton, G. Cragnolino, and S. Kalandros. A numerical model of crevice corrosion for passive and active metals. *Corros. Sci.*, 38(1):1–18, 1996.

[163] J. C. Walton. Mathematical modeling of mass transport and chemical reaction in crevice and pitting corrosion. *Corros. Sci.*, 30(8-9):915–928, 1990.

[164] J. Weerheijm. *Understanding the tensile properties of concrete*. Elsevier, 2013.

[165] J. Weertman. Can a water-filled crevasse reach the bottom surface of a glacier. *IASH Publ.*, 95:139–145, 1973.

[166] M. Woldemedhin, J. Srinivasan, and R. Kelly. Effects of environmental factors on key kinetic parameters relevant to pitting corrosion. *J. Solid State Electr.*, 19(12): 3449–3461, 2015.

[167] J.-Y. Wu, V. P. Nguyen, H. Zhou, and Y. Huang. A variationally consistent phase-field anisotropic damage model for fracture. *Comput. Meth. Appl. Mech. Eng.*, 358: 112629, 2020.

[168] W. Wu, Z. Liu, S. Hu, X. Li, and C. Du. Effect of pH and hydrogen on the stress corrosion cracking behavior of duplex stainless steel in marine atmosphere environment. *Ocean Eng.*, 146:311–323, 2017.

[169] J. Xiao and S. Chaudhuri. Predictive modeling of localized corrosion: an application to aluminum alloys. *Electrochim. Acta*, 56(16):5630–5641, 2011.

[170] Z. Xiao, S. Hu, J. Luo, S. Shi, and C. Henager. A quantitative phase-field model for crevice corrosion. *Comput. Mater. Sci.*, 149:37–48, 2018.

[171] K. Yaya, Y. Khelfaoui, B. Malki, and M. Kerkar. Numerical simulations study of the localized corrosion resistance of aisi 316l stainless steel and pure titanium in a simulated body fluid environment. *Corros. Sci.*, 53(10):3309–3314, 2011.

[172] G. Yeh and V. Tripathi. A critical evaluation of recent developments in hydrogeochemical transport models of reactive multichemical components. *Water. Resour. Res.*, 25(1):93–108, 1989.

[173] G. Yeh and V. Tripathi. A model for simulating transport of reactive multispecies components: model development and demonstration. *Water. Resour. Res.*, 27(12): 3075–3094, 1991.

[174] B. Yin and M. Kaliske. Fracture simulation of viscoelastic polymers by the phase-field method. *Comput. Mech.*, 65:293–309, 2020.

[175] L. Yin, Y. Jin, C. Leygraf, N. Birbilis, and J. Pan. Numerical simulation of micro-galvanic corrosion in al alloys: effect of geometric factors. *J. Electrochem. Soc.*, 164 (2):C75–C84, 2017.

[176] H. Yu, E. Rignot, M. Morlighem, and H. Seroussi. Iceberg calving of thwaites glacier, west antarctica: full-stokes modeling combined with linear elastic fracture mechanics. *The Cryosphere*, 11(3):1283, 2017.

[177] X. Zhang, S. W. Sloan, C. Vignes, and D. Sheng. A modification of the phase-field model for mixed mode crack propagation in rock-like materials. *Comput. Meth. Appl. Mech. Eng.*, 322:123–136, 2017.

[178] S. Zhou, X. Zhuang, and T. Rabczuk. Phase field modeling of brittle compressive-shear fractures in rock-like materials: A new driving force and a hybrid formulation. *Comput. Meth. Appl. Mech. Eng.*, 355:729–752, 2019.